Ternary Bismuth-based Functional Materials for Photoelectrochemical Water Oxidation

A Dissertation Approved by the Department of Material and Geosciences of the Technical University of Darmstadt in Fulfillment of the Requirements for the Degree of Doctor Rerum Naturalium (Dr. rer. nat.)

Xiaofeng Wu

Born in Hubei, the People's Republic of China

Surface Science

TECHNISCHE UNIVERSITÄT DARMSTADT

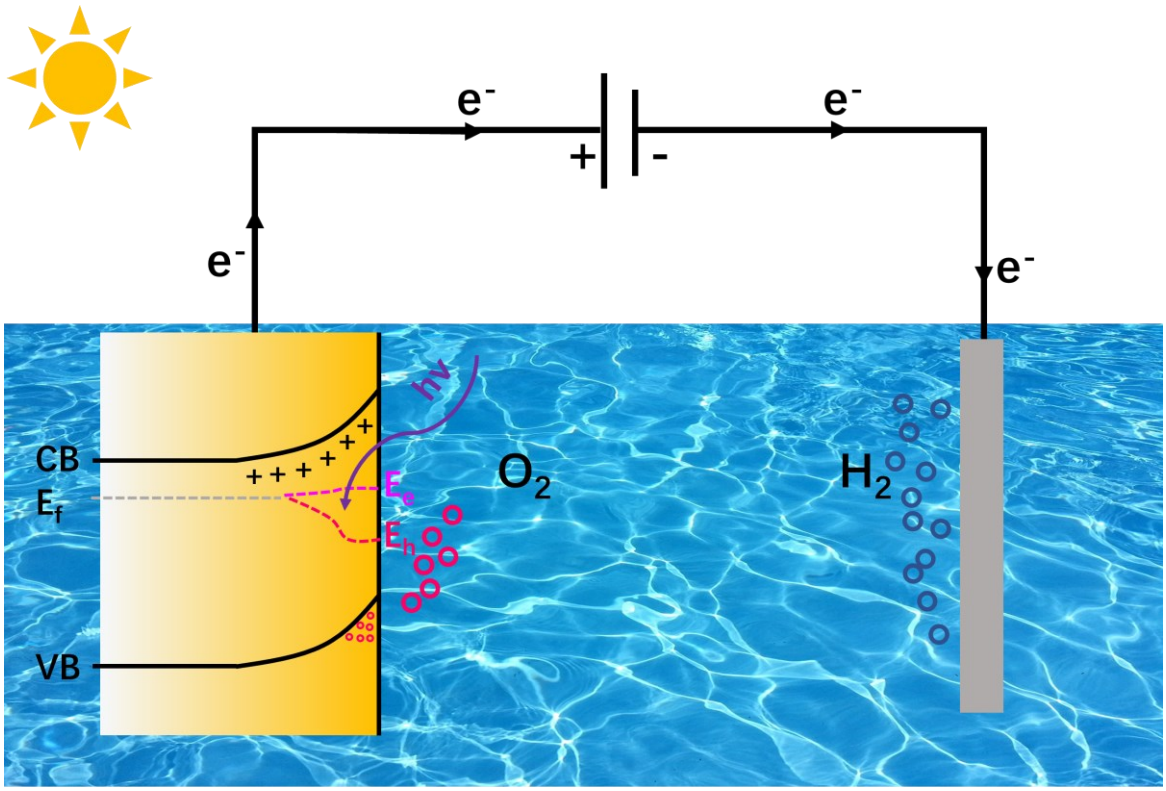

A Dissertation Approved by the Department of Material and Geosciences of the Technical University of Darmstadt in Fulfillment of the Requirements for the Degree of Doctor Rerum Naturalium (Dr. rer. nat.)

Ternary Bismuth-based Functional Materials for Photoelectrochemical Water Oxidation

Xiaofeng Wu

Born in Hubei, the People's Republic of China

1st Referee: Prof. Dr. Jan Philipp Hofmann

2nd Referee: Dr. Freddy E. Oropeza Palacio

Fachbereich Material- und Geowissenschaften

Technische Universität Darmstadt

Date of submission: 28.05.2024

Date of oral examination: 30.07.2024

Darmstadt 2024

D 17

"*As Heaven's movement is ever vigorous, so must a gentleman ceaselessly strive along*."

The book of changes

Erklärungen laut Promotionsordnung

§8 Abs. 1 lit. c PromO

Ich versichere hiermit, dass die elektronische Version meiner Dissertation mit der schriftlichen Version übereinstimmt.

§8 Abs. 1 lit. d PromO

Ich versichere hiermit, dass zu einem vorherigen Zeitpunkt noch keine Promotion versucht wurde. In diesem Fall sind nähere Angaben über Zeitpunkt, Hochschule, Dissertationsthema und Ergebnis dieses Versuchs mitzuteilen.

§9 Abs. 1 PromO

Ich versichere hiermit, dass die vorliegende Dissertation selbstständig und nur unter Verwendung der angegebenen Quellen verfasst wurde.

§9 Abs. 2 PromO

Die Arbeit hat bisher noch nicht zu Prüfungszwecken gedient.

Darmstadt, 28.05.2024

_____

Xiaofeng Wu

Contents

List of Figures

List of Tables

List of abbreviations

AEM	Adsorbate Evolution Mechanism
CBM	Conduction Band Minimum
DRIFTS	Diffuse Reflectance FT-IR Spectroscopy
EDL	Electrical Double Layer
EIS	Electrochemical Impedance Spectroscopy
HER	Hydrogen Evolution Reaction
IMPS	Intensity Modulated Photocurrent Spectroscopy
LCAO	Linear Combination of Atomic Orbitals
LOM	Lattice Oxygen Mechanism
MO	Molecular Orbitals
OCP	Open Circuit Potential
OEC	Oxygen Evolution catalysts
OER	Oxygen Evolution Reaction
OVs	Oxygen Vacancies
PEC	Photoelectrochemistry / Photoelectrochemical
PL	Photoluminescence
SCR	Space Charge Region
VBM	Valence Band Maximum
XRD	X-ray Diffraction
XPS	X-ray Photoelectron Spectroscopy

Abstract

Ternary bismuth-based oxides are regarded as promising photoanode materials in the field of photoelectrochemical water splitting due to their tunable structure and suitable energy band position. However, an in-depth understanding of bulk defects in structure-activity relationships and interfacial charge transfer kinetics is still lacking but needed for designing optimally functioning photoelectrodes.

In the present work, the impact of bulk oxygen vacancies (OVs) in BiOCl and the related induced shallow and deep defect states on the photocurrent was investigated. The results demonstrated that shallow defect states acting as electrons sinks can effectively accelerate separation of charge carriers and remarkably enhance the photocurrent, while deep lying surface states act as recombination centers and are detrimental to photocurrent.

Apart from BiOCl, the influence of Mo doping in $BiVO_4$ on photocurrent, photovoltage, and charge carrier dynamics was investigated. The results showed that both dark- and photocurrent densities of $BiVO_4$ in OER are dominantly limited by interfacial charge carrier resistance (R_{ct}) rather than bulk resistance (R_{bulk}). This conclusion confirms that the increase of bulk charge carrier concentration is not a decisive factor for improved OER performance of $BiVO_4$, which is consistent with the viewpoint that photocurrent of $BiVO_4$ is limited by surface recombination.

Based on the $BiVO_4$ results, we further proposed a semiconductor-electrolyte interface model, in which the surface accumulated hole density in $BiVO_4$ and Mo-doped $BiVO_4$ samples during water oxidation can be acquired via employing illumination-dependent Mott-Schottky measurements. According to this model, we demonstrate that the hole transfer rate remains linearly proportional to surface hole density on a log-log scale. Both water oxidation on $BiVO_4$ and Mo-doped $BiVO_4$ follow first-order reaction kinetics at low surface hole densities, which is in good agreement with literature. Besides, we find that water oxidation active sites in both $BiVO_4$ and Mo doped $BiVO_4$ are very likely to be Bi^{5+}, which are produced by photoexcited or/and electro-induced surface holes, rather than VO_x species or Mo^{6+} due to their insufficient redox potential for water oxidation. Our model gives a relatively complete physical image for generation and transfer of the photo(electro)-induced holes, as well as their accumulation and distribution within the space charge region (SCR) of semiconductors and surface hole-related water oxidation kinetics.

Zusammenfassung

Ternäre Oxide auf Wismut-Basis gelten aufgrund ihrer abstimmbaren Struktur und ihrer geeigneten Energiebandpositionen als vielversprechende Photoanodenmaterialien im Bereich der photoelektrochemischen Wasserspaltung. Ein tiefgreifendes Verständnis der Bulkdefekte in den Struktur-Aktivitäts-Beziehungen und der Grenzflächen-Ladungstransferkinetik fehlt jedoch noch, ist aber für die Entwicklung optimal funktionierender Photoelektroden erforderlich.

In der vorliegenden Arbeit wurden die Auswirkungen von Sauerstoffleerstellen (OVs) in BiOCl und die damit verbundenen flachen und tiefen Defektzustände auf den Photostrom untersucht. Die Ergebnisse zeigten, dass flache Defektzustände, die als Elektronensenken fungieren, die Trennung von Ladungsträgern effektiv beschleunigen und den Photostrom deutlich erhöhen können, während tief liegende Oberflächenzustände als Rekombinationszentren wirken und den Photostrom beeinträchtigen.

Neben BiOCl wurde der Einfluss der Mo-Dotierung in $BiVO_4$ auf den Photostrom, die Photospannung und die Ladungsträgerdynamik untersucht. Die Ergebnisse zeigten, dass sowohl die Dunkel- als auch die Photostromdichte von $BiVO_4$ in der OER hauptsächlich durch den Grenzflächen-Ladungsträgerwiderstand (R_{ct}) und nicht durch den Volumenwiderstand (R_{bulk}) begrenzt wird. Diese Schlussfolgerung bestätigt, dass die Erhöhung der Bulk-Ladungsträgerkonzentration kein entscheidender Faktor für eine verbesserte OER-Effizienz von $BiVO_4$ ist, was mit der Beobachtung übereinstimmt, dass der Photostrom von $BiVO_4$ durch Oberflächenrekombination begrenzt wird.

Auf der Grundlage der $BiVO_4$-Ergebnisse schlagen wir ein Halbleiter-Elektrolyt-Grenzflächenmodell vor, bei dem die an der Oberfläche akkumulierte Lochdichte in $BiVO_4$- und Mo-dotierten $BiVO_4$-Proben während der Wasseroxidation durch beleuchtungsabhängige Mott-Schottky-Messungen bestimmt werden kann. Mit diesem Modell zeigen wir, dass sich die Lochtransferrate linear proportional zur Oberflächen-Lochdichte auf einer log-log Skala verhält. Sowohl die Wasseroxidation auf $BiVO_4$ als auch Mo-dotiertem $BiVO_4$ folgen bei niedrigen Oberflächen-Lochdichten einer Reaktionskinetik erster Ordnung, was in guter Übereinstimmung mit der Literatur ist. Außerdem stellen wir fest, dass die aktiven Stellen für die Wasseroxidation sowohl in $BiVO_4$ als auch in Mo-dotiertem $BiVO_4$ sehr wahrscheinlich Bi^{5+} Spezies sind, die durch photoangeregte oder/und elektroinduzierte Oberflächenlöcher

erzeugt werden, und nicht VO_x-Spezies oder Mo^{6+} Spezies, da deren Redoxpotential für die Wasseroxidation nicht ausreicht. Unser Modell vermittelt ein relativ vollständiges physikalisches Bild der Erzeugung und des Transfers der photo(elektro)-induzierten Löcher sowie ihrer Akkumulation und Verteilung innerhalb der Raumladungszone (SCR) von Halbleitern und der mit Oberflächenlöchern verbundenen Wasseroxidationskinetik.

1. Introduction

This chapter introduces the background of photoelectrochemical water oxidation and emphasizes the importance of clean and sustainable energy, as well as the advantages of ternary bismuth-based metal oxides. The photoelectrochemical performance of inorganic oxide absorber materials is closely related to the behavior of photogenerated charge carriers. However, to date, there are still unanswered questions regarding photoelectrochemical reaction and interfacial charge transfer kinetics. Therefore, the aim of this dissertation is to study the influences of defects and doping on the concentration and interfacial dynamics of photogenerated charge carriers during the photoelectrochemical water oxidation reaction. The research objectives consist of the oxygen vacancies (OVs) related-structure activity relationship in BiOCl and the interfacial charge carrier dynamics in $BiVO_4$.

1.1 Research background

With the continuous growth of the world's population and the rapid development of science and technology, the global energy demand is increasing rapidly. It is estimated that the world's demand for primary energy will be about 30 and 46 TWh by 2050 and 2100, respectively.[1, 2] Traditional fossil fuels are limited and non-renewable. Moreover, the combustion of fossil resources releases a massive amount of carbon dioxide (CO_2), which is one of the main causes of global climate change. Based on the data from the global monitoring laboratory, the CO_2 concentration in the Earth's atmosphere has increased from 340 ppm in 1980 to 420 ppm in 2023.[3] Therefore, the development of a clean, carbon-neutral, and sustainable energy system is urgently needed.

Solar energy is considered as one of the most ideal energy sources due to its unlimited nature, sustainability and safety. However, one of the major challenges in using solar light is its intermittency. The efficiency of solar energy utilization is affected by the day-night cycle, weather conditions, and seasonal variations. To solve this problem, an attractive strategy is to convert solar energy into chemical energy, i.e., solar fuels with H_2 as the simplest chemical energy carrier. Hydrogen is a clean energy vector with the highest gravimetric energy density of all known substances.[4] For this reason, hydrogen energy as a replacement of traditional fossil energy sources is of great interest and potential in the transformation of our current energy system to a carbon-neutral, renewable energy system. Many countries and regions

had launched significant size projects to develop new technologies of hydrogen energy. For instance, Australia published an economically sustainable hydrogen energy policy in 2021.[5] The European Commission proposed a hydrogen energy plan in 2020 with the aim of providing secure, sustainable, and affordable energy to citizen.[6] Germany also put forward a national hydrogen strategy to emphasize the significance of green hydrogen in 2020.[7]

To date, the solar light-driven H_2 production can be realized by photocatalytic (PC) water splitting, photoelectrochemical (PEC) water splitting, photovoltaic electrochemical (PV-EC) water splitting, solar thermochemical (STC) water splitting, photothermal (PTC) catalytic CH_4 decomposition, and photobiological (PB) H_2 production.[8-13] Among these approaches, photoelectrochemical (PEC) and photovoltaic electrochemical (PV-EC) water splitting are ideal alternatives for H_2 production due to their relatively high theoretical solar to hydrogen (STH) efficiencies and corresponding large improvement margins (**Figure 1.1a**). However, the PV-EC combination brings about a great deal of CO_2 and SO_2 emissions, leading global warming potential (GWP) and acidification potential (AP). SO_2 emission mainly originates from the decomposition of Na_2SO_4 during the manufacture of the photovoltaic glasses. Considering the case of environmental protection, PEC water splitting is the most optimal technique for H_2 production. (**Figure 1.1b)**

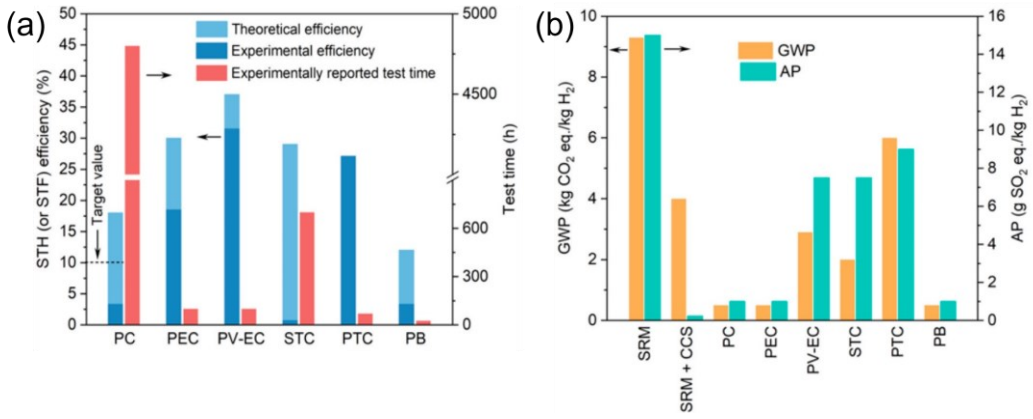

Figure 1.1 Theoretical and experimental efficiencies and the test time (a) of various solar light-driven H_2 production and their respective global warming potential (GWP) and acidification potential (AP) (b). [8]

Overall photoelectrochemical (PEC) water splitting comprises the photoanodic water oxidation reaction and the cathodic proton reduction reaction.[14] Since the hydrogen

evolution reaction (HER) is thermodynamically and kinetically simpler, water splitting efficiency is generally restricted by the O_2 evolution reaction (OER) at the photoanode due to its complex proton-coupled four-electron transfer reaction.[15, 16] Therefore, the investigation and development of photoanode materials is key to design overall water splitting concepts with optimal efficiency.

TiO_2 is a well-known binary photocatalytic oxide which is first reported by Fujishima and Honda in 1972.[17] it is readily available, non-toxic, and has an unprecedented stability. However, its large bandgap (3.2 eV) restricts its light-harvesting ability and intrinsic photon conversion efficiency. For example, the theoretical maximum photocurrent density and corresponding solar to hydrogen (STH) efficiency of anatase TiO_2 are estimated to be only 1.25~1.86 mA cm^{-2} and 1.8 % while those of Fe_2O_3 are estimated to be 12.4 mA cm^{-2} and 15.8 %, respectively (**Figure 1.2**). Accordingly, a bandgap matching the solar spectrum is essential for achieving high solar-to-H_2 efficiencies (STH).

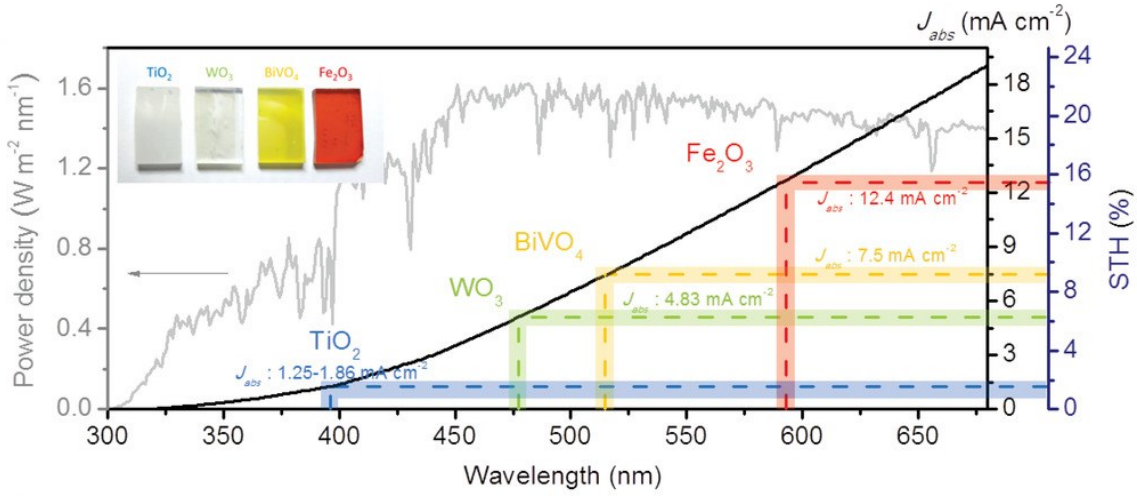

Figure 1.2 Theoretical photocurrent density (J_{abs}) and solar-to-hydrogen (STH) efficiency of TiO_2, WO_3, $BiVO_4$ and Fe_2O_3 under AM 1.5G solar light irradiation. Reproduced from reference [18] with permission of Wiley-VCH.

Despite of this, some unavoidable factors should be considered, such as the photochemical stability, the separation and migration efficiency of charge carriers, as well as surface photochemical reaction mechanisms. For example, Cu_2O is one of the most promising photocathode materials due to its small bandgap and superior photoelectrochemical performance. However, it is photo-transformed to CuO in air or aqueous solutions.

Accordingly, efforts have been devoted to surface protection to improve its long-term stability. For example, Tilley and co-workers reported that RuO_2-loaded Cu_2O/Al:ZnO/TiO_2 photoelectrodes exhibited ~100% Faradaic efficiencies and 94% stability after 8 h of chopped light illumination.[19]

In addition to the matching bandgaps and photochemical stabilities of photoabsorbers, their separation and migration efficiencies of charge carriers are essential. For instance, binary oxide α-Fe_2O_3 has an exceptional stability and a narrow bandgap of 2.0 eV. However, pristine α-Fe_2O_3 are subjected to a very short lifetime of charge carriers (~ 40 ps), leading to a practical maximum photocurrent of 4 mA cm^{-2} which is much lower than its theoretically achievable photocurrent density (12.4 mA cm^{-2}).[20]

Based on the above analysis, binary metal oxides rarely meet the requirements of highly efficient photoabsorbers. Therefore, numerous ternary metal oxides have been explored and are expected to be more promising semiconductors for photoelectrochemical water oxidation.

On the other hand, once a photoabsorber is given, the properties of the photogenerated charge carriers are of utmost significance, as they are directly related to the bulk separation and migration efficiency of the photoexcited charge carriers and the surface chemical reaction rates. However, up to now, the photogenerated charge carriers are difficult to be tracked due to their invisibility. As a result, the relevant photoelectrochemical reaction mechanisms remain elusive. Photoelectrochemical water splitting over semiconductors is like a black box. We can easily measure the photoelectrochemical performance, but the behavior of the charge carriers, such as their storage location, their concentration (especially the surface concentration) and the corresponding charge transfer kinetics, are key to open the black box. (**Figure 1.3**)

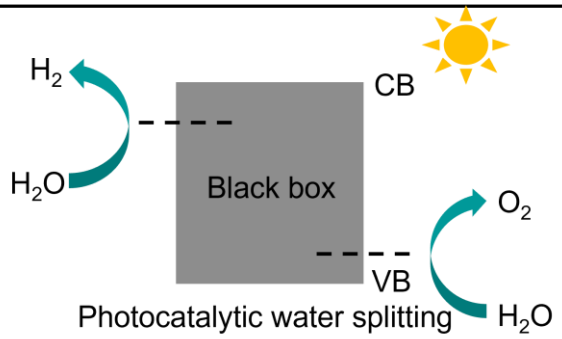

Figure 1.3 Schematic illustration of the photoelectrochemical water splitting process over a semiconductor.

In this dissertation, the ternary bismuth-based metal oxides BiOCl and $BiVO_4$ are employed as model catalysts because they are eco-friendly, structurally diverse and commonly used as photoanode materials in the PEC water oxidation system. Most importantly, they have a number of special advantages. For example, the OVs in BiOCl are easy to be generated and their concentration can be readily tuned, which is suitable for studying the effect of oxygen vacancies (OVs) on the nature of photoexcited charge carriers during the PEC water oxidation process. The concentration of the photogenerated holes in $BiVO_4$ under illumination is impressive and Mo doping is easy to be carried out due to the similar size of Mo ions and V ions. These properties are suitable for studying the effect of Mo doping on the concentration and surface dynamics of the photogenerated charge carriers.

1.2 Research objectives

High PEC water oxidation activities of photoanode materials closely depend on the behavior of the photogenerated charge carriers. Some defects (typically oxygen vacancies, OVs) can increase the concentration of charge carriers in the semiconductor, which in principle is conductive to their transfer. Nonetheless, some researchers argued that charge carriers trapped by OVs can reduce the charge carrier mobility, which is detrimental to their bulk transport.[21]

Besides, considering the energy band diagram, OVs will often create states at or near to the middle of the bandgap. The amount of OVs can affect their relative positions in the band alignment and corresponding roles in the catalytic process. Therefore, the relationships

between OVs, defect states and the catalytic activities are significant for an in-depth understanding of behavior of charge carriers. Unfortunately, the impacts of bulk OVs in BiOCl on defect states and photocatalytic performance are still unclear.

To address the above two issues, we intend to study the effect of oxygen vacancies in BiOCl on the charge carrier concentration and position of defect states, along with the PEC performance.

The second key challenge regarding charge carriers is to understand their transfer processes. The bulk and interfacial charge transfer processes can be reflected by the bulk resistance and interfacial charge transfer resistance, respectively. Generally, sample modification or light illumination can alter the values of these two resistances. These two physical quantities are simple, but they give us a relatively clear picture of the rate-determining step of the charge transfer process. This physical picture is helpful for us to further analyze the major limitations during the whole PEC water oxidation, such as bulk or interfacial recombination of photogenerated charge carriers, interfacial concentration of photogenerated charge carriers, photoelectrochemically active sites, etc.

For this purpose, undoped $BiVO_4$ and Mo-doped $BiVO_4$ photoanodes are chosen as model systems to understand the charge carrier kinetics from the aspect of interfacial charge transfer resistance.

The third intriguing but tough question concerning charge carriers is the energetics and thermodynamics of surface photoexcited charge carriers. Up to now, the detection and monitoring of the photoexcited charge carriers has been a very challenging and meaningful topic, which is essential to track the catalytic reaction mechanisms. Fortunately, some advanced instruments have been invented and applied in the field of catalysis. For instance, Li et al. first revealed the charge transfer process on the cuprous oxide photocatalyst on the femtosecond to second timescale by a home-made spatiotemporally resolved surface photovoltage spectroscopy.[22] Durrant et al. quantified the surface hole density and studied the water oxidation mechanism during the process over the hematite by photoinduced absorption spectroscopy.[23]

Despite these efforts, some issues regarding surface hole identification and quantification are still ambiguous. For instance, in the transition absorption study of $BiVO_4$, Durrant et al. assigned the broad photoinduced absorption in the range of 500 nm to 900 nm to the

photogenerated holes.[24, 25] This assignment is evidenced by the experiments of hole/electron scavengers and applied potentials.[26] However, they did not quantify the contribution of the photogenerated holes in the amplitude of photoinduced absorption signal. Additionally, the statement that the peak absorption at 550 nm is considered as the surface holes is also unconvincing. This is because the photogenerated holes accumulate within the space charge region, not only at the surface.

Therefore, we aim to setup a theoretical hole model with the consideration of accumulation of the photogenerated holes within space charge region. Based on this model, the surface hole concentration can be quantified according to the Fermi-Dirac distribution statistics. The interfacial charge carrier dynamics and thermodynamics are further investigated to understand the complex relationship between surface hole density, applied bias, (photo)electrochemically active sites and (photo)current density.

In a nutshell, influence of bulk OVs in BiOCl on the defect states and the photogenerated charge carriers is ambiguous. On the other hand, the study on the nature of the photogenerated charge carriers in $BiVO_4$ is significant and on the early stage. Current techniques, such as transient absorption spectroscopy (TAS), are not able to clearly resolve all issues regarding the behaviors of the photogenerated charge carriers due to some drawbacks and limitations. Herein, two modified bismuth-based ternary metal oxides (BiOCl-OVs and Mo-doped $BiVO_4$) are employed as model systems to investigate the effects of oxygen vacancies in BiOCl and Mo doping in $BiVO_4$ on the nature of the photogenerated charge carriers and their corresponding photoelectrochemical performance. We expect to comprehend the complicate relationship between OVs induced, defect states, concentration of photogenerated charge carriers and photocurrent in BiOCl. Besides, we expect to investigate the influence of Mo doping in $BiVO_4$ on the nature of the photogenerated charge carriers via setting up a general surface hole model and subsequent water oxidation kinetics and thermodynamics of the interfacial charge carrier transfer processes.

1.3 Thesis overview

In Chapter 2, the basic concepts and theories related to semiconductors and photoelectrochemistry are introduced. Finally, the crystalline structures, physical properties and modification strategies of the investigated materials BiOCl and $BiVO_4$ are presented.

In Chapter 3, the sample preparation procedures and the main characterization methods are presented including UV-Vis-NIR absorption spectroscopy, X-ray photoelectron spectroscopy (XPS), electrochemical impedance spectroscopy (EIS) and intensity modulated photocurrent spectroscopy (IMPS).

In Chapter 4, the influence of OVs in BiOCl on defect states, carrier concentrations and photoelectrochemical performance is systematically investigated. The photocurrent of BiOCl is mainly limited by the synergistic effect of charge carrier concentration (conductivity) and shallow defect states induced by bulk oxygen vacancies. The shallow defect states can not only effectively increase the light absorption but also further increase the photogenerated carrier concentration leading to an enhancement in the photoelectrochemical performance of BiOCl.

In Chapter 5, $BiVO_4$ (BVO) and molybdenum doped $BiVO_4$ (Mo-BVO) film samples are investigated. The promoting effect of Mo doping in $BiVO_4$ on the photocurrent density is studied via various characterization methods including photovoltage, electrochemical impedance spectroscopy, and intensity modulated photocurrent spectroscopy (IMPS). In particular, the analysis of bulk resistance (R_{bulk}) and charge transfer resistance (R_{ct}) provides a visual understanding of the main limitations of $BiVO_4$ during water oxidation.

In Chapter 6, a surface hole model is proposed, in which the surface accumulated hole densities in BVO and Mo-BVO samples during water oxidation are determined by employing illumination-dependent Mott-Schottky measurements. The interplay between surface hole density and photocurrent is systematically studied and described. Furthermore, we infer that the active sites for photoelectrochemical water oxidation in both BVO and Mo-BVO samples are Bi^{5+} rather than VO_x or Mo^{6+} species by combining the redox potential with the variation of the reaction rate constants. The Mo doping in Mo-BVO sample inhibits the surface charge carrier recombination and indirectly increases the formation of Bi^{5+} active species.

References

[1] A.K. Hussein, Applications of nanotechnology in renewable energies—A comprehensive overview and understanding, *Renew. Sustain. Energy Rev.*, **2015**, *42*, 460-476.

[2] F.M. Sapountzi, J.M. Gracia, C.J. Weststrate, H.O.A. Fredriksson, J.W. Niemantsverdriet, Electrocatalysts for the generation of hydrogen, oxygen and synthesis gas, *Prog. Energy Combust. Sci.*, **2017**, *58*, 1-35.

[3] Trends in Atmospheric Carbon Dioxide, https://gml.noaa.gov/ccgg/trends/global.html

[4] K.T. Møller, T.R. Jensen, E. Akiba, H.-w. Li, Hydrogen - A sustainable energy carrier, *Prog. Nat. Sci.: Mater. Int.*, **2017**, *27*, 34-40.

[5] The National Hydrogen Roadmap provides a blueprint for the development of a hydrogen industry in Australia, October 20, **2021**, https://www.csiro.au/en/research/environmental-impacts/fuels/hydrogen/Hydrogen-Roadmap.

[6] A hydrogen strategy for a climate-neutral Europe, July 8, **2020**, https://ec.europa.eu/commission/presscorner/api/files/attachment/865942/EU_Hydrogen_Strategy.pdf.

[7] National Hydrogen Strategy: Green hydrogen as energy source of the future, June, **2020**, https://www.bmbf.de/bmbf/en/news/national-hydrogen-strategy.html.

[8] H. Song, S. Luo, H. Huang, B. Deng, J. Ye, Solar-Driven Hydrogen Production: Recent Advances, Challenges, and Future Perspectives, *ACS Energy Lett.*, **2022**, *7*, 1043-1065.

[9] J.H. Kim, D. Hansora, P. Sharma, J.W. Jang, J.S. Lee, Toward practical solar hydrogen production - an artificial photosynthetic leaf-to-farm challenge, *Chem. Soc. Rev.*, **2019**, *48*, 1908-1971.

[10] Q. Wang, K. Domen, Particulate Photocatalysts for Light-Driven Water Splitting: Mechanisms, Challenges, and Design Strategies, *Chem. Rev.*, **2019**, *120*, 919-985.

[11] T. Pregger, D. Graf, W. Krewitt, C. Sattler, M. Roeb, S. Möller, Prospects of solar thermal hydrogen production processes, *Int. J. Hydrogen Energy*, **2009**, *34*, 4256-4267.

[12] S. Luo, X. Ren, H. Lin, H. Song, J. Ye, Plasmonic photothermal catalysis for solar-to-fuel conversion: current status and prospects, *Chem. Sci.*, **2021**, *12*, 5701-5719.

[13] M.Y. Azwar, M.A. Hussain, A.K. Abdul-Wahab, Development of biohydrogen production by photobiological, fermentation and electrochemical processes: A review, *Renew. Sustain. Energy Rev.*, **2014**, *31*, 158-173.

[14] M.A. Marwat, M. Humayun, M.W. Afridi, H. Zhang, M.R. Abdul Karim, M. Ashtar, M. Usman, S. Waqar, H. Ullah, C. Wang, W. Luo, Advanced Catalysts for Photoelectrochemical Water Splitting, *ACS Appl. Energy Mater.*, **2021**, *4*, 12007-12031.

[15] J. Yang, D. Wang, H. Han, C. Li, Roles of Cocatalysts in Photocatalysis and Photoelectrocatalysis, *Acc. Chem. Res.*, **2013**, *46*, 1900-1909.

[16] T. Palaniselvam, L. Shi, G. Mettela, D.H. Anjum, R. Li, K.P. Katuri, P.E. Saikaly, P. Wang, Vastly Enhanced $BiVO_4$ Photocatalytic OER Performance by $NiCoO_2$ as Cocatalyst, *Adv. Mater. Interfaces*, **2017**, *4*, 1700540.

[17] A. Fujishima, K. Honda, Electrochemical Photolysis of Water at a Semiconductor Electrode, *Nature*, **1972**, *238*, 37-38.

[18] J.H. Kim, J.S. Lee, Elaborately Modified $BiVO_4$ Photoanodes for Solar Water Splitting, *Adv. Mater.*, **2019**, *31*, 1806938.

[19] S.D. Tilley, M. Schreier, J. Azevedo, M. Stefik, M. Graetzel, Ruthenium Oxide Hydrogen Evolution Catalysis on Composite Cuprous Oxide Water-Splitting Photocathodes, *Adv. Funct. Mater.*, **2013**, *24*, 303-311.

[20] A.G. Joly, J.R. Williams, S.A. Chambers, G. Xiong, W.P. Hess, D.M. Laman, Carrier dynamics in α-Fe_2O_3 (0001) thin films and single crystals probed by femtosecond transient absorption and reflectivity, *J. Appl. Phys.*, **2006**, *99,* 053521.

[21] R. Gegevičius, M. Franckevičius, V. Gulbinas, The Role of Grain Boundaries in Charge Carrier Dynamics in Polycrystalline Metal Halide Perovskites, *Eur. J. Inorg. Chem.*, **2021**, *35*, 3519-3527.

[22] R. Chen, Z. Ren, Y. Liang, G. Zhang, T. Dittrich, R. Liu, Y. Liu, Y. Zhao, S. Pang, H. An, C. Ni, P. Zhou, K. Han, F. Fan, C. Li, Spatiotemporal imaging of charge transfer in photocatalyst particles, *Nature*, **2022**, *610*, 296-301.

[23] F. Le Formal, E. Pastor, S.D. Tilley, C.A. Mesa, S.R. Pendlebury, M. Gratzel, J.R. Durrant, Rate law analysis of water oxidation on a hematite surface, *J. Am. Chem. Soc.*, **2015**, *137*, 6629-6637.

[24] Y. Ma, S.R. Pendlebury, A. Reynal, F. Le Formal, J.R. Durrant, Dynamics of photogenerated holes in undoped $BiVO_4$ photoanodes for solar water oxidation, *Chem. Sci.*, **2014**, *5*, 2964-2973.

[25] Y. Ma, C.A. Mesa, E. Pastor, A. Kafizas, L. Francàs, F. Le Formal, S.R. Pendlebury, J.R. Durrant, Rate Law Analysis of Water Oxidation and Hole Scavenging on a $BiVO_4$ Photoanode, *ACS Energy Lett.*, **2016**, *1*, 618-623.

[26] A.J. Cowan, J. Tang, W. Leng, J.R. Durrant, D.R. Klug, Water Splitting by Nanocrystalline TiO_2 in a Complete Photoelectrochemical Cell Exhibits Efficiencies Limited by Charge Recombination, *J. Phys. Chem. C*, **2010**, *114*, 4208-4214.

2. Theoretical background

This chapter presents the relevant fundamental concepts and theories, aiming at deeply understanding the basic physical properties of semiconductors and their photoelectrochemical water splitting mechanisms, including the energy band theory and optical properties of the semiconductor, the electrical double layer, the semiconductor solid-electrolyte junction and the mechanism of photoelectrochemical water oxidation. At the end of this chapter, the structure-activity relationships of bismuth oxychloride (BiOCl) and bismuth vanadate ($BiVO_4$) are reviewed.

2.1 Basic theory of semiconductors

2.1.1 Energy band evolution

In solid state physics, solids can be classified into conductors (metals), semiconductors and insulators, based on their bandgaps and conductivities. Metals typically possess excellent conductivity with a zero bandgap while insulators have an extremely low conductivity with a bandgap typically greater than 4.0 eV. The conductivities and bandgaps of semiconductors fall in between. Energy band theory provides a good description for the physical properties of semiconductors. The energy band theory is usually considered to be an extension of the Linear Combination of Atomic Orbitals (LCAO) concept. The crystal structure of semiconductors consists of many primitive cells. For instance, the number of Si atoms in crystalline Si reaches up to 5×10^{22} cm^{-3}. From a chemical point of view, analyzing the evolution process of energy bands of a few atoms in a single unit cell by LCAO is reasonable and helpful for understanding the nature of semiconductors due to the periodic crystal structure of solid semiconductors. [1]

For simplicity, we take silicon as an example to describe the energy band evolution process. The core levels (1*s*, 2*s*, and 2*p*) of Si are occupied with electrons, which leads to the formation of full-filled bands in the energy band of Si according to the LCAO model (**Figure 2.1**). The formation of valence band and conduction band is only relevant to the outer valence electrons of the Si atom. The outer electron configuration of the Si atom is $3s^2 3p^2$. The four valence orbitals of a Si atom produce four equivalent sp^3 hybrid orbitals, when they bond to four other Si atoms. Each hybrid orbital is occupied by an electron. The atomic orbitals will overlap when two Si atoms approach each other. The closer the two interacting atoms get, the greater gets

the orbital overlap. The overlap of equivalent hybrid orbitals gives rise to two split energy levels which are called bonding (σ) and anti-bonding (σ*) molecular orbitals (MO), respectively. According to the Pauli principle and Hund's rules, two single electrons from two equivalent sp^3 hybrid orbitals fill into the σ-bonding orbital while the anti-bonding orbital is empty.

As mentioned above, numerous Si atoms exist in a real Si crystal. Consequently, the occupied σ bonding orbital and the empty σ* anti-bonding orbital will further form a full-filled valence band and an empty conduction band, respectively.

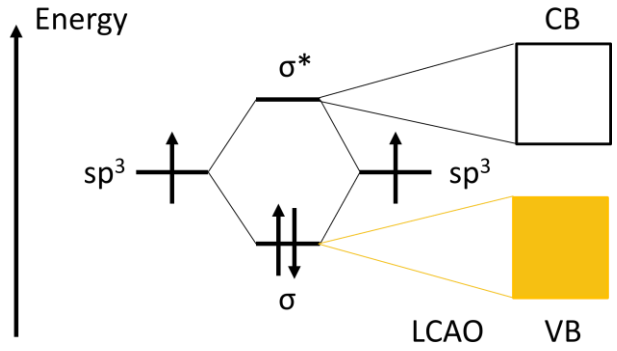

Figure 2.1 Energy band evolution of Si from sp^3 hybrid atomic orbitals to valence band and conduction band.

The evolution of the BiOCl band structure can be analyzed in a similar way. The ternary oxide BiOCl is a layered structure consisting of $[Bi_2O_2]^{2+}$ slabs and Cl^- ions. The structural unit cell of BiOCl is illustrated in **Figure 2.2**. Both O and Cl atoms are bonded to Bi atoms. The Bi-O and Bi-Cl bond lengths are 2.32 Å and 3.05 Å, respectively. Therefore, the interaction of Bi-O bonds is stronger than that of Bi-Cl bonds. The other atomic interactions such as Bi-Bi and Cl-Cl atoms are very weak due to their relatively large distances (typically greater than 3.5 Å). The electron configurations of the Bi, O and Cl atoms are $[Xe]4f^{14}5d^{10}6s^26p^3$, $[He]2s^22p^4$ and $[Ne]3s^23p^5$, respectively. In the BiOCl crystal, the valence states of Bi, O and Cl are +3, −2 and −1, respectively. As a result, the electron configurations of the Bi^{3+}, O^{2-} and Cl^- ions are $[Xe]4f^{14}5d^{10}6s^2$, $[He]2s^22p^6$ and $[Ne]3s^23p^6$, respectively.

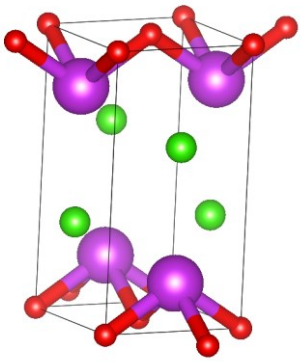

Figure 2.2 The unit cell of bismuth chloride, showing the bismuth (purple), oxygen (red) and chlorine (green) atoms, respectively.

The empty 6p atomic orbitals of the Bi^{3+} ions interact with the full-filled 2p orbitals of the O^{2-} ions and the 3p orbitals of the Cl^{-} ions, respectively. The corresponding bonding and anti-bonding molecular orbitals (MOs) are formed. Since the atomic distance of the Bi^{3+} and O^{2-} ions is larger than that of Bi^{3+} and Cl^{-} ions, the splitting energy of Bi-O MO is larger than that of Bi-Cl MO. Furthermore, the bonding MO are mainly derived from the 2*p* atomic orbitals of O^{2-} ions and 3*p* atomic orbitals of Cl^{-} ions while the anti-bonding MO are mainly derived from the empty 6*p* atomic orbitals of Bi^{3+} ions.[2] These MO form the valence band and conduction band of the BiOCl crystal via LCAO rules. The energy band evolution process of BiOCl is presented in **Figure 2.3**.

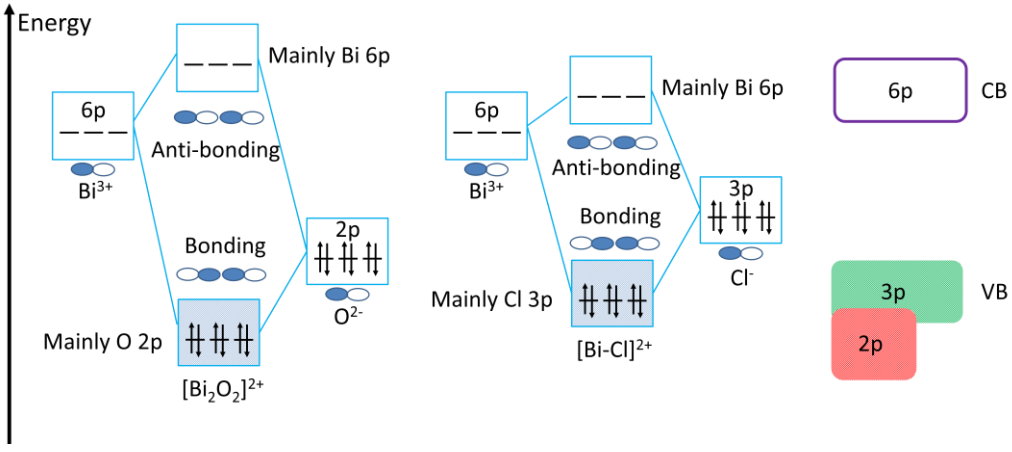

Figure 2.3 Energy band evolution of BiOCl from valence atomic orbitals to valence band (VB) and conduction band (CB) according to the LCAO concept.

The cell structure of monoclinic $BiVO_4$, shown in **Figure 2.4**, is more complicate than that of BiOCl. Herein, we analyze the energy band evolution of $BiVO_4$ from the atomic orbitals of the Bi^{3+}, O^{2-} and V^{5+} ions according to the LCAO rules. The electron configurations of the Bi^{3+}, O^{2-} and V^{5+} ions are $[Xe]4f^{14}5d^{10}6s^2$, $[He]2s^22p^6$ and $[Ne]3s^23p^6$, respectively. The Bi and V atoms are bonded to O atoms. Unlike the BiOCl structure, two Bi-O bond lengths (1.69 Å and 1.77 Å) and four V-O bond lengths (2.354 Å, 2.372 Å, 2.516 Å and 2.628 Å) are presented in the monoclinic $BiVO_4$ structure.

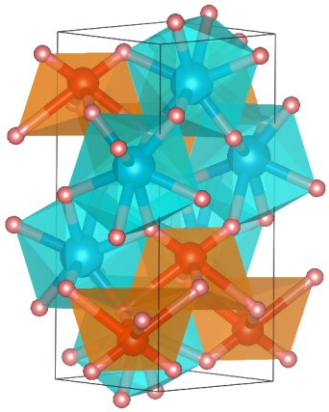

Figure 2.4 The cell structure of monoclinic bismuth vanadate, showing the bismuth (large, blue), oxygen (small, red) and vanadium (middle, light red) atoms, respectively.

Despite of the various bond distances in monoclinic $BiVO_4$, the V-O bond lengths are remarkably shorter than the Bi-O bond lengths, suggesting that the interaction of V-O bonds is stronger than that of B-O bonds. The full-filled 2*p* orbitals of the O^{2-} ions interact with the empty 3*d* atomic orbitals of the V^{5+} ions and the full-filled 6*s* orbitals of the Bi^{3+} ions, respectively. Accordingly, the gap of the spitting energy levels (formed bonding and anti-bonding orbitals) in V-O bonds is larger than in Bi-O bonds. In addition, the 3*d* orbital energy level of V^{5+} ion is higher than the 6s orbital energy level of the Bi^{3+} ion due to its higher valence states. Therefore, the VBM and CBM of monoclinic $BiVO_4$ are mainly composed of V^{5+} 3*d* orbitals and Bi 6*s* orbitals, respectively. The energy band evolution process of monoclinic $BiVO_4$ is illustrated in **Figure 2.5**.

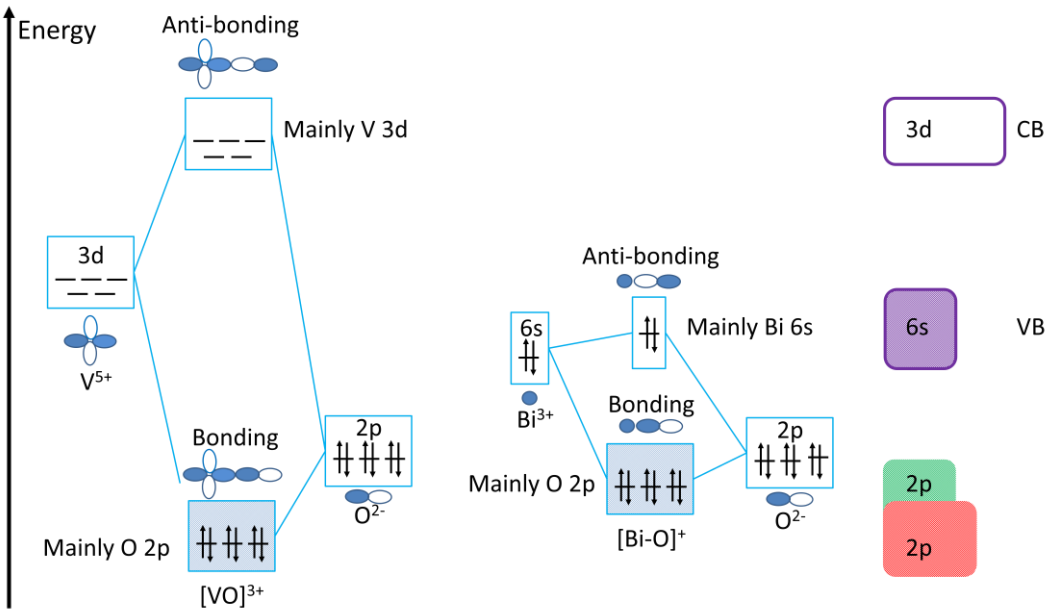

Figure 2.5 Energy band evolution of monoclinic $BiVO_4$ from valence atomic orbitals to valence band (VB) and conduction band (CB) according to the LCAO concept.

2.1.2 Optical properties

In a semiconductor, the energy difference between valence band maximum (VBM) and the conduction band minimum (CBM) is called the bandgap. Electrons at the VBM can be excited to the conduction band and become free electrons under illumination. In this process, if the VBM and CBM are located at the same *k* vector, a direct optical transition occurs without a change in crystal momentum (*k* vector). In contrast, an indirect optical transition is accompanied with a change of crystal momentum. A prerequisite for indirect optical transitions is the excitation of a phonon (i.e., a lattice vibration). The direct and indirect optical transitions in semiconductors are schematically represented in **Figure 2.6**. Since nature light carries little crystal momentum, it is difficult for indirect semiconductors to absorb photons directly. Accordingly, indirect semiconductors usually have much lower light absorption coefficients, compared to direct semiconductors. For example, the absorption coefficients at 1.8 eV of crystalline Si (indirect semiconductor) and $CuIn_{0.7}Ga_{0.3}Se_2$ (direct semiconductor) are 4×10^3 cm^{-1} and 10^5 cm^{-1}, respectively. This explains why the thickness of crystalline Si (~300 μm) in solar cells is commonly much larger than that of other direct semiconductors (<10 μm), used in thin film PV technology.

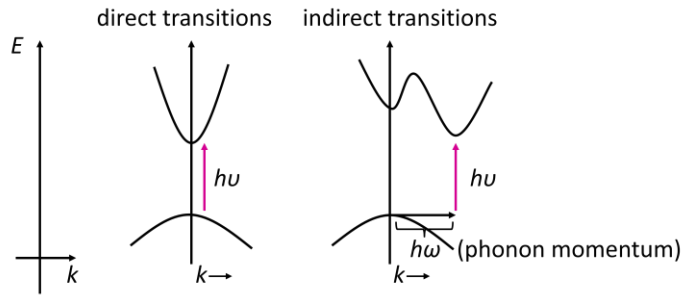

Figure 2.6 Direct (left) and indirect (right) optical transitions of semiconductors. Reproduced from reference [3] with permission of Springer Nature.

The absorption coefficient of the semiconductor is normally measured by UV-vis absorption spectroscopy and can be expressed by equation 2.1.

$$\alpha = A\frac{(h\upsilon - E_g)^m}{h\upsilon} \quad \text{(eqn. 2.1)}$$

A is a proportionality constant, α is the absorption coefficient, *hv* is the photon energy, E_g is the bandgap, *m* is relevant to the optical nature of the semiconductor. *m* = 2 implies an indirect bandgap and *m* = 1/2 implies a direct bandgap. The bandgaps and the types of semiconductors can be determined by plotting the absorption coefficient versus photon energy (the so-called Tauc plot).[4] The resulting plot usually has a linear regime, which can be extrapolated to the abscissa. The optical bandgap of the semiconductor is obtained directly from the intersection point.

2.2 Electrical double layers (EDL)

To investigate electron transfer reactions at the electrode-electrolyte interface, we need to know the transport and accumulation of electrons and the adsorption of ions at the actual solid-electrolyte interface. So far, many solid-liquid interface models have been proposed to explain the electrochemical behaviors of electrodes. Here we introduce the origin of electrical double layers from three models below.

The concept of the EDL was first put forward by Hermann von Helmholtz in 1853.[5] In his model, the EDL interface was simply described by a parallel plate capacitor. The ions surrounded by solvent molecules, are assumed to closely approach the surface of the

electrode and form a charged layer. Meanwhile, opposite charges are attracted to the surface of the electrode to balance the electrical charges of the ions. This model described the solid-liquid interface well but did not consider the adsorption of ions at the surface of electrode and the diffusion of ions in the solution. Louis Georges Gouy[6] in 1910 and David Leonard Chapman[7] in 1913 found that the capacitance was relevant to the ion concentration and the applied bias. They thus proposed a diffuse layer model, later called the Gouy-Chapman model. The charge distribution of the ions depends on the distance from the electrode surface and follows the Maxwell-Boltzmann statistics. Therefore, the potential drops exponentially as the distance between the ions and the electrode surface increases. Unfortunately, the Gouy-Chapman theory is only valid at low ion concentrations. Otto Stern combined the two models in 1924.[8] In the Stern model, some ions are in proximity to the electrode surface and form the Helmholtz layer while some other ions form the diffuse layer. Sketch maps of three models are described in **Figure 2.7**.

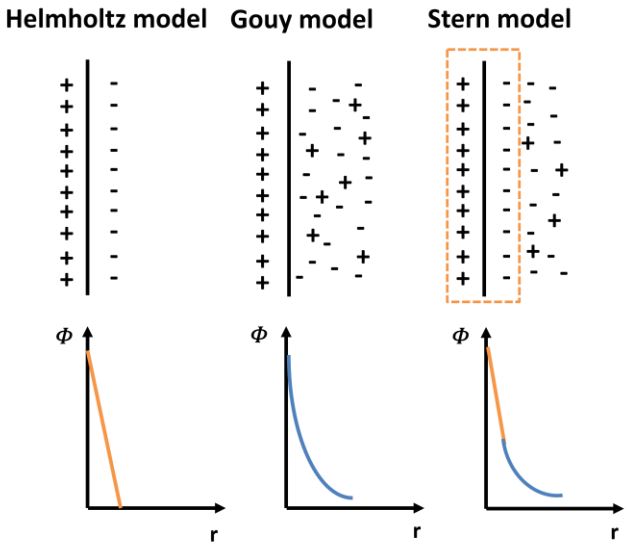

Figure 2.7 Sketch maps of the Helmholtz, Gouy-Chapman, and Stern models, describing the solid-liquid interface, the potential versus distance curves in the Helmholtz model (orange), the Gouy-Chapman model (blue) and the Stern model (orange and blue) are linear, non-linear, and partially linear respectively.[5, 6, 8]

After that, many scientists improved the solid-liquid interface model based on the Stern model. Nowadays, the widely accepted electrical double layer model is illustrated in **Figure 2.8**. This model is still incomplete in terms of the energy levels, density of states and chemical

species, etc., but it is successful in the description of solvated ions and interfacial adsorption of ions. In this model, the nearest layer to the metal electrode surface is called the compact layer or Helmholtz layer which comprises solvent molecules and sometimes specifically adsorbed ions and molecules. The location of the specifically adsorbed ions is denoted as the inner Helmholtz plane (IHP), while the location of the closest solvated ions is called the outer Helmholtz plane (OHP). The diffusion layer is composed of these non-specifically adsorbed solvated ions. Assuming that the total charge densities of the electrode surface, the IHP and the diffusion layer are q^M, σ^i and σ^d, respectively, the following equation describes charge neutrality.

$$q^M = \sigma^i + \sigma^d \quad \text{(eqn. 2.2)}$$

Normally, the thickness of the Helmholtz layer is very small (typically a few Å). The thickness of the diffusion layer is less than 100 Å, when the ion concentration is larger than 10^{-2} M.[9] Metals usually have high free electron concentrations, which can compensate for the potential drops with dipoles instead of the band bending after contact with the electrolyte. For example, the electron concentration of silver is 5.86×10^{22} cm^{-3}, which is much larger than that of semiconductors.[10] Therefore, very thin interface thickness in silver are required to maintain the potential drops. In other words, the thickness of the space charge layer of a metal is extremely thin and the potential drop between the metal and the electrolyte is completely distributed across the electrical double layer, mainly the Helmholtz layer. If a sufficiently high potential is applied to the metal electrode, an extremely high electric field (up to 10^9 V m^{-1}) is generated within the very narrow Helmholtz layer. Such a high electric field thus accelerates the charge transfer to the solution and decomposes the water into oxygen and hydrogen.[10]

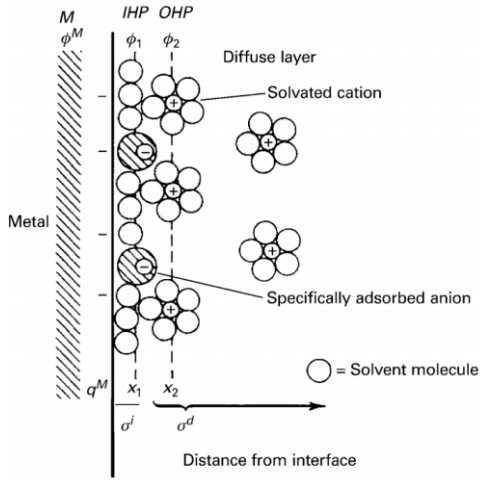

Figure 2.8 Proposed model of the electric double layer at the solid-liquid interface of a metal. Reproduced from reference [9] with permission of Wiley-VCH.

As mentioned above, a semiconductor has a lower electron concentration. When in contact with an electrolyte, the surface electron concentration of the semiconductor is unable to form dipoles to overcome the potential drop between the semiconductor and the electrolyte. As a result, the bulk electrons of the semiconductor flow towards the surface and, in the meantime, band bending occurs within the space charge region to align the Fermi levels of the semiconductor and the redox electrolyte. This process is illustrated in **Figure 2.9**. The semiconductor-electrolyte junction will be further elaborated below.

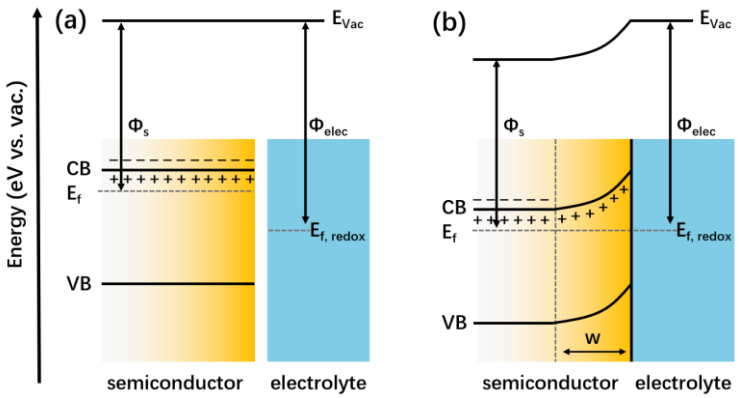

Figure 2.9 Schematic of an n-type semiconductor before (a) and after contacting (b) with an electrolyte. The shallow ionized donor species and free electrons are denoted as "+" and "-" markers, respectively. Φ_s and Φ_{elec} are the work functions of the semiconductor and the redox electrolyte. *w* is the width of the space charge layer.

2.3 Semiconductor-electrolyte junction

To analyze the distribution of potential and charge in the semiconductor-electrolyte junction, we take an n-type semiconductor immersed in a solution with a high ion concentration as an example. Accordingly, the diffusion layer is not considered. Assuming that the bulk hole and electron concentrations in the semiconductor are p_0 and n_0, respectively, the surface hole and electron concentrations are p_s and n_s, and can be expressed as follows:

$$p_s = p_0 \exp\left(\frac{e\phi_{sc}}{kT}\right) \quad \text{(eqn. 2.3)}$$

$$n_s = n_0 \exp\left(-\frac{e\phi_{sc}}{kT}\right) \quad \text{(eqn. 2.4)}$$

$e\phi_{sc}$ is the band bending in the space charge layer. The value of ϕ_{sc} depends on the applied potential. When ϕ_{sc} is zero, the corresponding potential is the flat band potential (U_{fb}) of the photoelectrode. The capacitance of the space charge layer C_{sc} is a function of ϕ_{sc} and the corresponding relationship is illustrated in **Figure 2.10a**. The whole potential region can be divided into three parts (accumulation, depletion, and inversion region), based on the value of ϕ_{sc}.

Envisioning that we apply a potential to make ϕ_{sc} negative, this means that the photoelectrode has a downward band bending within the space charge layer. Under these circumstances, electrons in the CBM tend to flow to the surface and holes in the VBM tend to flow to the bulk. When $e\phi_{sc}$ is greater than 3 kT, n_s is twenty times higher than n_0. Herein, this region is called the *accumulation region* of charge carriers.

When the applied bias is changed to shift the bandgap diagram downwards, the photoelectrode has a positive ϕ_{sc} value, i.e., the band bending of the space charge region is upward, if $e\phi_{sc}$ is smaller than half of the bandgap of the semiconductor. The electron concentration at the surface is smaller than that in the bulk, but the hole concentration at the surface is larger than that in the bulk. In this region, both hole and electron concentrations at the surface are very limited because the Fermi level of the semiconductor approaches to the surface mid-gap of the semiconductor. This region is known as the *depletion region*.

Note that, if the applied potential is increased further, the band bending will be larger than half of the bandgap. As a result, the holes become the majority carriers at the surface. the surface electron concentration is much lower than that in the bulk, but the surface hole

concentration is larger than that in the bulk. Since the surface hole concentration is an exponential function of the applied potential, it will increase sharply with increasing the applied potential in this region. This region is called the *inversion region*.

The three situations described above are visualized in **Figure 2.10b**.

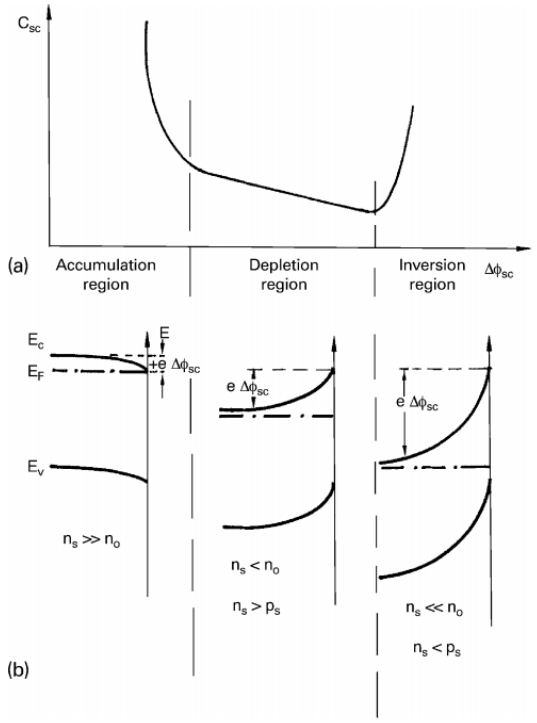

Figure 2.10 Space charge layer capacitance C_{sc} versus $\Delta\phi_{sc}$ curve (a) and corresponding band diagrams (b) of accumulation, depletion, and inversion region at an n-type semiconductor-electrolyte interface. Reproduced from reference [11] with permission of Wiley-VCH.

The formation process of the semiconductor-electrolyte junction can be described as follows: Free electrons in the semiconductor will flow to the electrolyte after contacting due to the difference of their work functions. The charge transfer reaches equilibrium until the Fermi level of the semiconductor is equal to that of the redox electrolyte. Band bending and a space change region in the semiconductor are subsequently formed to compensate the loss of electrons during the process. The width of the space charge region can be determined by Poisson's equation.

$$\frac{d^2V}{dx^2} = \begin{cases} -\frac{\rho}{\varepsilon_0\varepsilon_s}, & 0 \le x \le w \\ 0, & x > w \end{cases} \quad \text{(eqn. 2.5)}$$

V is the potential, ρ is the charge density, ε_0 is the vacuum dielectric constant (8.85×10^{-12} F m^{-1}), ε_s is the relative dielectric constant of the semiconductor, *w* is the width of the space charge region. Here, the position at the solid-electrolyte interface is defined as zero, *x* is the position of a certain point in the bulk semiconductor. The charge density ρ can be defined as follows:

$$\rho = eN_D \quad \text{(eqn. 2.6)}$$

e is the elementary charge (1.602×10^{-19} C), N_D is the donor density. The electric field and the electric potential at position *x* are denoted by *E*(x) and *V*(x), respectively, and can be expressed by the following equations:

$$E(x) = -\frac{dV}{dx} = -\frac{eN_D}{\varepsilon_0\varepsilon_s}(x - w) \quad \text{(eqn. 2.7)}$$

$$V(x) = \int E(x)dx = -\frac{eN_D}{2\varepsilon_0\varepsilon_s}(x^2 - 2xw) - \phi_{sc} \quad \text{(eqn. 2.8)}$$

eϕ_{sc} is the band bending of the space charge region resulting from the difference between the redox Fermi level position of the electrolyte ($E_{f,redox}$) and the work function of the semiconductor (eϕ_s) before contact.

$$e\phi_{sc} = E_{f,redox} - e\phi_s \quad \text{(eqn. 2.9)}$$

Note, that we neglect the potential drop within the electrical double layer(ϕ_{dl}), because ϕ_{sc} is usually much larger than ϕ_{dl} in the depletion layer region. The electrical potentials *V*(0) and *V*(*w*) are calculated as follows:

$$V(0) = -\phi_{sc} \quad \text{(eqn. 2.10)}$$

$$V(w) = \frac{eN_D}{2\varepsilon_0\varepsilon_s}w^2 - \phi_{sc} \quad \text{(eqn. 2.11)}$$

The potential difference in the space charge region between the surface and the depth *w* in the semiconductor is easily obtained.

$$\phi_{sc} = V(w) - V(0) = \frac{eN_D}{2\varepsilon_0\varepsilon_s}w^2 \quad \text{(eqn. 2.12)}$$

The space charge region capacitance C_{sc} can be defined as:

$$C_{sc} = \frac{\varepsilon_0 \varepsilon_s}{w} \quad \text{(eqn. 2.13)}$$

By combing eqn. 2.12 with eqn. 2.13, $\frac{1}{C_{sc}^2}$ is obtained as a function of ϕ_{sc}.

$$\frac{1}{C_{sc}^2} = \frac{w^2}{\varepsilon_0^2 \varepsilon_s^2} = \frac{2}{eN_D \varepsilon_0 \varepsilon_s} \phi_{sc} \quad \text{(eqn. 2.14)}$$

$$\phi_{sc} = U - U_{fb} - \frac{kT}{e} \quad \text{(eqn. 2.15)}$$

Where U is the applied potential, U_{fb} is the flat band potential, k is the Boltzmann constant (1.38×10 m^2 kg s^{-2} K^{-1}), and T is the temperature in Kelvin.

Finally, the so-called Mott-Schottky equation can be derived from eqn. 2.14 and eqn. 2.15.

$$\frac{1}{C_{sc}^2} = \frac{w^2}{\varepsilon_0^2 \varepsilon_s^2} = \frac{2}{eN_D \varepsilon_0 \varepsilon_s} (U - U_{fb} - \frac{kT}{e}) \quad \text{(eqn. 2.16)}$$

In addition, the width of the space charge region can be described by the following equation:

$$w = [\frac{2\varepsilon_0 \varepsilon_s}{eN_D} \left(U - U_{fb} - \frac{kT}{e}\right)]^{\frac{1}{2}} \quad \text{(eqn. 2.17)}$$

2.4 Photoelectrochemical water splitting

Photoelectrochemical water splitting is a promising way to produce CO_2-neutral hydrogen. A photoelectrochemical cell consists of at least a photoelectrode and a dark counter electrode, other designs involving a photoanode and a photocathode have been reported as well. **Figure 2.11** describes the basic constitution of a simple photoelectrochemical cell, which includes a photoanode and dark metal cathode. Both electrodes are immersed in an electrolyte and connected by conductive wires. The photoanode can absorb light and generate holes in the VB and electrons in the CB. The holes will oxidize water on the surface of the photoanode, while the electrons move to the cathode and reduce H^+ (acidic media) or H_2O (alkaline media) to form H_2. The reactions at the cathode and photoanode can be written as follows:

Cathode: $2\mathrm{H}^+ + 2\mathrm{e}^- \xrightarrow{\square} \mathrm{H}_2$ (acidic media)

or $2\mathrm{H}_2\mathrm{O} + 2\mathrm{e}^- \xrightarrow{\square} 2\mathrm{OH}^- + \mathrm{H}_2$ (alkaline media)

Photoanode: $2\mathrm{H}_2\mathrm{O} + 4\mathrm{h}^+ \xrightarrow{\square} 4\mathrm{H}^+ + \mathrm{O}_2$ (acidic media)

or $4OH^- + 4h^+ \rightarrow 2H_2O + O_2$ (alkaline media)

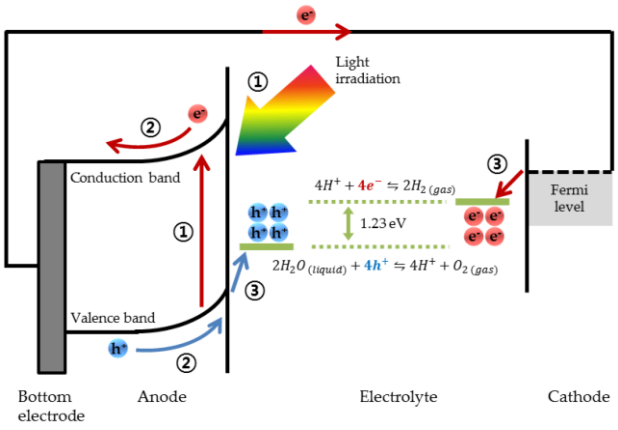

Figure 2.11 Schematic diagram of a typical photoelectrochemical cell, composed of a photoanode and a dark metal cathode.[12]

2.4.1 Mechanism of photoelectrochemical OER

Compared to HER, the OER process is usually much slower due to the required four electron transfer steps. In order to design highly efficient OER catalysts, an in-depth understanding of the OER mechanism is needed. Two different mechanisms involving water oxidation at the surface of catalysts have been widely accepted. i.e., adsorbate evolution mechanism (AEM) and lattice oxygen mechanism (LOM).

Adsorbate Evolution Mechanism (AEM)

In this mechanism, catalysts only provide active sites for water (acidic solution) or OH^- (alkaline solution) adsorption. After reactant adsorption, subsequent processes are initiated at the surface of the catalyst, including charge transfer, chemical bond cleavage/formation, adsorption/desorption of surface intermediates, and generation of oxygen molecules. The oxygen evolution can be expressed by the following equations (**Figure 2.12**).

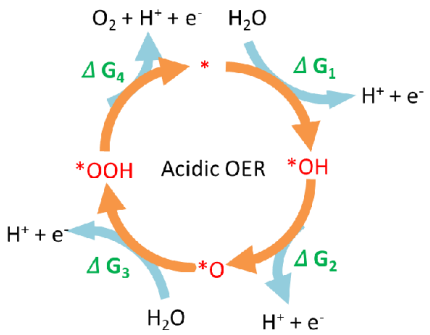

Acidic solution:

$$H_2O\ (l) + {}^{*} \rightarrow OH^{*} + H^{+} + e^{-}$$

$$^{*}OH \rightarrow O^{*} + H^{+} + e^{-}$$

$$O^{*} + H_2O(l) \rightarrow {}^{*}OOH + H^{+} + e^{-}$$

$$^{*}OOH \rightarrow * + O_2(g) + H^{+} + e^{-}$$

Figure 2.12 Four elementary reaction steps of OER in acidic solution, where $\Delta G_{1\text{-}4}$ indicates the required Gibbs free energy of each reaction.

Since bismuth-based semiconductor oxides are likely to be unstable in acidic media, we only describe the alkaline OER process here as an example. As demonstrated in **Figure 2.13**, firstly, a OH^- group is adsorbed on an active site and forms adsorbed OH*. Subsequently, another OH^- group reacts with adsorbed OH*, which produce O* and a water molecular. A third OH^- group then undergoes a nucleophilic attack on O* to yield *OOH. Finally, a fourth OH^- group reacts with *OOH to release *, water and oxygen molecules.

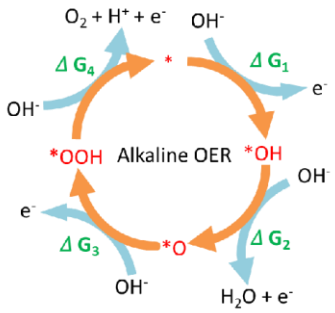

Alkaline solution:

$$OH^{-} + {}^{*} \rightarrow OH^{*} + e^{-}$$

$$OH^{-} + {}^{*}OH \rightarrow O^{*} + H_2O(l) + e^{-}$$

$$O^{*} + OH^{-} \rightarrow {}^{*}OOH + e^{-}$$

$$OH^{-} + {}^{*}OOH \rightarrow * + O_2(g) + H_2O(l) + e^{-}$$

Figure 2.13 Four elementary reaction steps of OER in alkaline solution, where $\Delta G_{1\text{-}4}$ indicates the required Gibbs free energy of each reaction.

Theoretically, this process overall requires a potential of 1.23 V vs. RHE, but the four elementary reactions can have individually different redox potentials.[13, 14] An ideal OER catalyst requires that four elementary reactions have the same Gibbs free energy (namely, 1.23 eV). However, this is impossible to be achieved due to the linear correlation of adsorption energies of surface oxygen species (O*, *OH and *OOH). For instance, the binding energy difference of *OH and *OOH ($\Delta G_{OOH^*} - \Delta G_{OH^*}$) is a constant of 3.2 ± 0.2 eV, independent of

catalysts and adsorption sites. The reason for this is that either *OH or *OOH is connected to an adsorption site of the catalyst by an oxygen atom single bond.[15] Since the first and fourth elementary reaction steps rarely possess the highest potential in most OER catalysts, the potential of OER is determined by the second or third elementary step and can be expressed as follows:

$$\eta^{OER} = \max\left\{\frac{\Delta G_{O^*} - \Delta G_{OH^*}}{e}, \frac{\Delta G_{OOH^*} - \Delta G_{OH^*}}{e}\right\} \text{ (eqn. 2.18)}$$

$$\eta^{OER} = \max\left\{\frac{\Delta G_{O^*} - \Delta G_{OH^*}}{e}, \frac{3.2\ \text{eV} - (\Delta G_{O^*} - \Delta G_{OH^*})}{e}\right\} \text{ (eqn. 2.19)}$$

Therefore, the potential (η^{OER}) is a function of ΔG_{O^*} -ΔG_{OH^*}. Here, the volcano plot of OER can be described as η^{OER} vs. ΔG_{O^*} -ΔG_{OH^*}. η^{OER} would reach a theoretical minimum potential (1.6 V) when ΔG_{O^*} -ΔG_{OH^*} = 1.6 V. Under these circumstances, the theoretical minimum value is 0.37 V.

Of note, based on the relationship between potential (η^{OER}) and ΔG_{O^*} -ΔG_{OH^*}, some strategies are dedicated to optimizing the value of ΔG_{O^*} -ΔG_{OH^*} for indirect control of η^{OER}, including introduction of vacancies,[16] strain tuning,[17] interface engineering,[18] heteroatom doping.[19]

Lattice oxygen mechanism (LOM)

During the development of OER catalysts, it was found that some catalytic phenomena involving OER cannot be interpreted by AEM. For example, the OER catalytic activities of some catalysts are dependent on the pH value of the solution, and they do not follow the typical potential-Gibbs free energy volcano plot.[20, 21] Accordingly, LOM has been proposed and widely accepted to explain the above-mentioned pH-dependence.

LOM is usually accompanied with the generation of oxygen vacancies (OVs) originating from the lattice oxygen of catalysts, which is different from a single metal active site in AEM. Since the lattice oxygen of catalysts in LOM directly acts as active sites and produces oxygen molecules in the OER, we can differentiate the AEM and LOM by an O^{18} isotope labelling approach. The typical LOM materials include $NiCo_2O_4$, $Li_xCo_{3-X}O_4$, cobalt phosphate and spinel oxides etc.[22-24] The LOM can be demonstrated in **Figure 2.14**.[25]

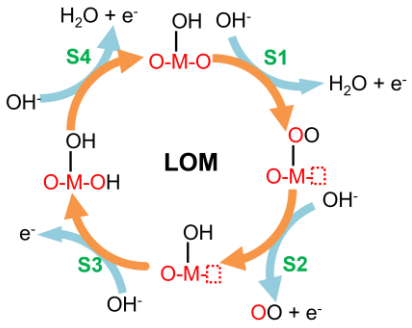

Figure 2.14 Schematic diagram of the proposed lattice oxygen mechanism (LOM), dashed boxes represent the oxygen vacancies.

2.5 Properties and applications of the studied materials

2.5.1 Bismuth oxychloride (BiOCl)

2.5.1.1 Crystal and electronic structure

Bismuth oxyhalides, usually denoted as BiOX (X=Cl, Br or I), are a series of V-VI-VII compounds. They have similar crystal structures which consist of $[Bi_2O_2^{2+}]$ layers and halogen ions (Cl^-, Br^- or I^-), as depicted in **Figure 2.15**. Bismuth oxyhalides have the same tetragonal matlockite (PbFCl-type) crystal structure and space group (P4/nmm). The detailed crystal structure parameters of bismuth oxyhalides are summarized in **Table 2.1**.[26] Bi and O atoms in $[Bi_2O_2^{2+}]$ layers are bonded by covalent bonds and O atoms and halogen atoms are attracted by van den Waals interactions.[27] The a, b and c values in the primitive cell increase from BiOCl, BiOBr to BiOI due to the increased radii of the halogen ions.

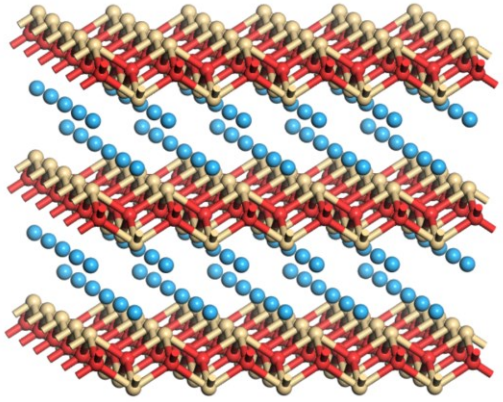

Figure 2.15 The crystal structure of bismuth oxyhalides, bismuth atoms (brown), oxygen atoms (red) and halogen atoms (blue) are presented, respectively.

Table 2.1 The space group and crystal parameters of bismuth oxyhalides.[28]

	Space group	a (Å)	b (Å)	c (Å)	α (°)	β (°)	γ (°)	JPCDS No.
BiOCl	P4/nmm	3.883	3.883	7.347	90.00	90.00	90.00	06-0249
BiOBr	P4/nmm	3.915	3.915	8.076	90.00	90.00	90.00	73-2061
BiOI	P4/nmm	3.984	3.984	9.128	90.00	90.00	90.00	73-2062

The valence band maximum of bismuth oxyhalides is mainly composed of O 2*p* orbitals and *X np* orbitals (*n*=3, 4, and 5 corresponding to *X*=Cl, Br, and I, respectively), while their conduction band minimum is composed of Bi 6*s* states. The energy level positions of *X np* states are generally higher than O 2p, as described in **Figure 2.16**.[2] Hence, the contribution of the *X np* states determines the valence band position. The VBM of bismuth oxyhalides will shifts upwards as *X* becomes larger,[26] explaining the band gap order of bismuth oxyhalides: BiOCl (3.4 eV) > BiOBr (2.8 eV) > BiOI (1.8 eV).[29]

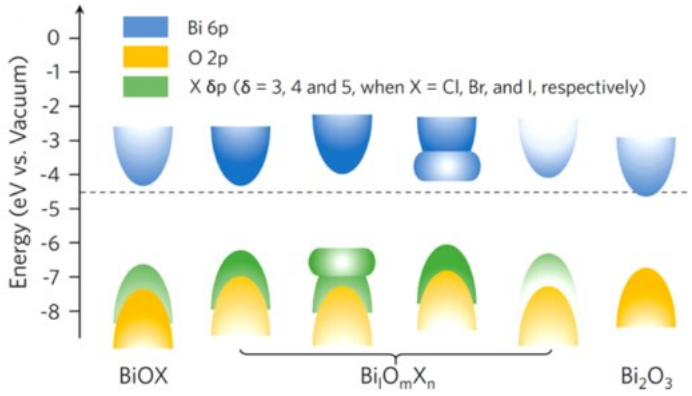

Figure 2.16 The energy band lineup of bismuth oxyhalides. Reproduced from reference [2] with the permission of American Chemical Society.

The transfer properties of charge carriers in the semiconductors are highly dependent on their effective masses. The effective masses of holes and electrons in bismuth oxyhalides are given in **Table 2.2**. Bismuth oxyhalides have much larger effective masses of electrons and holes perpendicular to the $[Bi_2O_2^{2+}]$ layers (m_z), as compared to m_x and m_y. This means that both electrons and holes are difficult to transfer to the surface along the z-axis (i.e.,[001] direction]). Although the diffusion lengths of carriers in bismuth oxyhalides along the z-direction have not been reported yet, they are supposed to be very small. Therefore, reducing the thickness of bismuth oxyhalides with exposed (001) facet is an effective approach to improve their photocatalytic activity. For instance, Zhang et al. reported that (001) crystal facets in BiOCl exhibited higher photodegradation activity than (010) crystal facets under UV light irradiation.[30] The higher activity of (001) facets was attributed to the surface structure and a suitable internal electric field.[30]

Table 2.2 Effective masses of electrons and holes in bismuth oxyhalides, "L" in the effective masses indicates very large value.[31]

	Effective masses of electrons (m_e)				Effective masses of holes (m_e)			
	m*	m_x	m_y	m_z	m*	m_x	m_y	m_z
BiOCl	0.39	0.29	0.29	1.15	1.33	0.95	0.95	6.31
BiOBr	0.36	0.24	0.24	L	1.72	1.26	1.26	6.15
BiOI	0.29	0.19	0.19	L	0.70	0.51	0.51	L

Since only BiOCl is investigated in this thesis, I will outline merits and drawbacks of BiOCl and corresponding strategies for improvement below. Firstly, single crystalline BiOCl nanosheets can be facilely synthesized via a hydrothermal method due to the weak interaction between $[Bi_2O_2^{2+}]$ layers and Cl^-.[27] BiOCl has a suitable valence band position which can oxidize organic pollutants and water.[32, 33] The main advantage of BiOCl is readily generated oxygen vacancies (OVs) under UV light illumination or thermal treatment in O_2 free condition, which creates an ideal platform to investigate the influence of OVs.[27, 34, 35] Additionally, the unique internal electric field of BiOCl resulting from its layered structure is beneficial to separate the charge carriers.[30]

The main drawback of BiOCl is insufficient light absorption owning to its large bandgap (3.2-3.4 eV), which implies a low theoretical photocurrent (500 μA cm^{-2}) under AM 1.5G solar light illumination. Moreover, BiOCl is an indirect semiconductor, which leads to a limited utilization of the photons. Indirect and direct optical transitions of BiOCl occur at 3.2 eV and 3.6 eV, respectively. The second limitation of BiOCl is severe recombination of charge carriers. The introduction of OVs in BiOCl can increase its light absorption due to defect states and enhance the adsorption and activation of small molecules (H_2O, CO_2 etc.) originating from the induced local electric field polarization.[32]

2.5.1.2 Approaches to improve photoelectrochemical properties of BiOCl

Modification of photocatalysts is typically considered from three aspects: light absorption, separation and migration of charge carriers, and interfacial charge carrier transfer.

Introducing other halogen ions (Br^- and I^-) into BiOCl is an elegant way to reduce the bandgap. The reason for this is that Br^- and I^- can shift the valence band, as elaborated previously. It is worth noting that this method differs from heteroatom doping because it barely creates any defects in the crystal lattice of BiOCl. In addition, heteroatom doping usually requires relatively harsh conditions, whereas the introduction of Br^- and I^- ions into BiOCl is facilely achieved and the ratio of halogen ions can be tuned over a wide range.[36, 37]

Doping with foreign atoms can also increase the photon absorption ability and conductivity of BiOCl. However, the doping of heteroatoms into $[Bi_2O_2^{2+}]$ layers is generally accompanied with a high symmetry change of the layer structure, resulting in poor thermal stability of the heteroatoms as well as some unavoidable crystal defects.[36] These crystal defects can trap holes or electrons and accelerate the charge carrier recombination.

Tuning internal electric fields is a general approach to facilitate separation of charge carriers in BiOCl, including bulk built-in electric field and interfacial electric field. Bulk self-induced electric field between $[Bi_2O_2^{2+}]$ slabs and Cl^- ions in BiOCl can accelerate charge carrier transfer along the direction perpendicular to $[Bi_2O_2^{2+}]$ slabs and Cl^- ions and can be enhanced by percentage of exposed (001) facets and doping.[36] For example, Zhang et al. found that the photoactivity of Bi_3O_4Cl is strongly dependent on percentage of exposed (001) facets due to the strong induced internal electric field.[38] Moreover, the internal electric field in Bi_3O_4Cl can be enhanced by non-metal doping, such as C, P, S, N, F and Br, as suggested by theoretical calculations.[39] The strength of the internal electric field of Bi_3O_4Cl increased by 126 times after 3.16% C doping and its bulk charge separation efficiency greatly increased from 0.6% to 80%.[39] This result indicates that mediating the internal electric field of layered materials is a promising way to restrain bulk charge carrier recombination.

The interfacial electric field of BiOCl can be tuned by the construction of heterojunctions. Nonetheless, appropriate band alignments of the heterojunctions must be considered. For instance, loading a semiconductor with a high work function onto BiOCl will cause an electron flow and a resulting interfacial electric field from BiOCl to the semiconductor. In addition to

the work function, suitable valence band and conduction band positions are also important for the photogenerated charge carrier transport.

The transfer of surface charge carriers is a crucial step in (photo)electrochemical reactions. For the photocatalytic water oxidation reaction, the valence band position of BiOCl is thermodynamically able to oxidize water molecules. However, bare BiOCl shows an unsatisfactory photocatalytic performance due to the relatively high overpotential of the rate-limiting step during water oxidation and the high surface recombination of charge carriers. it has been reported that introducing surface oxygen vacancies at the (010) facet of BiOCl can decrease the required overpotential of water oxidation and facilitate the dissociation of water molecules on OVs.[32] Besides, surface OVs in BiOCl have also been applied to the photocatalytic NO oxidation,[40] photocatalytic CO_2 reduction[41] and the degradation of organic compounds.[42] Although surface OVs have been widely studied in the field of photocatalysis and photo(electro)chemistry, the studies of bulk OVs in BiOCl are relatively rare. Obviously, bulk OVs in BiOCl can also significantly affect its light absorption, charge carrier recombination and photo(electro)chemical performance. Therefore, the influence of bulk OVs in BiOCl will be investigated in Chapter 4 of this thesis.

2.5.2 Bismuth vanadate ($BiVO_4$)

2.5.2.1 Crystal and electronic structure

$BiVO_4$ is a promising photoanode for photoelectrochemical water oxidation due to its suitable band gap and chemical stability. In general, $BiVO_4$ has four crystal forms: pucherite, dreyerite and clinobisvanite and tetragonal scheelite. Their crystal structures are shown in **Figure 2.17**.

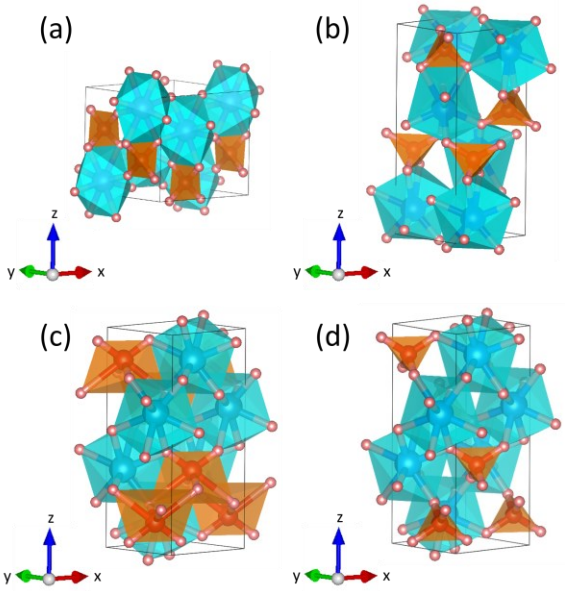

Figure 2.17 Four crystal structures of $BiVO_4$: (a) pucherite (orthorhombic), (b) dreyerite (tetragonal zircon), (c) clinobisvanite (monoclinic scheelite) and (d) tetragonal scheelite.[43, 44]

Tetragonal scheelite $BiVO_4$ can reversibly phase-transformed to the monoclinic scheelite structure at 255 °C. The tetragonal zircon structure can be irreversibly converted to monoclinic scheelite structure during heat treatment at 400-500 °C. The thermal phase transformation of monoclinic scheelite, tetragonal zircon and tetragonal scheelite structure is illustrated in **Figure 2.18**.

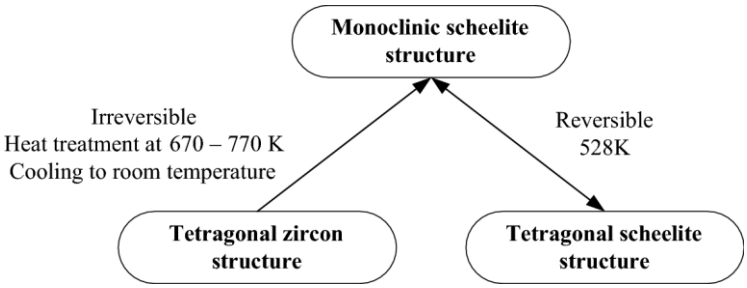

Figure 2.18 Thermal phase transformation of $BiVO_4$. Reproduced from reference [45] with the permission of American Chemical Society.

All $BiVO_4$ polymorphs consist of V-O tetrahedra and Bi-O dodecahedra, but the bond lengths of V-O and Bi-O are different. For instance, the V-O bond length in a V-O tetrahedron is 1.73 Å and the Bi-O bond lengths in Bi-O dodecahedra are 2.4 Å and 2.47 Å in a tetragonal scheelite structure. However, the crystal structure of the monoclinic scheelite $BiVO_4$ is more distorted. The V-O bond lengths are 1.69 Å and 1.76 Å, while the Bi-O bond lengths are 2.35 Å and 2.37 Å, 2.52 Å and 2.63 Å. This distortion enhances local polarization, charge carrier separation and therefore leads to a higher photocatalytic activity.[45] The space groups and crystal parameters of all $BiVO_4$ polymorphs are summarized in **Table 2.3**.

Table 2.3 The space group and the crystal parameters of pucherite, dreyerite and clinobisvanite.[44, 46-49]

	Space group	*a* (Å)	*b* (Å)	*c* (Å)	*α* (°)	*β* (°)	*γ* (°)	JCPDS No.
Pucherite (Orthorhombic)	Pnca	5.332	5.063	12.02	90.00	90.00	90.00	12-0293
Dreyerite (Tetragonal zircon)	$I4_1/amd$	7.303	7.303	6.584	90.00	90.00	90.00	14-0133
Clinobisvanite (Monoclinic scheelite)	I I 11 2/b	5.195	5.094	11.704	90.00	90.00	90.40	14-0688
Tetragonal scheelite	$I4_1/a$	5.147	5.147	11.722	90.00	90.00	90.00	75-2481

The photocatalytic activity of $BiVO_4$ is closely relevant to its electronic structure. Kudo et al. found that monoclinic $BiVO_4$ showed much higher photocatalytic activity than zircon type $BiVO_4$.[50] Since the bandgaps of monoclinic $BiVO_4$ and zircon $BiVO_4$ are 2.4 eV and 2.9 eV, they hypothesized that the improved photocatalytic property is resulted from enhanced absorption of photons.[50] The valence band of zircon-type $BiVO_4$ mainly consists of O 2p

orbitals while that of scheelite $BiVO_4$ is composed of Bi 6s orbitals (or hybrid Bi 6s and O 2p orbitals). The photon absorption in zircon type $BiVO_4$ occurs only between occupied O 2p and empty V 3*d* orbitals. In contrast, the valence band electrons in scheelite $BiVO_4$ can be excited from occupied Bi 6s (or hybrid Bi 6s and O 2p orbitals) to empty V 3*d* orbitals. The band structures of zircon-type and scheelite $BiVO_4$ are illustrated in **Figure 2.19**. However, Zhao et al. reported that the optical transition from the occupied Bi 6*s* orbital to the empty V 3*d* orbital in scheelite $BiVO_4$ is rather impossible due to the large spatial distance between the V and Bi atoms (3.61 Å~3.85 Å).[51] Normally, the interaction between two neighboring atoms is considered to be very weak when their distance is larger than 3.00 Å.[52] They confirmed that crystal distortion increased the impact of Bi 6*s* states in scheelite $BiVO_4$ by density functional theory calculations.[51] This factor pushes the occupied O 2*p* upwards and thus decreases the band gap. As a consequence, the transition behavior of electrons in scheelite $BiVO_4$ is the same as that in zircon type $BiVO_4$, excited from occupied O 2*s* states to unoccupied V 3*d* states.[51] On the other hand, as mentioned above, this crystal distortion leads to local polarization of the Bi-O tetrahedra and increases the charge separation in the scheelite $BiVO_4$, which contributes to the high photocatalytic activity.[45]

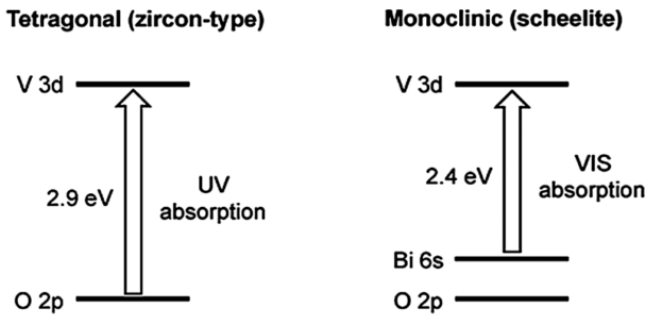

Figure 2.19 Band structures of tetragonal zircon and scheelite $BiVO_4$.Reproduced from references [50] with the permission of American Chemical Society.

Additionally, the effective masses of holes and electrons in monoclinic $BiVO_4$ are 0.7 m_0 and 0.9 m_0, respectively.[51] Nevertheless, the effective masses of holes and electrons in zircon type $BiVO_4$ are 1.2 m_0 and 17.3 m_0, respectively.[49] The lighter effective masses of charge carriers in monoclinic scheelite $BiVO_4$ imply their larger charge carrier mobilities and longer diffusion lengths to reach the interface. As a consequent, the excellent photocatalytic performance of scheelite $BiVO_4$ is attributed to its lighter effective masses of charge carriers.

Superior photocatalytic performance of photocatalysts requires not only a wide range of light absorption but also a large light absorption coefficient. The monoclinic scheelite $BiVO_4$ has a small bandgap (2.4 eV) which can absorb visible light. Moreover, it, as an indirect semiconductor,[53, 54] shows an exceptionally high absorption coefficient (10^{-7} m^{-1}). The reason for the high absorption coefficient is that the required energy for the direct optical transition is only 200 meV higher than that for the indirect optical transition. In other words, the direct optical transition in monoclinic scheelite $BiVO_4$ is very easy to occur, accompanied with its indirect optical transition.

2.5.2.2 Approaches to improve photoelectrochemical properties

High photon absorption is essential for superior photoabsorbers, but improving photon utilization (i.e., reducing charge carrier recombination) is also significant. The theoretical maximum photocurrent and corresponding solar to hydrogen (STH) generation efficiency of monoclinic $BiVO_4$ under AM 1.5G solar light stimulation are 7.5 mA cm^{-2} and 9.2%, respectively.[55, 56] However, bare $BiVO_4$ photoelectrodes without modification usually have small photocurrents.

$BiVO_4$ is dominantly limited by its poor charge carrier mobility.[57] Effective masses and carrier mobilities of some typical photocatalytic semiconductors are summarized in **Table 2.4**.

Table 2.4 Effective masses and carrier mobilities of selected semiconductors at 298 K.

	Effective masses of carriers		Mobilities of carriers		References
	Electrons (m_e)	Holes (m_e)	Electrons ($cm^{-2}V^{-1}s^{-1}$)	Holes ($cm^{-2}V^{-1}s^{-1}$)	
Si	/	/	1500	450	[58]
ZnO	0.24	0.45	200	180	[59]
Anatase TiO_2	> 10	0.80	2×10^{-3}	/	[60, 61]
WO_3	0.9	/	10	/	[62]
CdS	0.19	0.80	720	40	[59]
$BiVO_4$	/	/	0.2	0.044	[63, 64]

In contrast to other semiconductors, the carrier mobilities of monoclinic $BiVO_4$ are relatively small, which implies short carrier diffusion lengths. The diffusion lengths of electrons and holes can be estimated according to the following equation.

$$L_D = \sqrt{\frac{kT}{e}\tau\mu} \quad \text{(eqn. 2.20)}$$

Where L_D is the diffusion length of charge carriers, k is the Boltzmann constant, T is the temperature in Kelvin, e is the elementary charge, μ and τ are the mobility and lifetime of charge carriers, respectively.[65] For example, if the lifetime of holes is 40 ns, the diffusion length of holes will be ~70 nm.[66]

Short carrier diffusion length is unfavorable to separate photogenerated charge carriers and photocatalytic activities of semiconductors. To overcome this drawback, some works are dedicated to control the sizes and morphologies of $BiVO_4$. For instance, Fu et al. reported that core-shell hollow sphere $BiVO_4$ exhibited much higher visible photodegradation activity of Rhodamine B as compared to that of plate-like $BiVO_4$.[67] In fact, hollow nanostructured $BiVO_4$ not only shortens the required diffusion length of holes but also increases the specific surface area. Besides hollow structures, many morphologies such as worm-like, plate and nanorod $BiVO_4$ have been synthesized so far.[68-70]

An alternative approach to alleviate the disadvantages of small carrier mobilities is to increase the conductivity of $BiVO_4$ (i.e., the concentration of charge carriers) by doping.[63, 71, 72] The most effective doping elements for increasing conductivity of $BiVO_4$ are W and Mo, because the radii of the W^{6+} (74 pm) and Mo^{6+} (73 pm) ions are similar to that of the V^{5+} (68 pm). Doping can increase the light absorption and the conductivity of semiconductors, but excessive doping will create deeply trapped energy levels and narrow the depletion layer significantly increasing charge carrier recombination. Therefore, balancing unfavorable and favorable impacts of doping is essential.

The second limitation of $BiVO_4$ is relevant to the sluggish water oxidation due to the multielectron transfer process.[73] This viewpoint is also supported by experiments with hole scavengers, such as methanol,[74, 75] sulfites,[76, 77] carbonates,[78, 79] and hydrogen peroxide.[57, 80] The photocurrent of $BiVO_4$ is significantly enhanced in the presence of these hole scavengers, as they are more easily oxidized than water. The accumulation of holes gives rise to their increased recombination at the surface. Loading oxidation evolution co-catalysts is an elegant way to alter the reaction pathways and reduce the required activity energy of water oxidation.[81, 82] The most commonly used oxygen evolution cocatalysts are located in the VIII B group including iron-based cocatalysts (FeOOH),[83] cobalt-based cocatalysts (CoO_x, Co_3O_4,$Co_3(PO_4)_2$),[84-86] nickel-based cocatalysts (NiO_x, NiOOH, $NiBO_3$),[87] MnO_x, Pt, RuO_x and IrO_x.[82] The deposition of oxygen evolution cocatalysts can significantly accelerate the charge transfer from the semiconductor to the solution, implying that the slow water oxidation process can be solved after loading an effective OEC. For instance, Wang et al. reported that the surface charge transfer efficiency of $BiVO_4$ increased from 23.2% to 71.4% at 1.23 V_{RHE} after the deposition of $NiCoO_2$.[88]

The combination of various modification methods of $BiVO_4$ can greatly enhance its photocurrent, even approaching the theoretical maximum photocurrent. For instance, the photocurrent of $BiVO_4$ achieved 2.73 mA cm^{-2} at a potential of 0.6 V_{RHE}, by applying double oxygen evolution catalyst (OEC) layers (FeOOH and NiOOH) and its nanostructure, as reported by Choi et al.[76] To date, the highest photocurrent of $BiVO_4$ is 6.72 mA cm^{-2} under AM 1.5G solar light stimulation at 1.23 V_{RHE} which corresponds to 90% of its theoretical maximum value.[70] In this article, the authors subtly combined the advantages of heterojunction ($BiVO_4$-WO_3), morphology control (nanorods) and deposition of OEC (Co-Pi).

References

[1] R. Hoffmann, How Chemistry and Physics Meet in the Solid State, *Angew. Chem. Int. Ed.*, **1987**, *26* 846-878.

[2] J. Li, H. Li, G. Zhan, L. Zhang, Solar Water Splitting and Nitrogen Fixation with Layered Bismuth Oxyhalides, *Acc. Chem. Res.*, **2017**, *50*, 112-121.

[3] Photoelectrochemical Hydrogen Production, Springer, **2012**, p 17.

[4] R. Kerremans, C. Kaiser, W. Li, N. Zarrabi, P. Meredith, A. Armin, The Optical Constants of Solution‐Processed Semiconductors-New Challenges with Perovskites and Non‐Fullerene Acceptors, *Adv. Opt. Mater.*, **2020**, *8*, 2000319.

[5] H. Helmholtz, Ueber einige Gesetze der Vertheilung elektrischer Ströme in körperlichen Leitern mit Anwendung auf die thierisch-elektrischen Versuche, *Annalen der Physik*, **1853**, *165*, 363-377.

[6] M. Gouy, Sur la constitution de la charge électrique à la surface d'un électrolyte, *Journal de Physique Théorique et Appliquée*, **1910**, *9*, 457-468.

[7] D.L. Chapman, LI. A contribution to the theory of electrocapillarity, *The London, Edinburgh, and Dublin Philosophical Magazine and Journal of Science*, **2010**, *25*, 475-481.

[8] O. Stern, Zur Theorie Der Elektrolytischen Doppelschicht, *Und Angewandte Physikalische Chemie*, **1924**, *30*, 508-516.

[9] Electrochemical methods: Fundamentals and Applications, Second Edition, John Wiley & Sons, Inc., **2001**.

[10] Interfacial_Electrochemistry, Second Edition, Springer-Verlag Berlin Heidelberg, **2010**, p 4.

[11] Semiconductor Electrochemistry, Second Edition, Wiley-VCH, **2015**, p 98.

[12] S. Jeong, J. Song, S. Lee, Photoelectrochemical Device Designs toward Practical Solar Water Splitting: A Review on the Recent Progress of $BiVO_4$ and $BiFeO_3$ Photoanodes, *Appl. Sci.*, **2018**, *8*, 1388.

[13] H.N. Nong, L.J. Falling, A. Bergmann, M. Klingenhof, H.P. Tran, C. Spöri, R. Mom, J. Timoshenko, G. Zichittella, A. Knop-Gericke, S. Piccinin, J. Pérez-Ramírez, B.R. Cuenya, R.

Schlögl, P. Strasser, D. Teschner, T.E. Jones, Key role of chemistry versus bias in electrocatalytic oxygen evolution, *Nature*, **2020**, *587*, 408-413.

[14] J.T. Mefford, A.R. Akbashev, M. Kang, C.L. Bentley, W.E. Gent, H.D. Deng, D.H. Alsem, Y.S. Yu, N.J. Salmon, D.A. Shapiro, P.R. Unwin, W.C. Chueh, Correlative operando microscopy of oxygen evolution electrocatalysts, *Nature*, **2021**, *593*, 67-73.

[15] J. Song, C. Wei, Z.F. Huang, C. Liu, L. Zeng, X. Wang, Z.J. Xu, A review on fundamentals for designing oxygen evolution electrocatalysts, *Chem. Soc. Rev.*, **2020**, *49*, 2196-2214.

[16] J. Bao, X. Zhang, B. Fan, J. Zhang, M. Zhou, W. Yang, X. Hu, H. Wang, B. Pan, Y. Xie, Ultrathin Spinel-Structured Nanosheets Rich in Oxygen Deficiencies for Enhanced Electrocatalytic Water Oxidation, *Angew. Chem. Int. Ed.*, **2015**, *54*, 7399-7404.

[17] J.R. Petrie, V.R. Cooper, J.W. Freeland, T.L. Meyer, Z. Zhang, D.A. Lutterman, H.N. Lee, Enhanced Bifunctional Oxygen Catalysis in Strained $LaNiO_3$ Perovskites, *J. Am. Chem. Soc.*, **2016**, *138*, 2488-2491.

[18] Z. Zhuang, W. Sheng, Y. Yan, Synthesis of monodispere Au@Co_3O_4 core-shell nanocrystals and their enhanced catalytic activity for oxygen evolution reaction, *Adv. Mater.*, **2014**, *26*, 3950-3955.

[19] O. Diaz-Morales, I. Ledezma-Yanez, M.T.M. Koper, F. Calle-Vallejo, Guidelines for the Rational Design of Ni-Based Double Hydroxide Electrocatalysts for the Oxygen Evolution Reaction, *ACS Catal.*, **2015**, *5*, 5380-5387.

[20] A. Grimaud, O. Diaz-Morales, B. Han, W.T. Hong, Y.L. Lee, L. Giordano, K.A. Stoerzinger, M.T.M. Koper, Y. Shao-Horn, Activating lattice oxygen redox reactions in metal oxides to catalyse oxygen evolution, *Nat. Chem.*, **2017**, *9*, 457-465.

[21] A. Grimaud, A. Demortière, M. Saubanère, W. Dachraoui, M. Duchamp, M.-L. Doublet, J.-M. Tarascon, Activation of surface oxygen sites on an iridium-based model catalyst for the oxygen evolution reaction, *Nat. Energy*, **2016**, *2*, 16189.

[22] D.B. Hibbert, C.R. Churchill, Kinetics of the electrochemical evolution of isotopically enriched gases. Part 2.—$^{18}O^{16}O$ evolution on $NiCo_2O_4$ and $Li_xCo_{3-x}O_4$ in alkaline solution, *J. Chem. Soc., Faraday Trans. 1*, **1984**.

[23] Y. Surendranath, M.W. Kanan, D.G. Nocera, Mechanistic Studies of the Oxygen Evolution Reaction by a Cobalt-Phosphate Catalyst at Neutral pH, *J. Am. Chem. Soc.*, **2010**, *132*, 16501-16509.

[24] Y. Sun, H. Liao, J. Wang, B. Chen, S. Sun, S.J.H. Ong, S. Xi, C. Diao, Y. Du, J.-O. Wang, M.B.H. Breese, S. Li, H. Zhang, Z.J. Xu, Covalency competition dominates the water oxidation structure–activity relationship on spinel oxides, *Nat. Catal.*, **2020**, *3*, 554-563.

[25] X. Rong, J. Parolin, A.M. Kolpak, A Fundamental Relationship between Reaction Mechanism and Stability in Metal Oxide Catalysts for Oxygen Evolution, *ACS Catal.*, **2016**, *6*, 1153-1158.

[26] D.S. Bhachu, S.J.A. Moniz, S. Sathasivam, D.O. Scanlon, A. Walsh, S.M. Bawaked, M. Mokhtar, A.Y. Obaid, I.P. Parkin, J. Tang, C.J. Carmalt, Bismuth oxyhalides: synthesis, structure and photoelectrochemical activity, *Chem. Sci.*, **2016**, *7*, 4832-4841.

[27] H. Li, J. Li, Z. Ai, F. Jia, L. Zhang, Oxygen Vacancy-Mediated Photocatalysis of BiOCl: Reactivity, Selectivity, and Perspectives, *Angew. Chem. Int. Ed.*, **2017**, *56*, 2-19.

[28] O. Madelung, Semiconductors: Data Handbook, Third Edition, *Springer Berlin Heidelberg*, **2004**, *p 100*.

[29] D. Kato, K. Hongo, R. Maezono, M. Higashi, H. Kunioku, M. Yabuuchi, H. Suzuki, H. Okajima, C. Zhong, K. Nakano, R. Abe, H. Kageyama, Valence Band Engineering of Layered Bismuth Oxyhalides toward Stable Visible-Light Water Splitting: Madelung Site Potential Analysis, *J. Am. Chem. Soc.*, **2017**, *139*, 18725-18731.

[30] J. Jiang, K. Zhao, X. Xiao, L. Zhang, Synthesis and facet-dependent photoreactivity of BiOCl single-crystalline nanosheets, *J. Am. Chem. Soc.*, **2012**, *134*, 4473-4476.

[31] Z. Ran, X. Wang, Y. Li, D. Yang, X.-G. Zhao, K. Biswas, D.J. Singh, L. Zhang, Bismuth and antimony-based oxyhalides and chalcohalides as potential optoelectronic materials, *Npj Comput. Mater.*, **2018**, *4*, 14.

[32] H. Li, J. Shang, H. Zhu, Z. Yang, Z. Ai, L. Zhang, Oxygen Vacancy Structure Associated Photocatalytic Water Oxidation of BiOCl, *ACS Catal.*, **2016**, *6*, 8276-8285.

[33] Z. Li, Y. Qu, K. Hu, M. Humayun, S. Chen, L. Jing, Improved photoelectrocatalytic activities of BiOCl with high stability for water oxidation and MO degradation by coupling RGO and

modifying phosphate groups to prolong carrier lifetime, *Appl. Catal. B: Environ.*, **2017**, *203*, 355-362.

[34] H. Li, J. Shi, K. Zhao, L. Zhang, Sustainable molecular oxygen activation with oxygen vacancies on the {001} facets of BiOCl nanosheets under solar light, *Nanoscale*, **2014**, *6*, 14168-14173.

[35] L. Zhang, W. Wang, D. Jiang, E. Gao, S. Sun, Photoreduction of CO_2 on BiOCl nanoplates with the assistance of photoinduced oxygen vacancies, *Nano Res.*, **2014**, *8*, 821-831.

[36] J. Li, Y. Yu, L. Zhang, Bismuth oxyhalide nanomaterials: layered structures meet photocatalysis, *Nanoscale*, **2014**, *6*, 8473-8488.

[37] X. Zhang, Z. Ai, F. Jia, L. Zhang, Generalized One-Pot Synthesis, Characterization, and Photocatalytic Activity of Hierarchical BiOX (X = Cl, Br, I) Nanoplate Microspheres, *J. Phys. Chem. C*, **2008**, *112*, 747-753.

[38] J. Li, L. Zhang, Y. Li, Y. Yu, Synthesis and internal electric field dependent photoreactivity of Bi3O4Cl single-crystalline nanosheets with high {001} facet exposure percentages, *Nanoscale*, **2014**, *6*, 167-171.

[39] J. Li, L. Cai, J. Shang, Y. Yu, L. Zhang, Giant Enhancement of Internal Electric Field Boosting Bulk Charge Separation for Photocatalysis, *Adv. Mater.*, **2016**, *28*, 4059-4064.

[40] H. Li, H. Shang, X. Cao, Z. Yang, Z. Ai, L. Zhang, Oxygen Vacancies Mediated Complete Visible Light NO Oxidation via Side-On Bridging Superoxide Radicals, *Environ. Sci. Technol.*, **2018**, *52*, 8659-8665.

[41] Z. Ma, P. Li, L. Ye, Y. Zhou, F. Su, C. Ding, H. Xie, Y. Bai, P.K. Wong, Oxygen vacancies induced exciton dissociation of flexible BiOCl nanosheets for effective photocatalytic CO_2 conversion, *J. Mater. Chem. A*, **2017**, *5*, 24995-25004.

[42] M. Pan, H. Zhang, G. Gao, L. Liu, W. Chen, Facet-dependent catalytic activity of nanosheet-assembled bismuth oxyiodide microspheres in degradation of bisphenol A, *Environ. Sci. Technol.*, **2015**, *49*, 6240-6248.

[43] D.T.T. Trinh, W. Khanitchaidecha, D. Channei, A. Nakaruk, Synthesis, characterization and environmental applications of bismuth vanadate, *Res. Chem. Intermed.*, **2019**, *45*, 5217-5259.

[44] Y. Yuan, Y. Huang, F. Ma, Z. Zhang, X. Wei, G. Zhu, Structural stability, band structure and optical properties of different $BiVO_4$ phases under pressure, *J. Mater. Sci.*, **2016**, *51*, 6662-6673.

[45] S. Tokunaga, H. Kato, A. Kudo, Selective Preparation of Monoclinic and Tetragonal $BiVO_4$ with Scheelite Structure and Their Photocatalytic Properties, *Chem. Mater.*, **2001**, *13*, 4624-4628.

[46] J.D. Bierlein, A.W. Sleight, Ferroelasticity In $BiVO_4$, *Solid State Commun.*, **1975**, *16*, 69-70.

[47] A.W. Sleight, H.Y. Chen, A. Ferretti, Crystal growth and structure of $BiVO_4$, *Mater. Res. Bull.*, **1979**, *14*, 1571-1581.

[48] Z. Zhao, W. Luo, Z. Li, Z. Zou, Density functional theory study of doping effects in monoclinic clinobisvanite $BiVO_4$, *Phys. Lett. A*, **2010**, *374*, 4919-4927.

[49] K. Ding, B. Chen, Z. Fang, Y. Zhang, Density functional theory study on the electronic and optical properties of three crystalline phases of $BiVO_4$, *Theor. Chem. Acc.*, **2013**, *132*, 1352.

[50] A. Kudo, K. Omori, H. Kato, A Novel Aqueous Process for Preparation of Crystal Form-Controlled and Highly Crystalline $BiVO_4$ Powder from Layered Vanadates at Room Temperature and Its Photocatalytic and Photophysical Properties, *J. Am. Chem. Soc.*, **1999**, *121*, 11459-11467.

[51] Z. Zhao, Z. Li, Z. Zou, Electronic structure and optical properties of monoclinic clinobisvanite $BiVO_4$, *Phys. Chem. Chem. Phys.*, **2011**, *13*, 4746-4753.

[52] R. Hoffmann, Solids and Surfaces: A Chemist's View of Bonding in Extended Structures, **1988**.

[53] J.K. Cooper, S. Gul, F.M. Toma, L. Chen, Y.-S. Liu, J. Guo, J.W. Ager, J. Yano, I.D. Sharp, Indirect Bandgap and Optical Properties of Monoclinic Bismuth Vanadate, *J. Phys. Chem. C*, **2015**, *119*, 2969-2974.

[54] J.K. Cooper, S. Gul, F.M. Toma, L. Chen, P.-A. Glans, J. Guo, J.W. Ager, J. Yano, I.D. Sharp, Electronic Structure of Monoclinic $BiVO_4$, *Chem. Mater.*, **2014**, *26*, 5365-5373.

[55] Q. Meng, B. Zhang, L. Fan, H. Liu, M. Valvo, K. Edstrçm, M. Cuartero, R.d. Marco, G.A. Crespo, L. Sun, Efficient $BiVO_4$ Photoanodes by Postsynthetic Treatment: Remarkable Improvements in Photoelectrochemical Performance from Facile Borate Modification, *Angew. Chem. Int. Ed.*, **2021**, *131*, 19203-19209.

[56] B.S. Kalanoor, H. Seo, S.S. Kalanur, Recent developments in photoelectrochemical water-splitting using WO_3/$BiVO_4$ heterojunction photoanode: A review, *Mater. Sci. Energy Technol.*, **2018**, *1*, 49-62.

[57] F.F. Abdi, N. Firet, R. van de Krol, Efficient $BiVO_4$ Thin Film Photoanodes Modified with Cobalt Phosphate Catalyst and W-doping, *ChemCatChem*, **2013**, *5*, 490-496.

[58] Physics of Semiconductor Devices, Third Edition, John Wiley & Sons, Inc., **2007**, p 789.

[59] L.E. Brus, Electron–electron and electron-hole interactions in small semiconductor crystallites: The size dependence of the lowest excited electronic state, *J. Chem. Phys.*, **1984**, *80*, 4403-4409.

[60] B. Enright, D. Fitzmaurice, Spectroscopic Determination of Electron and Hole Effective Masses in a Nanocrystalline Semiconductor Film, *J. Phys. Chem.*, **1996**, *100*, 1027-1035.

[61] N.A. Deskins, M. Dupuis, Intrinsic Hole Migration Rates in TiO_2 from Density Functional Theory, *J. Phys. Chem. C*, **2009**, *113*, 346-358.

[62] J.M. Berakt, M.J. Sienko, Effect of Oxygen-Deficiency on Electrical Transport Properties of Tungsten Trioxide Crystals, *J. Solid State Chem.*, **1970**, *2*, 109-133.

[63] A.J. Rettie, H.C. Lee, L.G. Marshall, J.F. Lin, C. Capan, J. Lindemuth, J.S. McCloy, J. Zhou, A.J. Bard, C.B. Mullins, Combined charge carrier transport and photoelectrochemical characterization of $BiVO_4$ single crystals: intrinsic behavior of a complex metal oxide, *J. Am. Chem. Soc.*, **2013**, *135*, 11389-11396.

[64] F.F. Abdi, T.J. Savenije, M.M. May, B. Dam, R. van de Krol, The Origin of Slow Carrier Transport in $BiVO_4$ Thin Film Photoanodes: A Time-Resolved Microwave Conductivity Study, *J. Phys. Chem. Lett.*, **2013**, *4*, 2752-2757.

[65] K.T. Butler, B.J. Dringoli, L. Zhou, P.M. Rao, A. Walsh, L.V. Titova, Ultrafast carrier dynamics in $BiVO_4$ thin film photoanode material: interplay between free carriers, trapped carriers and low-frequency lattice vibrations, *J. Mater. Chem. A*, **2016**, *4*, 18516-18523.

[66] I. Grigioni, K.G. Stamplecoskie, D.H. Jara, M.V. Dozzi, A. Oriana, G. Cerullo, P.V. Kamat, E. Selli, Wavelength-Dependent Ultrafast Charge Carrier Separation in the $WO_3/BiVO_4$ Coupled System, *ACS Energy Lett.*, **2017**, *2*, 1362-1367.

[67] Y. Lu, Y.-S. Luo, H.-M. Xiao, S.-Y. Fu, Novel core–shell structured $BiVO_4$ hollow spheres with an ultra-high surface area as visible-light-driven catalyst, *CrystEngComm*, **2014**, *16*, 6059-6065.

[68] X. Zhao, W. Luo, J. Feng, M. Li, Z. Li, T. Yu, Z. Zou, Quantitative Analysis and Visualized Evidence for High Charge Separation Efficiency in a Solid-Liquid Bulk Heterojunction, *Adv. Energy Mater.*, **2014**, *4*, 1301785.

[69] R.G. Li, F.X. Zhang, D.E. Wang, J.X. Yang, M.R. Li, J. Zhu, X. Zhou, H.X. Han, C. Li, Spatial separation of photogenerated electrons and holes among {010} and {110} crystal facets of $BiVO_4$, *Nat. Commun.*, **2013**, *4*, 1432.

[70] Y. Pihosh, I. Turkevych, K. Mawatari, J. Uemura, Y. Kazoe, S. Kosar, K. Makita, T. Sugaya, T. Matsui, D. Fujita, M. Tosa, M. Kondo, T. Kitamori, Photocatalytic generation of hydrogen by core-shell $WO_3/BiVO_4$ nanorods with ultimate water splitting efficiency, *Sci. Rep.*, **2015**, *5*, 11141.

[71] S. Gu, W. Li, F. Wang, H. Li, H. Zhou, Substitution of Ce(III,IV) ions for Bi in $BiVO_4$ and its enhanced impact on visible light-driven photocatalytic activities, *Catal. Sci. Technol.*, **2016**, *6*, 1870-1881.

[72] W. Luo, Z. Li, T. Yu, Z. Zou, Effects of Surface Electrochemical Pretreatment on the Photoelectrochemical Performance of Mo-Doped $BiVO_4$, *J. Phys. Chem. C*, **2012**, *116*, 5076-5081.

[73] Z. Zhang, X. Huang, B. Zhang, Y. Bi, High-performance and stable $BiVO_4$ photoanodes for solar water splitting via phosphorus–oxygen bonded FeNi catalysts, *Energy Environ. Sci*, **2022**, *15*, 2867-2873.

[74] K. Sayama, A. Nomura, T. Arai, T. Sugita, R. Abe, M. Yanagida, T. Oi, Y. Iwasaki, Y. Abe, H. Sugihara, Photoelectrochemical Decomposition of Water into H_2 and O_2 on Porous $BiVO_4$ Thin-Film Electrodes under Visible Light and Significant Effect of Ag Ion Treatment, *J. Phys. Chem. B*, **2006**, *110*, 11352-11360.

[75] S.J. Hong, S. Lee, J.S. Jang, J.S. Lee, Heterojunction $BiVO_4/WO_3$ electrodes for enhanced photoactivity of water oxidation, *Energy Environ. Sci*, **2011**, *4*, 1781-1787.

[76] W. Kim, K.-S. Choi, Nanoporous $BiVO_4$ Photoanodes with Dual-Layer Oxygen Evolution Catalysts for Solar Water Splitting, *Science*, **2014**, *343*, 990-994.

[77] J.A. Seabold, K.S. Choi, Efficient and stable photo-oxidation of water by a bismuth vanadate photoanode coupled with an iron oxyhydroxide oxygen evolution catalyst, *J. Am. Chem. Soc.*, **2012**, *134*, 2186-2192.

[78] K. Sayama, N. Wang, Y. Miseki, H. Kusama, N. Onozawa-Komatsuzaki, H. Sugihara, Effect of Carbonate Ions on the Photooxidation of Water over Porous $BiVO_4$ Film Photoelectrode under Visible Light, *Chem. Lett.*, **2010**, *39*, 17-19.

[79] R. Saito, Y. Miseki, K. Sayama, Highly efficient photoelectrochemical water splitting using a thin film photoanode of $BiVO_4/SnO_2/WO_3$ multi-composite in a carbonate electrolyte, *Chem. Commun.*, **2012**, *48*, 3833-3835.

[80] D.K. Zhong, S. Choi, D.R. Gamelin, Near-complete suppression of surface recombination in solar photoelectrolysis by "Co-Pi" catalyst-modified W:$BiVO_4$, *J. Am. Chem. Soc.*, **2011**, *133*, 18370-18377.

[81] W. Luo, J. Wang, X. Zhao, Z. Zhao, Z. Li, Z. Zou, Formation energy and photoelectrochemical properties of $BiVO_4$ after doping at Bi^{3+} or V^{5+} sites with higher valence metal ions, *Phys. Chem. Chem. Phys.*, **2013**, *15*, 1006-1013.

[82] J. Yang, D. Wang, H. Han, C. Li, Roles of Cocatalysts in Photocatalysis and Photoelectrocatalysis, *Acc. Chem. Res.*, **2013**, *46*, 1900-1909.

[83] W.D. Chemelewski, H.C. Lee, J.F. Lin, A.J. Bard, C.B. Mullins, Amorphous FeOOH oxygen evolution reaction catalyst for photoelectrochemical water splitting, *J. Am. Chem. Soc.*, **2014**, *136*, 2843-2850.

[84] C. Ding, J. Shi, D. Wang, Z. Wang, N. Wang, G. Liu, F. Xiong, C. Li, Visible light driven overall water splitting using cocatalyst/$BiVO_4$ photoanode with minimized bias, *Phys. Chem. Chem. Phys.*, **2013**, *15*, 4589-4595.

[85] M. Zhong, T. Hisatomi, Y. Kuang, J. Zhao, M. Liu, A. Iwase, Q. Jia, H. Nishiyama, T. Minegishi, M. Nakabayashi, N. Shibata, R. Niishiro, C. Katayama, H. Shibano, M. Katayama, A. Kudo, T. Yamada, K. Domen, Surface Modification of CoO(x) Loaded $BiVO_4$ Photoanodes with Ultrathin p-Type NiO Layers for Improved Solar Water Oxidation, *J. Am. Chem. Soc.*, **2015**, *137*, 5053-5060.

[86] X.X. Chang, T. Wang, P. Zhang, J.J. Zhang, A. Li, J.L. Gong, Enhanced Surface Reaction Kinetics and Charge Separation of p-n Heterojunction Co_3O_4/$BiVO_4$ Photoanodes, *J. Am. Chem. Soc.*, **2015**, *137*, 8356-8359.

[87] S.K. Choi, W. Choi, H. Park, Solar water oxidation using nickel-borate coupled $BiVO_4$ photoelectrodes, *Phys. Chem. Chem. Phys.*, **2013**, *15*, 6499-6507.

[88] T. Palaniselvam, L. Shi, G. Mettela, D.H. Anjum, R. Li, K.P. Katuri, P.E. Saikaly, P. Wang, Vastly Enhanced $BiVO_4$ Photocatalytic OER Performance by $NiCoO_2$ as Cocatalyst, *Adv. Mater. Interfaces*, **2017**, *4*, 1700540.

3. Experimental section

To avoid repetition, the detailed procedures of sample preparation are presented in Chapter 4 (BiOCl) and Chapter 5 ($BiVO_4$). This chapter mainly gives an introduction to sample characterization and photoelectrochemical measurements, including ultraviolet visible near infrared (UV-Vis-NIR) absorption spectroscopy, X-ray photoelectron spectroscopy (XPS), Electrochemical impedance spectroscopy (EIS) and Intensity modulated photocurrent spectroscopy (IMPS).

3.1 Sample preparation

3.1.1 Chemicals

Bismuth nitrate pentahydrate (Sigma-Aldrich, 99.99%), D-mannitol (Sigma-Aldrich, 98%), NaCl (Sigma-Aldrich, 99%), sodium sulfate(Sigma-Aldrich, 99%), sodium sulfite (Sigma-Aldrich, 98%), 2-methoxyethanol (99.5%, Carl Roth), vanadyl acetylacetonate (Sigma-Aldrich, 98%), acetylacetonate(Sigma-Aldrich, 98%), bis(acetylacetonato) dioxomolybdenum(VI) (Sigma-Aldrich, 99%, monobasic potassium phosphate (Sigma-Aldrich, 99%), dibasic potassium phosphate (Sigma-Aldrich, 98%) were used without further purification, deionized water (conductivity: 0.055 μS cm^{-1}) was provided by Millipore Milli-Q Direct 8 water purification system.

3.1.2 Preparation of BiOCl nanosheets

BiOCl nanosheets were fabricated by a hydrothermal method and the detailed procedure is given in Chapter 4.

3.1.3 Preparation of $BiVO_4$ films

Different from the synthesis of the powder samples, the $BiVO_4$ film photoanodes were prepared by a spin-coating approach. The experimental details are given in Chapter 5.

3.2 Characterization

3.2.1 UV-Vis-NIR spectroscopy

UV-Vis-NIR spectroscopy is employed to measure the light absorption and bandgap of a material. Herein, the basic principle of UV-Vis-NIR spectroscopy is presented. When a film sample is irradiated in the measurement chamber, the following equation is easily obtained according to the law of conservation of photons.

$$I_{tran} + I_{ref} + I_{abs} = I_0 \quad \text{(eqn. 3.1)}$$

I_{tran}, I_{ref}, I_{abs} and I_0 represent the intensities of the transmitted light, reflected light, absorbed light and incident light, respectively.

Therein, I_{tran} follows the Lambert-Beer law.

$$I_{tran} = I_0 \exp(-\alpha\, d) \quad \text{(eqn. 3.2)}$$

D and α are the thickness and the absorption coefficient of the sample.

However, in real solid samples, the rough surface of the samples leads to diffuse reflection. Therefore, I_{tran} is written as:

$$I_{tran} = (I_0 - I_{ref}) \exp(-\alpha\, d) \quad \text{(eqn. 3.3)}$$

The absorption coefficient α can be derived from eqn.3.4.

$$\alpha = \ln\left(\frac{I_0 - I_{ref}}{I_{tran}}\right) \frac{1}{\mathrm{d}} \quad \text{(eqn. 3.4)}$$

Figure 3.1 presents an illustration of the used UV-Vis-NIR Cary 7000 universal spectrometer (Agilent Technologies, Santa Clara, USA). The detector moves to a specific position along the circular path, when the sample is rotated by an angle φ. After that, the spectra are recorded. Since the sample is tilted at an angle φ, the absorption coefficient α should be modified by cosφ and expressed as follows:

$$\alpha = \ln\left(\frac{I_0 - I_{ref}}{I_{tran}}\right) \frac{\cos\varphi}{\mathrm{d}} \quad \text{(eqn. 3.5)}$$

The Tauc plots can be obtained by plotting the curve of absorption coefficient α vs. photon energy to determine the direct or indirect optical bandgap of the semiconductor, which we have discussed in Chapter 2.1.

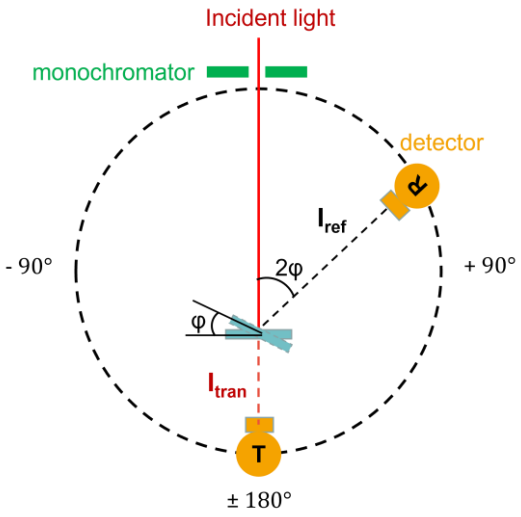

Figure 3.1 Schematic representation of the light path in UV-Vis-NIR spectroscopy.[1]

3.2.2 X-ray photoelectron spectroscopy

Since Hertz and Röntgen separately discovered the photoelectric effect and X-rays in 1887 and 1895, many scientists have contributed to the development of XPS. For example, Albert Einstein explained the photoelectric effect theoretically in 1905, P.D. Innes recorded the first XPS spectrum experimentally. After several important improvements to XPS instruments, Siegbahn and his co-workers finally designed and produced the first commercial XPS equipment in 1969.

Since its invention, XPS has been extensively used in the fields of surface chemistry and materials science. This technique became extremely sensitive and indispensable for material characterization with the development of materials science.

The XPS principle is based on the photoelectric effect. The production of photoelectrons involves two steps. Firstly, high-energy electron beams bombard anodic target materials (aluminum), accompanied with producing X-rays (for Al Ka, $E_{X\text{-}ray}$=1486.6 eV); Secondly, photoelectrons are excited from the core levels and valence levels of the samples by X-ray

illumination. Photoelectrons with sufficient kinetic energy escape from the surface and are collected by an electron energy analyzer.

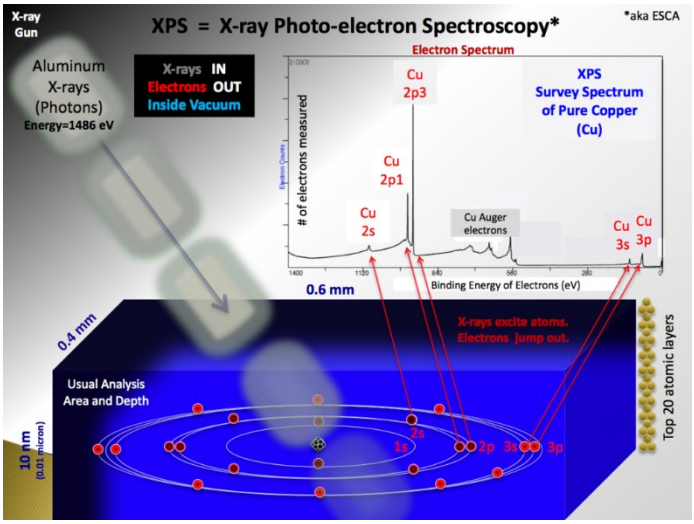

Figure 3.2 Schematic diagram of XPS.[2]

As mentioned above, X-ray photoemission spectroscopy is a key technique for understanding the chemical composition and electronic structure of materials. Here, we present some primary applications of XP spectra.

(1) Identification of specific elements.

According to the photoelectric effect, the binding energy of the material can be expressed as follows:

$$E_{binding} = \mathrm{h}\upsilon - E_{kinetic} - \Phi \quad \text{(eqn. 3.6)}$$

E_{binding} and E_{kinetic} are the binding energies and kinetic energies of the photoelectrons, respectively. $h\upsilon$ is the X-ray energy (here: 1486.6 eV), ϕ is the work function of the spectrometer. The binding energy is unique when the kinetic energy of the photoelectrons in a particular atomic orbital is determined.

The first basic application of XPS is to identify the type of elements in the sample. The core level of an element usually has a higher binding energy than its outer levels. It is also worth noting that the spin-orbit splitting energy of the element is also a characteristic of the element identification. The spin-orbit splitting interaction is a magnetic interaction between the

angular momentum of an atomic orbital (*s, p, d, f* orbitals) and the spin angular momentum of an electron. Because the spin state of the electron is up (*s* = 1/2) or down (*s* = -1/2), each electron in a given orbital has two different states. The total angular momentum is the sum of the orbital angular momentum and the spin angular momentum of the electron, written as follows:

$$J = l + \mathrm{s} \quad \text{(eqn. 3.7)}$$

J is the total angular momentum, *l* is the orbital momentum (*l* = 0, 1, 2, 3, corresponding to the s, p, d, f orbitals), s is the spin angular momentum of the electron, respectively.

For example, owning to the spin-orbital coupling of the electron, the 2*p* orbital (*l* = 2) is split into a doublet: $2p_{1/2}$ and $2p_{3/2}$. The energy difference between these two sub-levels is called the spin orbital splitting energy of the 2*p* orbital. Moreover, the degeneracy degree of each splitting energy level is equal to 2*J* +1. Therefore, the peak area ratio of $2p_{1/2}$ and $2p_{3/2}$ is theoretically 1 to 2. Here we summarize this information about spin orbital splitting in **Table 3.1**.

Table 3.1 Summary of spin orbital splitting and XPS notations.

Orbit	Orbital angular momentum (*l*)	Total angular momentum ($J = l \pm s$)	Degeneracy degree ($2J + 1$)	XPS notation	Peak area ratio
s	0	1/2	-	$s_{1/2}$	-
p	1	1/2, 3/2	2, 4	$p_{1/2}$, $p_{3/2}$	1:2
d	2	3/2, 5/2	4, 6	$d_{3/2}$, $d_{5/2}$	2:3
f	3	5/2, 7/2	6, 8	$f_{5/2}$, $f_{7/2}$	3:4

XPS can identify not only the type of the elements but also their valence states. Generally, low valence states imply low binding energies, such as $E_{binding}$ (Bi^0) < $E_{binding}$ (Bi^{3+}). Based on this, the atomic ratio of various valence states can be readily determined from the XPS peak area

and R.S.F value of the element. For instance, Mofarah et al. reported that Ce^{3+} in ultrathin CeO_{2-x} films reached up to 60 at% according to the area ratio of Ce^{3+} and Ce^{4+} peaks.[3] Yannick et al. Found that Bi^{3+} and V^{5+} in $BiVO_4$ can be partially reduced to Bi^0 and V^{4+} during the water exposure measurement.[4]

The second useful information from XPS analysis is the Auger electron spectra. Excitation of the atomic inner electrons leaves many electron vacancies. The outer electrons of the atoms can jump to an inner low energy empty orbital and simultaneously releasing thermal or photon energy in the process. This photon energy can be used to excite surrounding electrons, and these re-generated free electrons are called Auger electrons. Auger electron spectroscopy is a powerful and practical characterization technique.

The third key characterization in XPS is the valence band spectra. UPS is more surface sensitive than XPS due to the lower excitation light source (21.2 eV or 40.1 eV), but valence band spectra of XPS are also conventionally used to determine the work function and valence band position determination of semiconductors. Once the band position of the semiconductor and the required redox potentials of the chemical reactions are known, it is possible to assess whether the chemical reactions thermodynamically occur. The band diagram of the semiconductor can be tuned by some modification approaches, such as doping and defect engineering etc. Hence, an energy band diagram is also beneficial for an in-depth understanding to analyze the charge transfer and reaction mechanism.

3.3 Photoelectrochemical measurements

3.3.1 Electrochemical Impedance Spectroscopy (EIS)

Electrochemical impedance spectroscopy is a versatile tool to investigate charge kinetics and ion adsorption processes at the electrode.[5, 6] According to Ohm's theorem, the resistance R is defined as the applied voltage *U* divided by the electric current (*I*), when a certain direct current (DC) voltage is applied to a material.

$$R = \frac{\mathrm{U}}{I} \quad \text{(eqn.3.8)}$$

This is the simplest expression of ideal resistance. However, many electrical circuits are much more complex due to the presence of inductance and capacitance. In this case, resistance is replaced by impedance *Z*. Generally, an alternating current (AC) potential is used to characterize these electrical elements in complex electrical circuits. The AC potential is expressed as follows:

$$U(t) = U_A sin(\omega t) \quad \text{(eqn.3.9)}$$

U_A is the maximum amplitude of the frequency dependent voltage $U(t)$. ω is the angular frequency. The resulting current is relevant to the elements. For an ideal resistor, the AC current behave no phase shifts and the impedance Z can be written as:

$$Z = \frac{U_A sin(\omega t)}{I_A sin(\omega t)} = \frac{U_A}{I_A} \quad \text{(eqn. 3.10)}$$

For capacitance, the resulting current shows a phase shift with a maximum amplitude of I_A. The impedance Z is described as follows:

$$Z = \frac{U_A sin(\omega t)}{I_A sin(\omega t - \phi)} = |Z| \frac{sin(\omega t)}{sin(\omega t - \phi)} \quad \text{(eqn. 3.11)}$$

where |Z| is the absolute value of the impedance Z.

Besides, according to Euler's formula, the complex number Ã can be represented in three ways, as illustrated in **Figure 3.3**.

$$\tilde{A} = a + b\,i = r\,cos\phi + i\,r\,sin\phi = r\,e^{i\,\phi} \quad \text{(eqn. 3.12)}$$

$$i^2 = -1 \quad \text{(eqn. 3.13)}$$

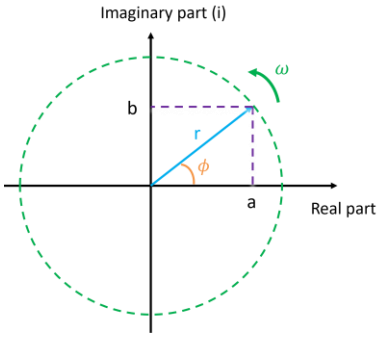

Figure 3.3 Three representations of complex number.

Therefore, the U(t) and I(t) can be represented by the following equations, respectively.

$$\mathrm{U}(t) = U_A \, \mathrm{e}^{i\,\omega t} \quad \text{(eqn. 3.14)}$$

$$\mathrm{I}(t) = I_A \, \mathrm{e}^{i\,(\omega t - \phi)} \quad \text{(eqn. 3.15)}$$

As a result, the impedance Z is written as:

$$Z = \frac{\mathrm{U(t)}}{I(t)} = |Z|\mathrm{e}^{i\,\phi} = |Z|\big(\cos(\phi) + i sin(\phi)\big) = Z_{real} + i\,Z_{im} \quad \text{(eqn. 3.16)}$$

Z_{real} and Z_{im} are the real and imaginary parts of the impedance Z, respectively.

Photoelectrochemical water oxidation usually takes place at the surface of the photocathode.[7, 8] This electrochemical half-cell can be considered as an equivalent electrical circuit consisting of resistance, inductance, and capacitance. Taking $BiVO_4$ work (Chapter 5) as an example, a semiconductor electrolyte interface typically consists of a double electrical layer and a space charge region, as shown in **Figure 3.4**. Accordingly, the total capacitance (C_{total}) is the sum of the double layer capacitance (C_{dl}) and the space charge region capacitance (C_{SCR}) while the total resistance (R_{total}) is the sum of the charge transfer resistance (R_{ct}) and the bulk resistance (R_{bulk}). R_s is the solution resistance between the working and reference electrodes. For simplicity, this equivalent circuit of a semiconductor liquid junction can be further represented by the Randles circuit (**Figure 3.5**).[9]

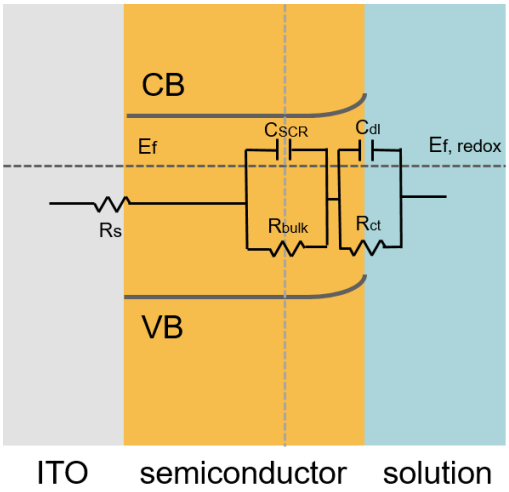

Figure 3.4 Illustration of a semiconductor-electrolyte interface and the corresponding equivalent electrical circuits.

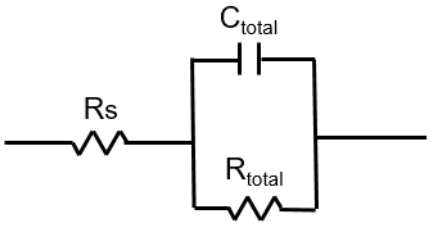

Figure 3.5 Schematic of a Randles circuit model.

The frequency dependent electrochemical impedance spectra can be plotted by two common ways: Nyquist and Bode plots. The Nyquist plot is the curve of the imaginary part versus the real part as the angular frequency is increased. **Table 3.2** summarizes the resulting impedance Z of each electrical element.

Table 3.2 Electrical elements, R, L and C indicate resistance, inductance, and capacitance, respectively.

Element	Relationship between current (*I*) vs. voltage (*U*)	Impedance *Z*
resistor	$U = IR$	$U = R$
inductor	$U = L\frac{dI}{dt}$	$Z = i\omega L$
capacitor	$I = C\frac{dU}{dt}$	$Z = \frac{1}{i\omega C}$

According to this data, the total impedance of the Randles circuit can be readily written as:

$$Z = R_s + \frac{1}{\frac{1}{R_{total}} + i\omega C} = R_s + \frac{R_{total}}{1 + i\omega C\, R_{total}} \quad \text{(eqn. 3.17)}$$

The impedance *Z* is equal to R_s when the angular frequency ω approaches infinity. Conversely, the impedance *Z* is equal to the sum of R_s and R_{total} when ω approaches zero. When the $\omega C\, R_{total} = 1$, the impedance *Z* can be expressed as:

$$Z = R_s + \frac{1}{\frac{1}{R_{total}} + i\omega C} = R_s + \frac{R_{total}}{1+i} = (R_s + \frac{R_{total}}{2}) + i\,\frac{R_{total}}{2} \quad \text{(eqn. 3.18)}$$

These three cases of a Randles circuit model are displayed in **Figure 3.6a**.

The Bode plot is the curve of log $|Z|$ and phase (ϕ) versus log ω. The typical Bode plot of a Randles circuit model is shown in **Figure 3.6b**.

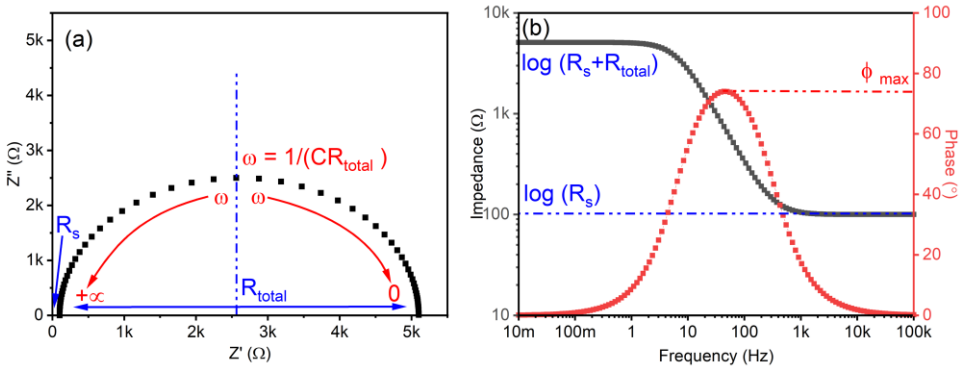

Figure 3.6 Nyquist plot (a) and Bode plot (b) of a Randles circuit, produced by the model editor of Zahner Analysis.

3.3.2 Intensity modulated Photocurrent Spectroscopy (IMPS)

IMPS provides a direct approach to monitor the charge carrier dynamic behavior of photoelectrodes on different time scales.[10] Different from small perturbation of voltage in EIS, IMPS is stimulated by the tiny perturbation of incident light intensity modulated with frequency variation. The perturbation amplitude and the frequency range of the light intensity are usually set to 10% and 0.1 Hz to 10 kHz, respectively. The resulting photocurrent variation generally reflects the transfer and recombination behaviors of photogenerated charge carriers at the interface.[11, 12]

To better understand the IMPS, the external quantum efficiency (EQE) is introduced. EQE is defined as the quotient of the resulting photocurrent density (J_e) and the theoretical maximum photocurrent density (J_ϕ) when an incident photon flux of wavelength λ illuminates the photovoltaic devices. Its expression is given by:

$$EQE = \frac{J_e(\lambda)}{J_\phi(\lambda)} \quad \text{(eqn. 3.19)}$$

Integrating the EQE over the specific wavelength range of the incident photon flux gives the corresponding total photocurrent density.

Similarly, the IMPS transfer function is the ratio of the collected photocurrent density ($\widetilde{J_e}$) to the theoretical maximum photocurrent density ($\widetilde{J_\phi}$) when a frequency-modulated incident photon flux stimulates the photovoltaic devices (wavelength λ is fixed). The IMPS transfer function can be expressed as:

$$H(\omega) = \frac{\widetilde{J_e}(\omega)}{\widetilde{J_\phi}(\omega)} \quad \text{(eqn. 3.20)}$$

Where *H(ω)* is the IMPS transfer function, *ω* is the frequency of the incident light.

When ω approaches zero, the incident light is stationary. In this case, the transfer function *H*(*ω*) can be rewritten as:

$$H(0) = \frac{\widetilde{J_e}(0)}{\widetilde{J_\phi}(0)} = \frac{\overline{J_e}}{\overline{J_\phi}} = EQE \quad \text{(eqn. 3.21)}$$

To explain the IMPS response of a semiconductor electrolyte junction, a reasonable interface model was proposed by Ponomarev and Peter in 1995.[13] This model reveals the competition between the interfacial transfer and recombination of the photoexcited minority carriers. The photocurrent response can be written as the following equation.

$$j(\omega) = \frac{I_0[k_{tr}+i\omega(C_{cell}/C_{sc})]}{(k_{tr}+k_{rec}+i\omega)(1+i\omega\tau)} \quad \text{(eqn. 3.22)}$$

ω is the angular frequency of the incident modulated light, I_0 is the intensity of photo-generated hole flux towards the surface. C_{cell} is the capacitance of the electrochemical cell and is equal to $\frac{C_{sc}C_H}{C_{sc}+C_H}$. C_{sc} and C_H are the capacitances of the space charge layer and Helmholtz layer. k_{tr} and k_{rec} are the transfer rate constant and recombination rate constant of photogenerated minority charge carriers, respectively. τ is the time constant of the electrochemical cell.[13, 14]

Since the implications of this formula have been elaborated in Chapter 5, it will not be repeated here.

References

[1] D.C. Moritz, Fermi level limitations in copper oxides for solar cell applications, *Master Thesis, TU Darmstadt*, **2019**, P 19.

[2] Schematic diagram of X-ray photo-electron spectroscopy, http://en.wikipedia.org/wiki/X-ray_photoelectron_spectroscopy.

[3] S.M. S, E. Adabifiroozjaei, Y. Yao, P. Koshy, S. Lim, R. Webster, X. Liu, R. Khayyam Nekouei, C. Cazorla, Z. Liu, Y. Wang, N. Lambropoulos, C.C. Sorrell, Proton-assisted creation of controllable volumetric oxygen vacancies in ultrathin CeO_{2-x} for pseudocapacitive energy storage applications, *Nat. Commun.*, **2019**, *10*, 2594.

[4] Y. Hermans, S. Murcia-López, A. Klein, W. Jaegermann, $BiVO_4$ Surface Reduction upon Water Exposure, *ACS Energy Lett.*, **2019**, *4*, 2522-2528.

[5] H.S. Magar, R.Y.A. Hassan, A. Mulchandani, Electrochemical Impedance Spectroscopy (EIS): Principles, Construction, and Biosensing Applications, *Sensors*, **2021**, *21*, 6578.

[6] N.A. Cañas, K. Hirose, B. Pascucci, N. Wagner, K.A. Friedrich, R. Hiesgen, Investigations of lithium–sulfur batteries using electrochemical impedance spectroscopy, *Electrochim. Acta*, **2013**, *97*, 42-51.

[7] W.D. Chemelewski, H.C. Lee, J.F. Lin, A.J. Bard, C.B. Mullins, Amorphous FeOOH oxygen evolution reaction catalyst for photoelectrochemical water splitting, *J. Am. Chem. Soc.*, **2014**, *136*, 2843-2850.

[8] D.K. Zhong, S. Choi, D.R. Gamelin, Near-complete suppression of surface recombination in solar photoelectrolysis by "Co-Pi" catalyst-modified W:$BiVO_4$, *J. Am. Chem. Soc.*, **2011**, *133*, 18370-18377.

[9] X. Wu, F.E. Oropeza, Z. Qi, M. Einert, C. Tian, C. Maheu, K. Lv, J.P. Hofmann, Influence of Mo doping on interfacial charge carrier dynamics in photoelectrochemical water oxidation on $BiVO_4$, *Sustain. Energy Fuels*, **2023**, *7*, 2923-2933.

[10] S. Ravishankar, A. Riquelme, S.K. Sarkar, M. Garcia-Batlle, G. Garcia-Belmonte, J. Bisquert, Intensity-Modulated Photocurrent Spectroscopy and Its Application to Perovskite Solar Cells, *J. Phys. Chem. C*, **2019**, *123*, 24995-25014.

[11] L.M. Peter, Dynamic Aspects of Semiconductor Photoelectrochemistry, *Chem. Rev.*, **1990**, *90*, 753-769.

[12] L. Dloczik, O. Ileperuma, I. Lauermann, L.M. Peter, E.A. Ponomarev, G. Redmond, N.J. Shaw, I. Uhlendorf, Dynamic response of dye sensitized nanocrystalline solar cells characterization by intensity, *J. Phys. Chem. B*, **1997**, *101*, 10281-10289.

[13] E.A. Ponomarev, L.M. Peter, A generalized theory of intensity modulated photocurrent spectroscopy (IMPS), *J. Electroanal. Chem.*, **1995**, *396*, 219-226.

[14] M. Antuch, P. Millet, A. Iwase, A. Kudo, The role of surface states during photocurrent switching: Intensity modulated photocurrent spectroscopy analysis of $BiVO_4$ photoelectrodes, *Appl. Catal. B: Environ.*, **2018**, *237*, 401-408.

4. Thermally Induced Oxygen Vacancies in BiOCl Nanosheets and Their Impact on Photoelectrochemical Performance[1]

Oxygen vacancies (OVs) have been reported to significantly alter the photocatalytic properties of BiOCl nanosheets. However, their formation mechanism and their role in the enhancement of photoelectrochemical performance remain unclear. In this work, thermally induced oxygen vacancies are introduced in BiOCl nanosheets by annealing in He atmosphere at various temperatures and their formation mechanism is investigated by in-situ diffuse reflectance infrared (DRIFTS) measurements. The influence of OVs on band offset, carrier concentrations and photoelectrochemical performance are systematically studied. The results show that (1) the surface of BiOCl nanosheets is extremely sensitive to temperature and defects are formed at temperatures as low as 200 °C in inert atmosphere. (2) The formation of surface and bulk OVs in BiOCl is identified by a combination of XPS, in-situ DRIFTS, and EPR experiments. (3) The photocurrent of BiOCl is limited by the concentration of charge carriers and shallow defect states induced by bulk oxygen vacancies, while the modulation of these parameters can effectively increase light absorption and carrier concentration leading to an enhancement of photoelectrochemical performance of BiOCl.

4.1 Introduction

Bismuth oxychloride (BiOCl), a promising V-VI-VII layered ternary semiconductor, has been widely studied in environmental and energy conversion applications.[1, 2] It is a layered structure with $[Bi_2O_2]^{2+}$ slabs interleaved by a double layer of Cl^- ions. Compared to other metal-oxide semiconductors, this unique layered structure produces a built-in electric field and facilitates the separation of photo-generated charge carriers.[3, 4] However, the large

[1] This chapter has been published in: **Xiaofeng Wu**, Freddy E. Oropeza, Daan den Boer, Peter Kleinschmidt, Thomas Hannappel, Dennis G. H. Hetterscheid, Emiel J. M. Hensen, Jan Philipp Hofmann, Thermally induced oxygen vacancies in BiOCl nanosheets and their impact on photoelectrochemical performance, *ChemPhotoChem*, **2022**, e202200192.

bandgap (3.4 eV) in the UV range and low quantum efficiency of bulk BiOCl photocatalysts have seriously hampered their photocatalytic application.[5, 6]

Up to now, several strategies have been proposed to solve the above-mentioned issues, including non-metal doping, preparation of homojunction and heterojunction composites,[7, 8] or metal co-catalyst deposition.[9] Among those strategies, introduction of defects is a simple and efficient way to improve the photocatalytic performance of BiOCl.[5, 10] According to the differences in atomic structure, defects can be categorized as point defect, line defects, planar defects and volume defects. The relation between these defects and photocatalytic activity may be complex and elusive. For instance, oxygen vacancies (OVs) in metal oxide semiconductors, considered point defects, can sensitively influence photoelectrochemical properties.[11-13] Recently, the study of surface OVs has emerged as a hot research topic, because most catalytic reactions occur on the surface of catalytic materials and a deep understanding of the nature of surface OVs is needed to design and prepare highly efficient photocatalysts. For example, Li et al. reported that surface OVs in BiOCl can improve water adsorption and reduce activation energy barriers for photocatalytic water oxidation.[14] Zhao et al. discovered that different pathways of molecular oxygen activation are prevailing on (001) and (010) crystal planes of BiOCl nanosheets in the presence of surface OVs.[15]

At the same time, the bulk properties of the semiconductor are equally important in determining the efficiency of a photoelectrochemical reaction. Separation and migration of photo-generated charge carriers first occur in the bulk of the materials. In addition, bulk modification, such as doping and defects, remarkably affect light harvesting ability and band alignment.[16-18] Nonetheless, bulk defects are commonly regarded as recombination centers for charge carriers, and therefore, unfavorable for photoelectrochemical performance.[19, 20] Taking these studies into account, it appears that experimental relationships between the presence of bulk OV defects, shallow or deep defect states in the band gap and the photoelectrochemical performance of OV-rich BiOCl still need to be established.

In this work, BiOCl samples were prepared by a hydrothermal method and OVs were introduced by thermal annealing at different temperatures in inert gas atmosphere. The formation process of OVs is investigated by in-situ diffuse reflectance FT-IR spectroscopy

(DRIFTS) experiments. X-ray photoelectron spectra (XPS) show the absence of surface OVs in as-prepared BiOCl samples, while electron paramagnetic resonance (EPR) confirms the presence of (bulk) OVs. The influence of oxygen vacancies on light absorption, carrier concentration and photoelectrochemical response are further investigated and discussed.

4.2 Experimental Details

4.2.1 Sample preparation

4.2.1.1 Preparation of BiOCl nanosheets

BiOCl nanosheets are synthesized by a hydrothermal method according to reference.[21] Briefly, 2 mmol of $Bi(NO_3)_3 \cdot 5H_2O$ (Aldrich, 99.99%) were dissolved in 50 mL of an aqueous D-mannitol (Aldrich, 98%) solution (0.1 mol L^{-1}) followed by 1 hour of agitation. After that, 10 mL of saturated aqueous NaCl (Aldrich, 99%) solution was added dropwise to the above solution under stirring. Subsequently, this mixture was transferred to a 100 mL Teflon-lined autoclave and heated at 160 °C for 3 h. The precipitates were washed with water and ethanol for 7-8 times and then collected after drying at 60 °C for overnight. For simplicity, the as-prepared, pristine sample is denoted as BOC-S0.

4.2.1.2 Thermal treatment of BiOCl nanosheets

The introduction of oxygen vacancies of BiOCl is conducted at various temperatures in helium atmosphere, the gas flow rate and ramping rate are 50 ml min^{-1} and 5 °C min^{-1}, respectively. The annealing samples are denoted as BOC-H-x (x indicates annealing temperature in °C). In addition, for comparison, BiOCl annealed at 300 °C in oxygen for 12 h is denoted as BOC-O-300.

4.2.2 Materials characterization

Powder X-ray diffraction pattern were recorded on a Bruker D2 PHASER diffractometer using Cu Kα radiation at a scan rate of 0.02° min^{-1}. BET specific surface area and pore volume were measured on a Tristar 3000 automated gas adsorption system. Transmission electron microscopy (FEI Tecnai 20) was used to observe the morphology and bulk structure of the materials. UV-vis diffuse reflection spectra of BiOCl samples were obtained on a UV-Vis

spectrometer (Shimadzu UV-2401, Japan) with $BaSO_4$ as reference. X-ray photoelectron spectra were collected on a Thermo Scientific K-Alpha spectrometer equipped with a monochromic Al K_α X-ray source (hv = 1486.7 eV). The powder samples were mounted on adhesive double-sided conductive carbon tape on substrate or filled into the holes of a homemade Cu powder sample holder. A low energy electron/ion flood gun neutralizer was used to compensate the surface charging. High resolution spectra of Bi, O and Cl elements were averagely scanned for 30 times and their pass energy was set to 50 eV. Spectra were binding energy calibrated by setting the main line of Bi $4f_{7/2}$ spectrum to 159.4 eV. All XPS spectra were analyzed and processed by CasaXPS and Origin softwares. EPR spectra were measured on a Bruker EMXplus X-band spectrometer at room temperature in air at a frequency of 9.460-9.470 GHz in 4 mm thin wall quartz glass EPR tubes (Wilmad).

In-situ temperature-controlled diffuse reflectance infrared Fourier transform spectroscopy (DRIFTS) was used to assess surface oxygen vacancy formation. Steady state IR spectra were recorded in the region of 400 to 3950 cm^{-1} at a resolution of 2 cm^{-1} on a Bruker Vertex 70v spectrometer with a room temperature DTGS detector. Pristine BOC-S0 was used as starting sample and heated at 200 °C, 250 °C, and 300 °C in vacuum, respectively. For the oxidation process, dry O_2 (≥99.95%) was introduced into the cell at a flow rate of 2 $cm^3\ min^{-1}$ at 400 °C for 6 h to oxidize defective BiOCl while the static pressure of the cell was 10 mbar. After cooling down to 298 K, DRIFTS spectra were collected in static vacuum (1 mbar). Dry KBr powder was used as the reference.

Photoelectrochemical measurements were carried out in three-electrode configuration (CIMPS workstation, Zahner-Elektrik GmbH & Co. KG, Germany). 0.1 M sodium phosphate buffer solution containing 0.1 M sodium sulfite was used as electrolyte for photocurrent and electrochemical impedance spectroscopy (EIS) measurements. The circular irradiation area was 0.283 cm^2 and the intensity of simulated solar LED white light source was 100 mW cm^{-2}. EIS measurements were conducted in the frequency range between 0.1 Hz and 10 KHz with a perturbation amplitude of 10 mV at open circuit potential (OCP). Mott-Schottky plots were measured at a frequency of 500 Hz in 0.5 M Na_2SO_4 solution in three-electrode configuration. Ag/AgCl (3 M NaCl) and Pt wire were used reference and counter electrodes, respectively and the potential of the Ag/AgCl reference electrode was +0.251 V.

Working electrodes were prepared on FTO glass (Solaronix, TCO10-10, 10 ohm/sq.) by drop casting. In detail, for pre-treatment, all BiOCl samples were sieved with an 80 µm sieve plate and the smaller particles were kept for further preparation of working electrodes. FTO glass substrates were initially subsequently ultra-sonicated in distilled water, ethanol and acetone for 30 minutes each, followed by UV-ozone cleaning treatment for 20 minutes. After that, 100 mg of the above samples were dispersed in a mixed solution of 5 w/w% Nafion^{TM} solution (200 µL) and ethanol (2 mL). Then, the solution was ultra-sonicated for 30 minutes to obtain a uniform white slurry. 100 µL of slurry was carefully dropped and spread out on the FTO substrates (2x2 cm^2). Thin films are formed after natural evaporation of ethanol.

4.3 Results and Discussion

4.3.1 Effect of annealing treatment on crystal structure, morphology, and specific surface area

The XRD pattern of BiOCl samples are shown in **Figure 4.1**. X-ray diffraction peaks of all BiOCl samples are in accordance with tetragonal phase BiOCl (JCPDS card no. 06-0249). When increasing temperature to 300 °C in helium or oxygen, all BiOCl samples retain their original tetragonal crystal structure, with no obvious diffraction peaks of Bi metal are observed. This indicates that annealing in either O_2 or He atmospheres did not significantly change the crystal structure of BiOCl samples. In addition, the annealing process has little effect on the average crystallite sizes of BiOCl samples as estimated via the Scherrer formula (**Table 4.1**). However, intensities of the diffraction peaks of BiOCl nanosheets obviously have changed. Using the intensity of the (001) crystal plane as reference, relative crystallinity of BiOCl noticeably increased from 1.00 to 1.68 after annealing in oxygen while it decreased from 1.00 to 0.58, 0.65, 0.55 at 200°C, 250°C, 300°C in helium, respectively (**Table 4.1**). Intensity of the (020) crystal facet follows the same trend. These changes are possibly caused by the increasing number of defects during annealing in He.

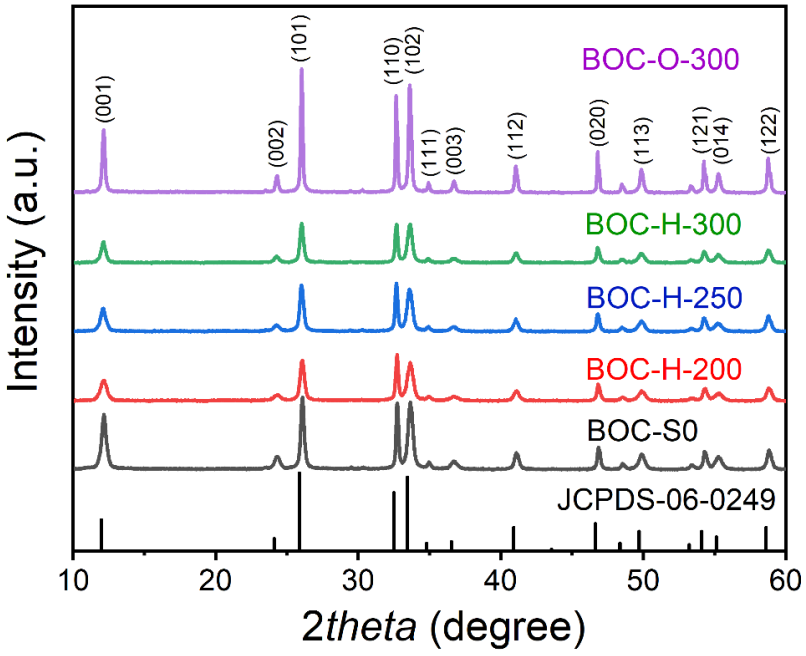

Figure 4.1 X-Ray diffraction pattern of as-prepared BOC-S0 (dark grey), BOC-H-200 (red), BOC-H-250(blue), BOC-H-300 (green) and BOC-O-300(purple), with BiOCl JCPDS-06-0249 (black) as reference.[22]

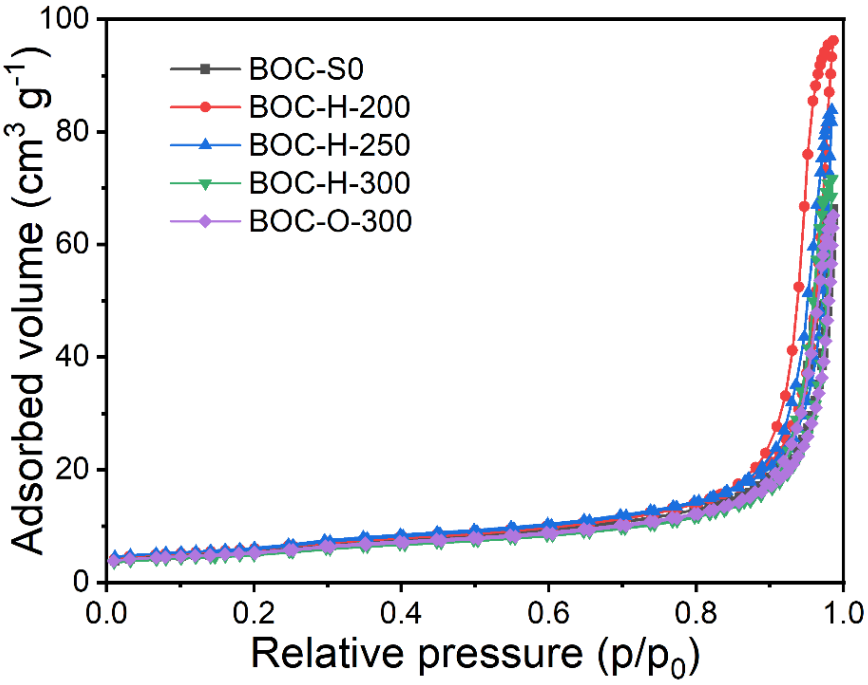

Figure 4.2 N_2 physisorption isotherms of as-prepared BiOCl samples.[22]

Table 4.1 Physical properties of the as-synthesized BiOCl samples, including BET surface area, pore volume, relative crystallinity and average crystallite size.[22]

Sample	S_{BET} area ($m^2\ g^{-1}$)	Pore volume ($cm^3\ g^{-1}$)[a]	Relative crystallinity[b]		Average crystallite size (nm)[c]
			(001)	(020)	
BOC-S0	19.5(±0.03)	0.11(±0.005)	1.00	1.00	23(±1)
BOC-H-200	21.2(±0.05)	0.15(±0.002)	0.58(±0.01)	0.73(±0.01)	17(±1)
BOC-H-250	21.4(±0.02)	0.13(±0.003)	0.65(±0.01)	0.80(±0.01)	20(±1)
BOC-H-300	17.5(±0.01)	0.11(±0.004)	0.55(±0.01)	0.70(±0.01)	23(±1)
BOC-O-300	18.7(±0.04)	0.10(±0.003)	1.68(±0.01)	1.72(±0.01)	39(±1)

[a] pore volume

[b] relative crystallinity calculated from the relative intensity of the (001) and (020) diffraction peaks with BOC-S0 as reference

[c] average crystallite size calculated from Scherrer formula.

Additionally, N_2 physisorption isotherms of the BiOCl samples were collected to calculate specific surface areas and pore volume (**Figure 4.2**). The BET surface area of BOC-S0 is 19.53 m^2g^{-1} and its pore volume is 0.11 $cm^{-2}g^{-1}$. These values show a negligible change after treatment at various temperatures in helium and oxygen. The data of physical properties are summarized in **Table 4.1**.

From TEM images of BOC-S0 and BOC-H-300 (**Figure 4.3**), it can be observed that BOC-S0 shows nanosheet morphology with length and thickness of approximately 100-200 nm and 20-30 nm, respectively. The lattice spacing is 0.730 nm, which implies their exposed (001) crystal facets. After annealing at 300 °C in helium, some defects emerged on the (001) crystal facets (**Figure 4.3c and 4.3d**). Taken together, the above data reflect that annealing in He atmosphere does not significantly change crystal structure, morphology, or porosity of BiOCl nanosheets.

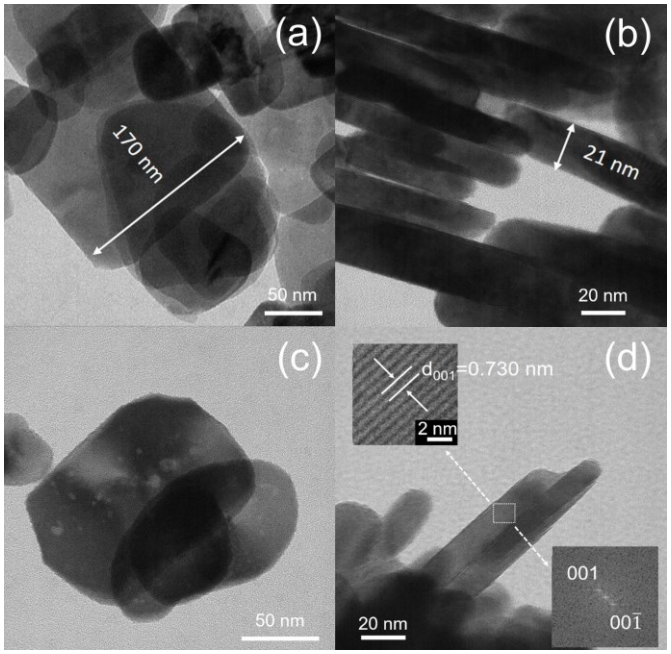

Figure 4.3 Transmission electron microscopy (TEM) images of BOC-S0 ((a) and (b)) and BOC-H-300 ((c) and (d)).[22]

4.3.2 Light absorption and formation of oxygen vacancies

In order to obtain information about the influence of defects on the optical absorption, UV-Vis diffuse reflectance spectra of the BiOCl samples were recorded. As shown in **Figure 4.4**, the absorption edge of BOC-S0 is at about 380 nm and the indirect bandgap calculated from corresponding the Tauc plot is 3.24 eV. The apparent bandgaps for the samples BOC-H-X (200, 250, 300) are 3.16, 3.00, and 2.95 eV, respectively, and decrease with increasing annealing temperature. The reduced bandgap is caused by band tailing due to the presence of a high number of defect states.[23] Interestingly, the bandgap of sample BiOCl-O-300 is restored to the value of the sample BOC-S0, indicating the healing of OV defects by O_2 annealing treatment. UV-Vis spectra of BOC-H-X (200, 250, 300) show a large increase of light absorption in the visible light range, while BOC-O-300 shows no changes. This extended light absorption at longer wavelengths has been reported to originate from oxygen vacancies.[24, 25] EPR spectra were measured to verify the presence of OVs (**Figure 4.5**). A significant peak appears positioned at g = 2.004, which is the typical signature for trapped electrons in OVs.[10] With an increasing annealing temperature in helium atmosphere, the respective signal gradually becomes larger, indicating an increasing amount of OVs. Consistently, BOC-O-300 shows no

response in the EPR spectra which relates to the absence of OVs after annealing in oxygen. In comparison to other reducible oxides, BiOCl is much more sensitive and prone to form OVs at low temperature. For instance, TiO_2 starts to be reduced at 500°C during H_2-TPR measurements.[26] Surface and bulk oxygen of pristine CeO_2 can be removed under H_2 gas atmosphere at 470 °C and 730 °C, respectively.[27] BiOCl is much less stable and phase change occurs at above 400°C.[28] The readiness to form OVs relates to the low Bi-O bond enthalpy.[2]

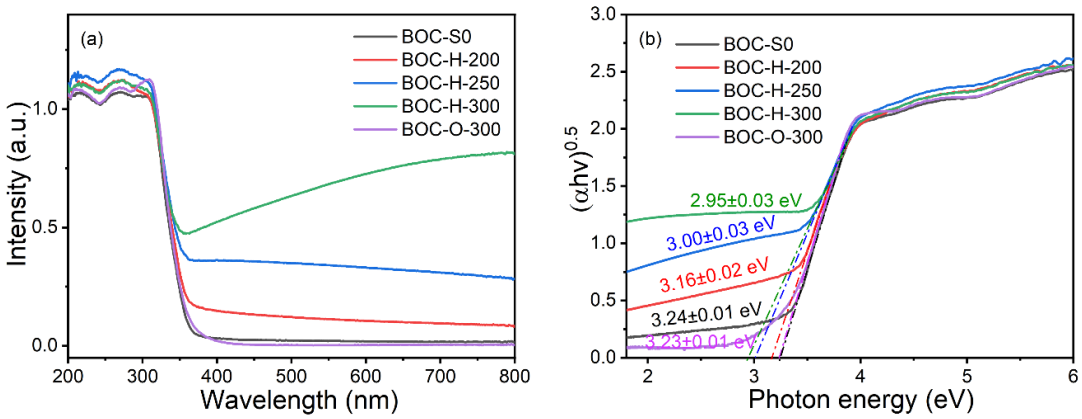

Figure 4.4 UV-Vis diffuse reflectance spectra (a) and the corresponding Tauc plots (b) of as-prepared and differently treated BiOCl samples. An indirect bandgap is assumed, according to literature.[3, 21, 22]

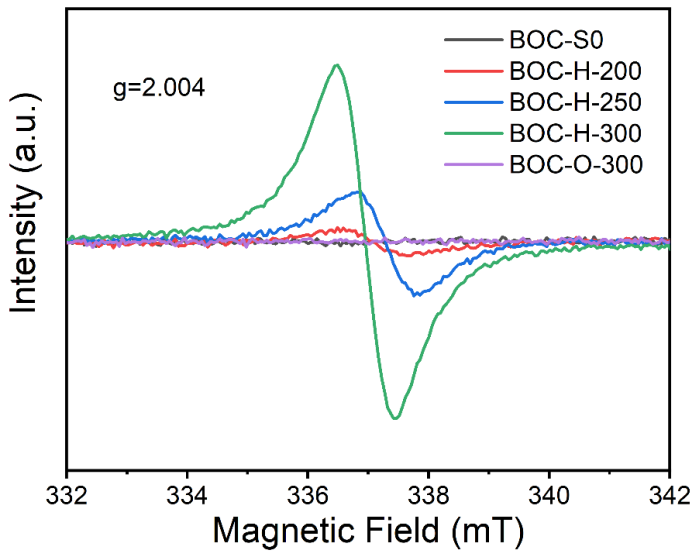

Figure 4.5 EPR spectra of BiOCl nanosheets, measured in the dark at 298 K.[22]

Generally, XPS measurements are employed to characterize OVs at the surface of semiconductors.[29, 30] However, the powder samples are conventionally mounted on the oxygen-containing carbon tape which would significantly affect the detection of OVs. To confirm this point, the XP spectra of BOC-H-300 mounted on carbon tape and filled into homemade Cu sample holder are measured, respectively. They are denoted as BOC-H-300 with conductive carbon tape (CT) and BOC-H-300 without CT. As displayed in **Figure 4.6a**, C 1*s* peaks of BOC-H-300 mainly originate from conductive carbon tape (CT), rather than BOC-H-300 sample. O 1*s* peaks at 531.6 eV and 533.0 eV are attributed to absorbed oxygen species at the surface of CT (**Figure 4.6b**). No binding energy shifts or additional spectral components are discovered in Bi 4*f* (**Figure 4.6c**) and Cl 2p spectra (**Figure 4.6d**), which implies Cu sample holder is suitable to measure XP spectra of BOC samples.

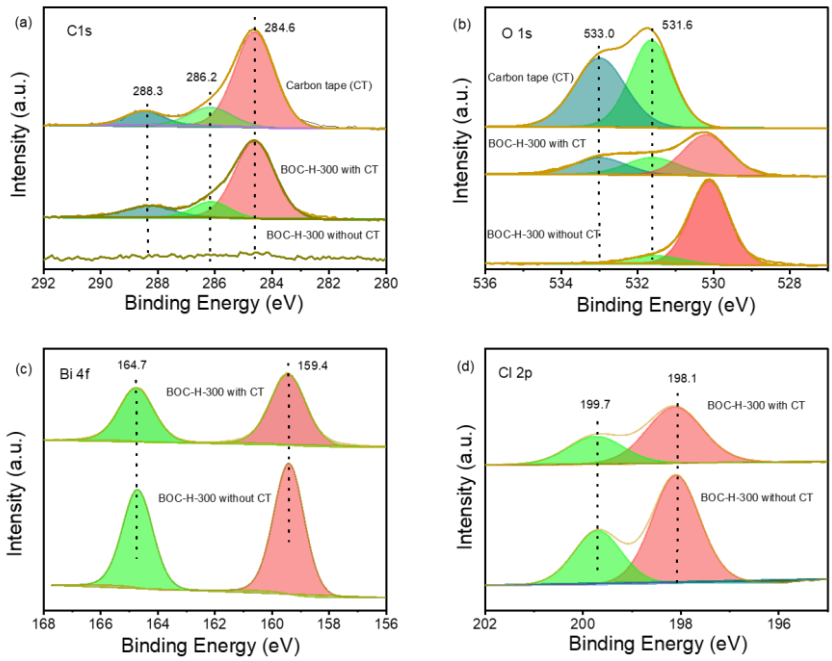

Figure 4.6 C 1*s*, O 1*s*, Bi 4*f* and Cl 2*p* high resolution XP spectra of carbon tape and BOC-H-300, measured at 298 K.[22]

XP spectra of all BOC samples placed onto the Cu sample holder are recorded to detect OVs. According to literature, the relative content of oxygen vacancies can be extracted from the O 1*s* and the corresponding metal high resolution core level XP spectra. For instance, it is possible to indirectly obtain the content of OVs through calculating the ratio of Ce^{3+}/Ce^{4+} in

the Ce 3*d* spectrum or the relative area of O-Ce^{3+} in O 1*s* spectrum.[31] Nevertheless, XPS is very surface sensitive with an information depth of few nanometers, depending on photoelectron kinetic energy. In our case, high resolution XP spectra of Bi 4*f*, O1*s* and Cl 2*p* regions remain almost unchanged with the different treatments indicating the absence of surface OVs (**Figure 4.7a-c**). No changes are observed in valence band XPS. The absence of spectral features between VBM and E_F indicates that there are no occupied defect states in the band gap close to the VBM (**Figure 7d**). The XPS and EPR results taken together with the reported high reactivity of surface OVs in BiOCl,[9] let us presume that surface OVs formed by annealing in He have been quickly replenished by subsequent exposure to ambient air during sample handling and preparation and that the OVs seen by EPR are located mainly in the bulk of the materials.[32]

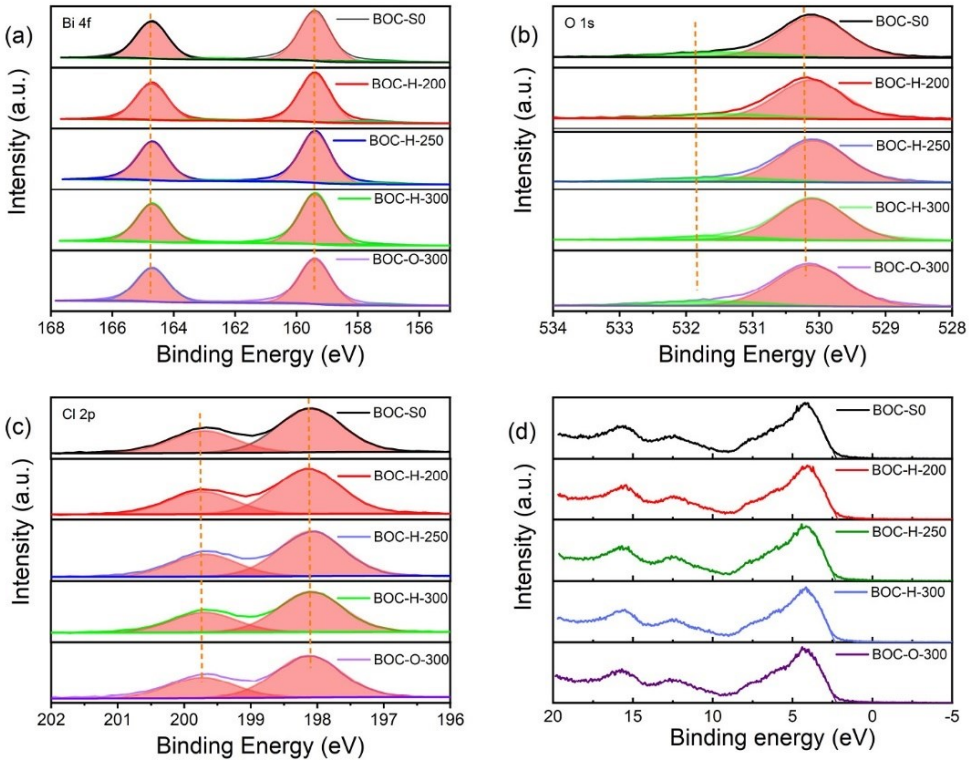

Figure 4.7 Bi 4*f* (a), O 1*s* (b), Cl 2*p* (c) high resolution XP spectra and X-ray valence band spectra (d) of as-prepared BiOCl samples.[22]

Photoluminescence (PL) is commonly used to determine the energy positions of defect states in the band gap and evaluate separation efficiency of photogenerated charge carriers.[33] The range of PL spectral features associated with OVs-created defect states is

relative wide. The PL spectra of the BiOCl samples taken at room temperature show a broad distribution of PL intensity in the range of 340-500 nm (**Figure 4.8**). The distinct peak at 423 nm is associated with a defect state 2.93 eV above valence band maximum (denoted as S_1 in **Figure 4.9**) and corresponds to the main recombination process of charge carriers. The required excitation energy of electrons trapped at S_1 in BOC-H-250 sample is only 0.070 eV (= $E_{CBM} - E_{S1}$), which is close to 3kT (0.078 eV). This means that the trapped electrons can be excited thermally at 298 K. Therefore, S_1 states are not regarded as effective recombination centers for BOC-H-250 and BOC-H-300 samples. However, this excitation energy reaches up to 0.23 eV in BOC-H-200, which makes it less likely that trapped electrons get thermally excited at 298 K. In this sample, additionally, a new deep defect state (denoted as S_2) at 2.56 eV (485 nm) above VBM emerged. These two recombination centers related to defect states contribute to the high photoluminescence intensity for BOC-H-200 sample (**Figure 4.9**). The amount of S_2 will decrease or even disappear with increasing annealing temperature.

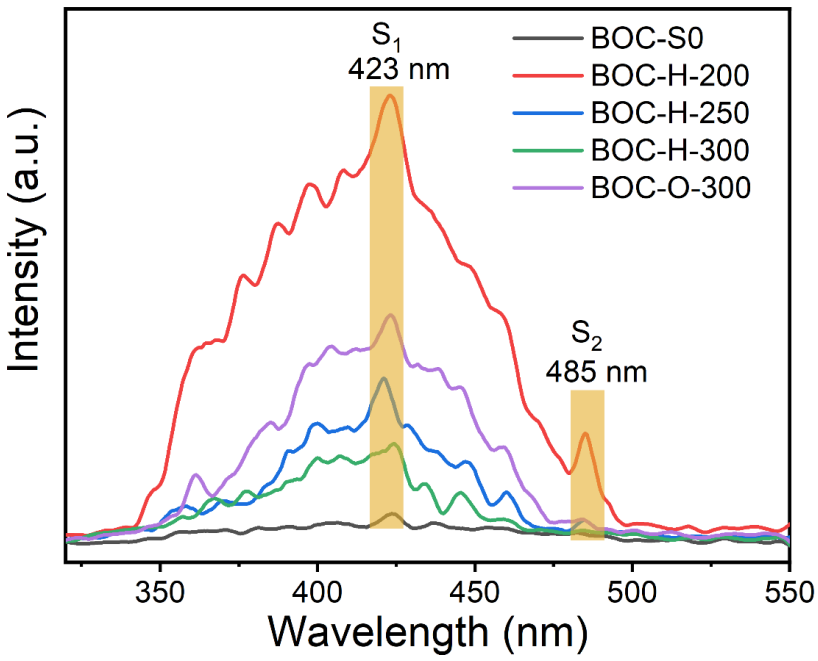

Figure 4.8 Photoluminescence spectra of BiOCl samples, measured at room temperature.[22]

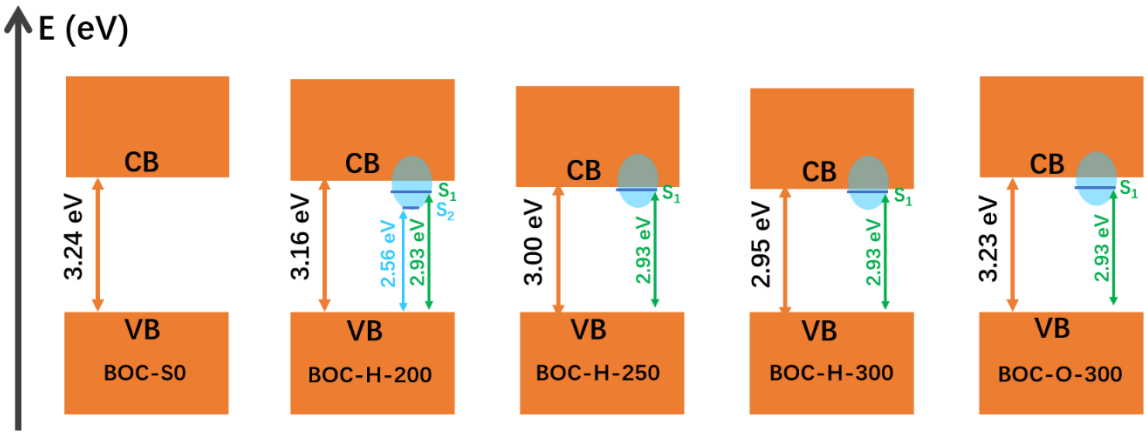

Figure 4.9 Photoluminescence spectra of BiOCl samples, measured at room temperature.[22]

To investigate the mechanism of thermally induced OV formation, in-situ DRIFTS experiments on BOC-S0 were conducted at various temperatures and a pressure <1 mbar. As shown in **Figure 4.10,** a peak centered at 2335 cm^{-1} appeared at 200 °C, which can be ascribed to physisorbed CO_2 after thermal removal of water. The amount of physisorbed CO_2 obviously increases as the amount of adsorbed water decreases. When the temperature increased to 300 °C, CO_2 physisorption became stronger and a noticeable red shift is observed from 2335 cm^{-1} to 2332 cm^{-1}. This change originates from influence of an increased amount of bulk OVs. Meanwhile, a small peak at 2267 cm^{-1} emerged, which can be ascribed to CO_2 chemisorption on Bi^{3+} at the surface of defective BiOCl.[34] Interestingly, these two peaks shift back to their original positions after oxygen treatment at 300 °C for 16 h. This is possibly because most of bulk OVs are healed and lead to reduction of the binding strength of CO_2 molecules at the surface. The CO_2 adsorption process can be understood as depicted in **Figure 4.11**. We anticipate residues of the D-mannitol from synthesis as well as other adventitious carbon species reacting with lattice oxygen of BiOCl as the source for CO_2 in the DRIFTS experiments. This viewpoint is confirmed by the decrease of hydrocarbon related absorption features between 3000-2800 cm^{-1} (C-H stretching region) upon increasing temperature. Moreover, D-mannitol starts to decompose when the temperature increases above 300 °C according to literature.[35] The formation and recovery process of bulk OVs can be described in Kröger-Vink notation as follows. Firstly, bulk OVs are formed in BiOCl samples and O_2 is released at low temperature (eqn. 4.1). Secondly, D-mannitol or adventitious carbon decomposition to

produce CO_2 and water and physisorption occurs at the surface of BiOCl (eqn. 4.2), followed by CO_2 chemisorption on surface Bi^{3+} sites when increasing temperature to 300°C. Finally, bulk OVs are healed by O_2 introduction at 400°C (eqn. 4.3).

$$O_O^X \xrightarrow{\text{heat}} V_O^{\cdot} + e^- + \frac{1}{2}\,O_2 \quad \text{(eqn. 4.1)}$$

$$C_x^{\square} H_y^{\square} + (x + \frac{y}{2})O_2 \xrightarrow{\text{heat}} xCO_2^{\square} + \frac{y}{2} H_2^{\square} O^{\square} \quad \text{(eqn. 4.2)}$$

$$V_O^{\cdot} + e^- + \frac{1}{2}\,O_2 \xrightarrow{\square} O_O^X \quad \text{(eqn. 4.3)}$$

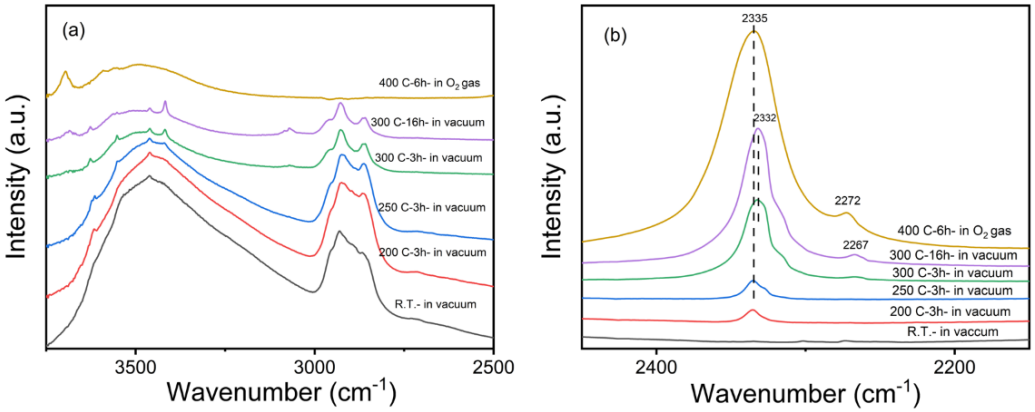

Figure 4.10 *In-situ* DRIFTS of pristine BOC-S0 sample in the range of 2500-3750 cm^{-1} (a) and 2150-2450 cm^{-1}, measured in static vacuum (< 1 mbar) at 298 K.[22]

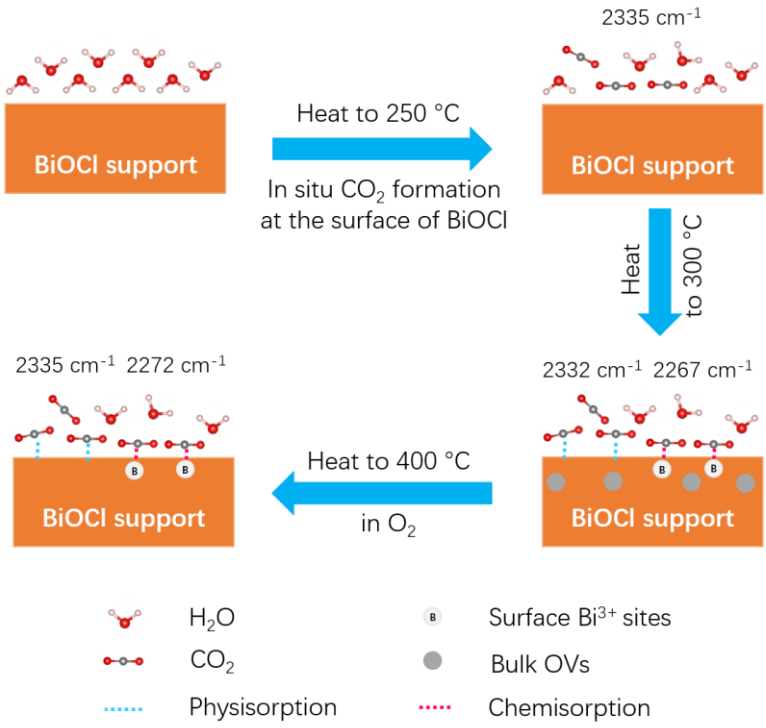

Figure 4.11 Proposed schematic mechanism of BiOCl OVs formation based on *in-situ* DRIFTS results in **Figure 4.10**.[22]

As elaborated above, the OVs of the temperature treated BiOCl samples are located in the bulk rather than at the surface. To further confirm this point, we also measured transmission FTIR spectra of all BiOCl samples pressed into KBr pellets in the evacuated sample compartment of the FTIR spectrometer at reduced pressure of <5 mbar at 298 K (**Figure 4.12**). The peak at 2332 cm^{-1} results from CO_2 physisorption from the residual gas.[36] Interestingly, there are no indications of CO_2 chemisorption in the region of 2260-2270 cm^{-1}, although that would have been expected for defective BiOCl.[34] The high reactivity of surface OVs towards atmospheric oxygen leads to their facile replenishment when in contact to air. Consistently, Zhang et al. reported that surface OVs in BiOCl basically disappeared after repeated use in benzyl alcohol oxidation for 5 times, which implies that surface OVs of BiOCl are highly reactive.[9]

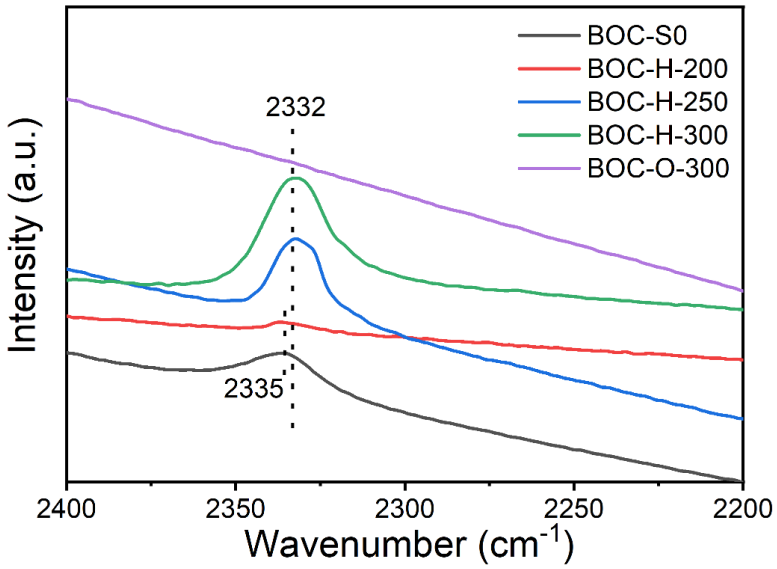

Figure 4.12 Transmission FTIR spectra of BiOCl samples, measured as KBr pellets in static vacuum at 298 K.[22]

4.3.3 Effect of bulk oxygen vacancies on photoelectrochemical performance

To investigate the effect of bulk OVs on the photoelectrochemical performance of BiOCl samples, chopped light voltammetry measurements on BiOCl / FTO glass photoelectrodes were carried out. In spite of similar specific surface areas and morphologies, the differently treated BiOCl materials show remarkably different photocurrents at open circuit potential (**Figure 4.13a**). Photocurrents under irradiation for all samples annealed in He are significantly higher than that of the as-prepared sample, reaching up to 1.17 µA cm^{-2} for BOC-H-300, which is 7 times higher than that of BiOCl (0.13 µA cm^{-2}). In contrast, O_2-annealing seems to be detrimental as the photocurrent for sample BOC-O-300 drops to 0.08 µA cm^{-2}. The maximum theoretically achievable photocurrent density of BiOCl (3.2 eV) is around 500 µA cm^{-2} under 100 mW cm^{-2} simulated solar light illumination.[37] However, the practical photocurrent will strongly be limited by light absorption, separation and transport of charge carriers as well as the rate of the surface redox reactions.[38] Although bulk defects may act as recombination centers for photogenerated charge carriers and are thus unfavorable for photoelectrochemical activity,[20] the overall effect of OVs formation on PEC performance is positive. Moreover, an enhancement of crystallinity in sample BOC-O-300 is not beneficial to the photoelectrochemical properties. A high crystallinity may accelerate the separation and

migration of charge carriers. However, this effect seems not to outweigh the depletion of O vacancies defects in these samples, suggesting that carrier mobility in BiOCl is not the rate-limiting step for the photoelectrochemical performance.

For driving the photoelectrochemical process, the charge carriers need to pass through the space charge region and the electrochemical double layer at the semiconductor solution junction. Electrochemical impedance spectroscopy (EIS) is capable to determine resistances and capacities in the semiconductor solution interface by fitting equivalent circuits. In our study, EIS was conducted at open circuit potential (OCP) in the dark. The BiOCl electrolyte interface can be fit in first approximation by a Randles equivalent circuit, describing charge transfer and diffusion processes (**Figure 4.13b**). The smaller the diameters of the semicircles of the plots, the smaller is the charge transfer resistance and the higher is the charge transfer rate at the interface. Compared to BOC-S0, defective BiOCl samples, i.e., BOC-H-200, BOC-H-250, BOC-H-300 qualitatively possess smaller charge transfer resistances.

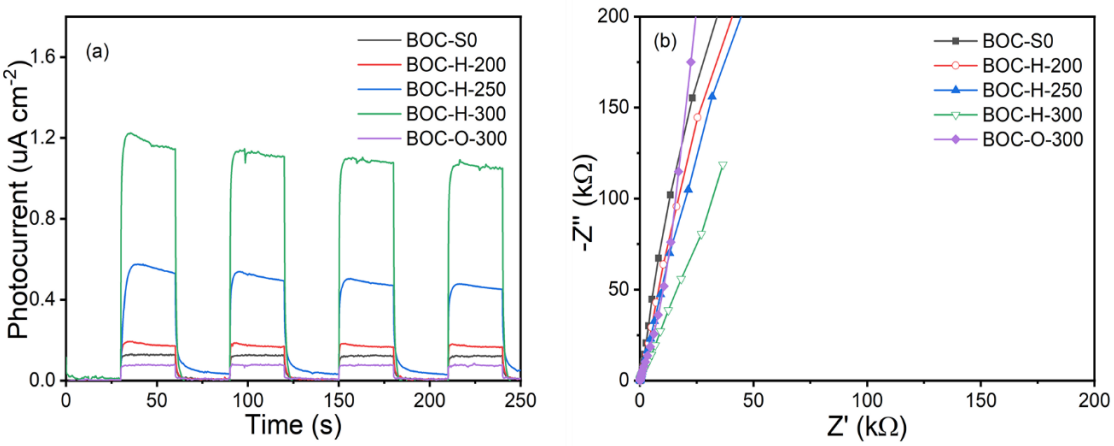

Figure 4.13 Photocurrent density under 100 mW cm^{-2} white LED light illumination (a) and electrochemical impedance spectroscopy in the dark (b) of as-prepared samples measured in 0.1 M sodium phosphate buffer solution containing 0.1 M Na_2SO_3, both at open circuit potential.[22]

Mott-Schottky plots were recorded to determine band alignment and concentrations of charge carriers in the different BiOCl samples. The slopes of the Mott-Schottky plots are positive (**Figure 4.14**), indicating n-type behavior, consistent with literature.[39-41] The open

circuit potential (OCP) and flat band position (E_{fb}) were measured and are summarized in **Table 4.2**. The band bending (U_{bb}) of BiOCl samples was calculated according to the formula: $U_{bb} = OCP - E_{fb}$.[42] The larger upwards band bending results in a larger contact potential difference at the semiconductor-solution interface. In addition, the donor density can be estimated by the slope of the Mott-Schottky plot.

According to the classical Mott-Schottky relationship, the equation can be written as:[43]

$$\frac{1}{C_{sc}} = \frac{2}{e\varepsilon_0\varepsilon_r N_D \cdot A^2}\left(V - V_{fb} - \frac{kT}{e}\right) \quad \text{(eqn. 4.4)}$$

C_{sc} is the space charge layer capacitance of the semiconductor, N_D is the donor density, e is elementary charge 1.60×10^{-19} C, ε_0 is the dielectric constant in vacuum which is equal to 8.85×10^{-14} F cm^{-1}, ε_r is relative dielectric constant of the material with ε_r(BiOCl) = 6.74.[44] A is the actual surface area which can be calculated from the mass and the BET data of the used material, V_{fb} is the flat band potential, k Boltzmann constant, T temperature in Kelvin.

From the Mott-Schottky formula, the donor density can be obtained as follows:

$$N_D = \frac{2}{e\varepsilon_0\varepsilon_r \cdot slope \cdot A^2} \quad \text{(eqn. 4.5)}$$

Obviously, BOC-H-200 sample possesses the highest donor density (1.1×10^{17} cm^{-3}) but does not show the highest photocurrent due to severe bulk recombination which is confirmed by photoluminescence measurements. The donor density of BOC-H-300 (5.20×10^{16} cm^{-3}) is 1.8 times and 3.6 times higher than that of BOC-S0 (2.88×10^{16} cm^{-3}) and BOC-O-300 (1.44×10^{16} cm^{-3}), respectively. Except for BOC-H-200, the photocurrent is proportional to the concentration of charge carriers, which reflects that both of defects and concentration of charge carriers affect the photocurrent density.

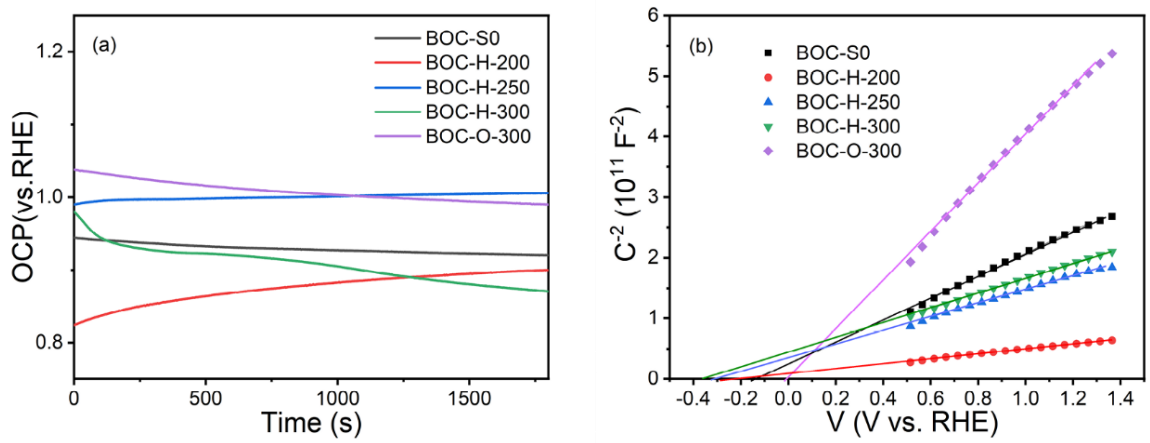

Figure 4.14 Open circuit potentials (a) and Mott-Schottky plots (b) of BiOCl samples.[22]

Table 4.2 Open circuit potential (OCP) values, energy positions of flat band (E_{fb}) and band bending (U_{bb}), the slopes of Mott-Schottky plots and calculated corresponding concentrations of charge carriers measured in 0.5 M Na_2SO_4 solution at 298 K. Error indicators in brackets.[22]

Sample	OCP (V vs. RHE)	E_{fb} (V vs. RHE)	U_{bb}=OCP−E_{fb}	Slope (10^{10} $F^{-2}V^{-1}$)	Concentration of charge carriers (cm^{-3})
BOC-S0	0.93(±0.01)	−0.12(±0.02)	1.05(±0.03)	18.5(±0.2)	2.88(±0.03)×10^{16}
BOC-H-200	0.86(±0.04)	−0.12(±0.04)	0.98(±0.08)	4.09(±0.1)	1.10(±0.03) ×10^{17}
BOC-H-250	1.00(±0.01)	−0.22(±0.02)	1.22(±0.03)	11.7(±0.1)	3.78(±0.03) ×10^{16}
BOC-H-300	0.93(±0.05)	−0.33(±0.03)	1.26(±0.08)	12.7(±0.1)	5.20(±0.04) ×10^{16}
BOC-O-300	1.02(±0.02)	0.00(±0.04)	1.02(±0.06)	40.2(±0.1)	1.44(±0.04) ×10^{16}

The conductivity (σ) of semiconductors is determined by mobility (μ) and concentration (n) of charge carriers according to equation 4.6:

$$\sigma = nq\mu \quad \text{(eqn. 4.6)}$$

with q being the elementary charge.

In this sense, OV related deep defect states as recombination centers are unfavorable to transfer charge carriers, because of their impact on the mobility of charge carriers. However, a moderate amount of shallow defect states from which electrons can easily be excited to the conduction band at room temperature does not only increase the concentration but also the separation efficiency of photogenerated charge carriers. Taking into account the layered structure of BiOCl, the distance of $[Bi_2O_2]^{2+}$ and adjacent Cl^- ion layers is relatively large, which gives rise to weak interaction and high energy barrier for charge carriers migration perpendicular to the sheets. We also can look at this from the point of mobility of charge carriers. According to literature,[45] effective masses of holes along x, y, z direction in BiOCl are $0.95m_0$, $0.95m_0$ and $6.31m_0$, respectively, while effective masses of electrons along x, y, z direction are $0.29m_0$, $0.29m_0$ and $1.15m_0$, respectively. Charge carrier mobility of semiconductors is inversely proportional to their effective mass. Therefore, charge carriers show low mobility in z direction. This phenomenon is also found in other 2D layered semiconductors.[46]

4.4 Conclusions

In summary, the surface of BiOCl is extremely sensitive to temperature and OVs are formed at temperatures as low as 200 °C in inert atmosphere. In-situ DRIFTS results demonstrate that CO_2 can specifically adsorb on the surface of BiOCl nanosheets bearing OVs and the formation process of OVs could be traced by using CO_2 as IR probe molecule. Introduction of OVs not only increases concentration of charge carriers but also gives rise to two kinds of shallow and deep defect states. Shallow defect states as electrons sinks accelerate separation of charge carriers and remarkably enhance the photocurrent, while deep defect states as recombination centers negatively impact on photocurrent. Finally, photoelectrochemical performance of BiOCl nanosheets is dominantly determined by the balance of OV induced generation (doping) and defect mediated recombination of charge carriers. This work sheds light on the important role of bulk defects in influencing the photo(electro)chemical performance of layered inorganic semiconductors.

References

[1] J. Li, H. Li, G. Zhan, L. Zhang, Solar Water Splitting and Nitrogen Fixation with Layered Bismuth Oxyhalides, *Acc. Chem. Res.*, **2017**, *50*, 112-121.

[2] H. Li, J. Li, Z. Ai, F. Jia, L. Zhang, Oxygen Vacancy-Mediated Photocatalysis of BiOCl: Reactivity, Selectivity, and Perspectives, *Angew. Chem. Int. Ed.*, **2017**, *56*, 2-19.

[3] J. Jiang, K. Zhao, X. Xiao, L. Zhang, Synthesis and facet-dependent photoreactivity of BiOCl single-crystalline nanosheets, *J. Am. Chem. Soc.*, **2012**, *134*, 4473-4476.

[4] H. Li, L. Zhang, Photocatalytic performance of different exposed crystal facets of BiOCl, *Curr. Opin. Green Sustain.*, **2017**, *6*, 48-56.

[5] L. Wang, D. Lv, F. Dong, X. Wu, N. Cheng, J. Scott, X. Xu, W. Hao, Y. Du, Boosting Visible-Light-Driven Photo-oxidation of BiOCl by Promoted Charge Separation via Vacancy Engineering, *ACS Sustain. Chem. Eng.*, **2019**, *7*, 3010-3017.

[6] J. Sun, S. Wu, S.-Z. Yang, Q. Li, J. Xiong, Z. Yang, L. Gu, X. Zhang, L. Sun, Enhanced photocatalytic activity induced by sp^3 to sp^2 transition of carbon dopants in BiOCl crystals, *Appl. Catal. B: Environ.*, **2018**, *221*, 467-472.

[7] S. Weng, Z. Fang, Z. Wang, Z. Zheng, W. Feng, P. Liu, Construction of teethlike homojunction BiOCl (001) nanosheets by selective etching and its high photocatalytic activity, *ACS Appl. Mater. Interfaces*, **2014**, *6*, 18423-18428.

[8] A.K. Chakraborty, S.B. Rawal, S.Y. Han, S.Y. Chai, W.I. Lee, Enhancement of visible-light photocatalytic efficiency of BiOCl/Bi_2O_3 by surface modification with WO_3, *Appl. Catal. A: Gen.*, **2011**, *407*, 217-223.

[9] H. Li, F. Qin, Z. Yang, X. Cui, J. Wang, L. Zhang, New Reaction Pathway Induced by Plasmon for Selective Benzyl Alcohol Oxidation on BiOCl Possessing Oxygen Vacancies, *J. Am. Chem. Soc.*, **2017**, *139*, 3513-3521.

[10] H. Li, J. Shi, K. Zhao, L. Zhang, Sustainable molecular oxygen activation with oxygen vacancies on the {001} facets of BiOCl nanosheets under solar light, *Nanoscale*, **2014**, *6*, 14168-14173.

[11] S. Niu, R. Zhang, C. Guo, Oxygen vacancy induced superior visible-light-driven photocatalytic performance in the BiOCl homojunction, *Materials Chemistry Frontiers*, **2020**, *4*, 2314-2324.

[12] Z. Yang, Y. Shi, H. Li, C. Mao, X. Wang, X. Liu, X. Liu, L. Zhang, Oxygen and Chlorine Dual Vacancies Enable Photocatalytic O_2 Dissociation into Monatomic Reactive Oxygen on BiOCl for Refractory Aromatic Pollutant Removal, *Environ. Sci. Technol.*, **2022**, *56*, 3587-3595.

[13] N. Zhang, L. Li, Q. Shao, T. Zhu, X. Huang, X. Xiao, Fe-Doped BiOCl Nanosheets with Light-Switchable Oxygen Vacancies for Photocatalytic Nitrogen Fixation, *ACS Appl. Energy Mater.*, **2019**, *2*, 8394-8398.

[14] H. Li, J. Shang, H. Zhu, Z. Yang, Z. Ai, L. Zhang, Oxygen Vacancy Structure Associated Photocatalytic Water Oxidation of BiOCl, *ACS Catal.*, **2016**, *6*, 8276-8285.

[15] K. Zhao, L. Zhang, J. Wang, Q. Li, W. He, J.J. Yin, Surface structure-dependent molecular oxygen activation of BiOCl single-crystalline nanosheets, *J. Am. Chem. Soc.*, **2013**, *135*, 15750-15753.

[16] Y. Yang, L.C. Yin, Y. Gong, P. Niu, J.Q. Wang, L. Gu, X. Chen, G. Liu, L. Wang, H.M. Cheng, An Unusual Strong Visible-Light Absorption Band in Red Anatase TiO_2 Photocatalyst Induced by Atomic Hydrogen-Occupied Oxygen Vacancies, *Adv. Mater.*, **2018**, *30*, 1704479.

[17] F. Wang, W. Septina, A. Chemseddine, F.F. Abdi, D. Friedrich, P. Bogdanoff, R. van de Krol, S.D. Tilley, S.P. Berglund, Gradient Self-Doped $CuBi_2O_4$ with Highly Improved Charge Separation Efficiency, *J. Am. Chem. Soc.*, **2017**, *139*, 15094-15103.

[18] G. Liu, J. Pan, L.C. Yin, J.T.S. Irvine, F. Li, J. Tan, P. Wormald, H.M. Cheng, Heteroatom-Modulated Switching of Photocatalytic Hydrogen and Oxygen Evolution Preferences of Anatase TiO_2 Microspheres, *Adv. Funct. Mater.*, **2012**, *22*, 3233-3238.

[19] M. Kong, Y. Li, X. Chen, T. Tian, P. Fang, F. Zheng, X. Zhao, Tuning the relative concentration ratio of bulk defects to surface defects in TiO_2 nanocrystals leads to high photocatalytic efficiency, *J. Am. Chem. Soc.*, **2011**, *133*, 16414-16417.

[20] Y. Zhu, Q. Ling, Y. Liu, H. Wang, Y. Zhu, Photocatalytic performance of $BiPO_4$ nanorods adjusted via defects, *Appl. Catal. B: Environ.*, **2016**, *187*, 204-211.

[21] M. Guan, C. Xiao, J. Zhang, S. Fan, R. An, Q. Cheng, J. Xie, M. Zhou, B. Ye, Y. Xie, Vacancy associates promoting solar-driven photocatalytic activity of ultrathin bismuth oxychloride nanosheets, *J. Am. Chem. Soc.*, **2013**, *135*, 10411-10417.

[22] Xiaofeng Wu, Freddy E. Oropeza, Daan den Boer, Peter Kleinschmidt, Thomas Hannappel, Dennis G. H. Hetterscheid, Emiel J. M. Hensen, J.P. Hofmann, Thermally Induced Oxygen Vacancies in BiOC Nanosheets and Their Impact on Photoelectrochemical Performance, *ChemPhotoChem*, **2022**, e202200192

[23] H.J. Yu, R. Shi, Y.X. Zhao, T. Bian, Y.F. Zhao, C. Zhou, G.I.N. Waterhouse, L.Z. Wu, C.H. Tung, T.R. Zhang, Alkali-Assisted Synthesis of Nitrogen Deficient Graphitic Carbon Nitride with Tunable Band Structures for Efficient Visible-Light-Driven Hydrogen Evolution, *Adv. Mater.*, **2017**, *29*, 1605148.

[24] Z. Ma, P. Li, L. Ye, Y. Zhou, F. Su, C. Ding, H. Xie, Y. Bai, P.K. Wong, Oxygen vacancies induced exciton dissociation of flexible BiOCl nanosheets for effective photocatalytic CO_2 conversion, *J. Mater. Chem. A*, **2017**, *5*, 24995-25004.

[25] S. Wu, J. Xiong, J. Sun, Z.D. Hood, W. Zeng, Z. Yang, L. Gu, X. Zhang, S.Z. Yang, Hydroxyl-Dependent Evolution of Oxygen Vacancies Enables the Regeneration of BiOCl Photocatalyst, *ACS Appl. Mater. Interfaces*, **2017**, *9*, 16620-16626.

[26] J. Li, G. Lu, G. Wu, D. Mao, Y. Guo, Y. Wang, Y. Guo, Effect of TiO_2 crystal structure on the catalytic performance of Co_3O_4/TiO_2 catalyst for low-temperature CO oxidation, *Catal. Sci. Technol.*, **2014**, *4*, 1268-1275.

[27] I. Popescu, I.C. Marcu, Insights into the electronic and redox behavior of surface-phosphated ceria catalysts in correlation with their propane oxydehydrogenation performance, *Phys. Chem. Chem. Phys.*, **2021**, *23*, 5897-5907.

[28] X. Liu, Y. Su, Q. Zhao, C. Du, Z. Liu, Constructing $Bi_{24}O_{31}Cl_{10}$/BiOCl heterojunction via a simple thermal annealing route for achieving enhanced photocatalytic activity and selectivity, *Sci. Rep.*, **2016**, *6*, 28689.

[29] J. Wan, W. Chen, C. Jia, L. Zheng, J. Dong, X. Zheng, Y. Wang, W. Yan, C. Chen, Q. Peng, D. Wang, Y. Li, Defect Effects on TiO_2 Nanosheets: Stabilizing Single Atomic Site Au and Promoting Catalytic Properties, *Adv. Mater.*, **2018**, *30*, 1705369.

[30] H. Li, J. Shang, Z. Ai, L. Zhang, Efficient Visible Light Nitrogen Fixation with BiOBr Nanosheets of Oxygen Vacancies on the Exposed {001} Facets, *J. Am. Chem. Soc.*, **2015**, *137*, 6393-6399.

[31] S.M. S, E. Adabifiroozjaei, Y. Yao, P. Koshy, S. Lim, R. Webster, X. Liu, R. Khayyam Nekouei, C. Cazorla, Z. Liu, Y. Wang, N. Lambropoulos, C.C. Sorrell, Proton-assisted creation of controllable volumetric oxygen vacancies in ultrathin CeO_{2-x} for pseudocapacitive energy storage applications, *Nat. Commun.*, **2019**, *10*, 2594.

[32] H. Idriss, On the wrong assignment of the XPS O1s signal at 531–532 eV attributed to oxygen vacancies in photo- and electro-catalysts for water splitting and other materials applications, *Surf. Sci.*, **2021**, *712*, 121894.

[33] W.J. Kim, D. Pradhan, B.-K. Min, Y. Sohn, Adsorption/photocatalytic activity and fundamental natures of BiOCl and $BiOCl_xI_{1-x}$ prepared in water and ethylene glycol environments, and Ag and Au-doping effects, *Appl. Catal. B: Environ.*, **2014**, *147*, 711-725.

[34] M. Wang, J. Liu, C. Guo, X. Gao, C. Gong, Y. Wang, B. Liu, X. Li, G.G. Gurzadyan, L. Sun, Metal–organic frameworks (ZIF-67) as efficient cocatalysts for photocatalytic reduction of CO_2: the role of the morphology effect, *J. Mater. Chem. A*, **2018**, *6*, 4768-4775.

[35] P.Y.a.T. Byron, Characterization of D-Mannitol by Thermal Analysis, FTIR, and Raman Spectroscopy, *Am. Lab.*, **2008**, *40*, 24-27.

[36] M. Mihaylov, K. Chakarova, S. Andonova, N. Drenchev, E. Ivanova, E.A. Pidko, A. Sabetghadam, B. Seoane, J. Gascon, F. Kapteijn, K. Hadjiivanov, Adsorption of CO_2 on MIL-53(Al): FTIR evidence of the formation of dimeric CO_2 species, *Chem. Commun.*, **2016**, *52*, 1494-1497.

[37] Z. Chen, T.F. Jaramillo, T.G. Deutsch, A. Kleiman-Shwarsctein, A.J. Forman, N. Gaillard, R. Garland, K. Takanabe, C. Heske, M. Sunkara, E.W. McFarland, K. Domen, E.L. Miller, J.A. Turner, H.N. Dinh, Accelerating materials development for photoelectrochemical

hydrogen production: Standards for methods, definitions, and reporting protocols, *J. Mater. Res.*, **2011**, *25*, 3-16.

[38] H. Dotan, K. Sivula, M. Grätzel, A. Rothschild, S.C. Warren, Probing the photoelectrochemical properties of hematite (α-Fe_2O_3) electrodes using hydrogen peroxide as a hole scavenger, *Energy Environ. Sci*, **2011**, *4*, 958-964.

[39] H. Fujito, H. Kunioku, D. Kato, H. Suzuki, M. Higashi, H. Kageyama, R. Abe, Layered Perovskite Oxychloride Bi_4NbO_8Cl: A Stable Visible Light Responsive Photocatalyst for Water Splitting, *J. Am. Chem. Soc.*, **2016**, *138*, 2082-2085.

[40] L. Yu, X. Zhang, G. Li, Y. Cao, Y. Shao, D. Li, Highly efficient $Bi_2O_2CO_3$ /BiOCl photocatalyst based on heterojunction with enhanced dye-sensitization under visible light, *Appl. Catal. B: Environ.*, **2016**, *187*, 301-309.

[41] J. Stephenson, V. Celorrio, D. Tiwari, S.R. Hall, D.C. Green, D.J. Fermín, Photoelectrochemical properties of BiOCl microplatelets, *J. Electroanal. Chem.*, **2018**, *819*, 171-177.

[42] F.A. Harraz, J. Sasano, T. Sakka, Y.H. Ogata, Different Behavior in Immersion Plating of Nickel on Porous Silicon from Acidic and Alkaline Fluoride Media, *J. Electrochem. Soc.*, **2003**, *150*, C277-C284.

[43] B. Bera, A. Chakraborty, T. Kar, P. Leuaa, M. Neergat, Density of States, Carrier Concentration, and Flat Band Potential Derived from Electrochemical Impedance Measurements of N-Doped Carbon and Their Influence on Electrocatalysis of Oxygen Reduction Reaction, *J. Phys. Chem. C*, **2017**, *121*, 20850-20856.

[44] L. Zhao, X. Zhang, C. Fan, Z. Liang, P. Han, First-principles study on the structural, electronic and optical properties of BiOX (X=Cl, Br, I) crystals, *Physica B: Condensed Matter*, **2012**, *407*, 3364-3370.

[45] Z. Ran, X. Wang, Y. Li, D. Yang, X.-G. Zhao, K. Biswas, D.J. Singh, L. Zhang, Bismuth and antimony-based oxyhalides and chalcohalides as potential optoelectronic materials, *Npj Comput. Mater.*, **2018**, *4*, 14.

[46] Y.Y. Kang, Y.Q. Yang, L.C. Yin, X.D. Kang, L.Z. Wang, G. Liu, H.M. Cheng, Selective Breaking of Hydrogen Bonds of Layered Carbon Nitride for Visible Light Photocatalysis, *Adv. Mater.*, **2016**, *28*, 6471-6477.

5. Influence of Mo doping on interfacial charge carrier dynamics in photoelectrochemical water oxidation on $BiVO_4$[2]

The understanding of interfacial charge transfer processes is vital to the design of efficient photoanodes in photoelectrochemical (PEC) water splitting. Bismuth vanadate ($BiVO_4$) is a promising photoanode material to drive the oxygen evolution reaction (OER). However, intrinsic $BiVO_4$ suffers from a slow charge carrier mobility and sluggish OER kinetics, which gives rise to a high charge carrier recombination rate and unsatisfactory photoelectrochemical performance. Although the impact of metal doping of $BiVO_4$ in the field of photocatalysis and photoelectrochemistry has been investigated in literature, a detailed understanding of the interfacial charge carrier dynamics in dependence of surface configuration is still required for further PEC device optimization.

In this work, $BiVO_4$ film samples were prepared by a modified metal organic precursor decomposition method. Effects of molybdenum (Mo) doping on the photocurrent density, electrochemical impedance spectra and interfacial charge transfer kinetics of $BiVO_4$ were investigated. Our results indicate: (1) interfacial charge transfer resistances (R_{ct}) of $BiVO_4$ in 0.1 M phosphate buffer solution decrease 2 to 3 orders of magnitude under illumination. (2) Intensity of the photocurrent is predominantly limited by R_{ct}, rather than the semiconductor bulk resistance (R_{bulk}). (3) Mo doping not only increases photovoltage, but also obviously decreases R_{ct}. (4) Compared to pristine $BiVO_4$, Mo doping leads to an enhancement of photocurrent density at 1.23 V vs. RHE to 25.3 μA cm^{-2}, i.e., by a factor 2.7.

5.1 Introduction

Photoelectrochemical water splitting is regarded as a promising approach to convert and store solar energy in H_2.[1] Compared to the photocathodic half reaction, the oxygen evolution reaction (OER) in photoelectrochemical water splitting is more complex due to involvement of multiple proton-coupled electron transfer steps.[2, 3] Monoclinic bismuth vanadate ($BiVO_4$), as a promising photoanode material, has drawn significant attention due to its high absorption

[2] This chapter has been published in: **Xiaofeng Wu,** Freddy E. Oropeza, Zheng Qi, Marcus Einert, Chuanmu Tian, Clément Maheu, Kangle Lv and Jan P. Hofmann, Influence of Mo doping on interfacial charge carrier dynamics in photoelectrochemical water oxidation on $BiVO_4$, *Sustainable Energy & Fuels*, **2023,** 7, 2923-2933.

coefficient, suitable band edge positions for redox reactions, long charge carrier lifetime and chemical stability.[4, 5] However, intrinsic $BiVO_4$ still suffers from a low charge carrier mobility, which gives rise to a small diffusion length of holes. According to previous literatures, the hole diffusion length of $BiVO_4$ is reported to be 70-100 nm.[6-8] Nevertheless, recent study based on a more reliable approach indicated that it may be overestimated and only 15 nm.[9] On the other hand, the oxygen evolution reaction (OER) process is kinetically sluggish due to the proton-coupled four-electron transfer at the semiconductor-electrolyte interface.[10]

Morphology control of $BiVO_4$ is an effective approach to overcome the drawback of small carrier diffusion length and therefore has been employed for enhancing photoelectrochemical performance. Up to date, plates, dendrite-like, and worm-like shapes of $BiVO_4$ have been synthesized for increasing the number of active sites and reducing the required migration lengths for charge transfer.[11-13] For example, Zou et al. confirmed that the charge carrier separation efficiency of porous worm-like $BiVO_4$ films is twice higher than that of dense $BiVO_4$ films due to lower bulk recombination of the charge carriers.[14] On the other hand, lots of works have been dedicated to increase the charge carrier concentration and conductivity of semiconductors by metal/non-metal doping, which can alleviate the disadvantage of small charge carrier mobility.[6, 15, 16]

In order to solve the problem of slow reaction kinetics of the OER, loading oxidation co-catalysts, such as IrO_2, RuO_2, and CoO_x, is conventionally considered as a superior strategy, as it can change the reaction paths and lower the activation energy barrier of the rate-determining steps in OER.[17, 18] For instance, Gong and co-workers achieved a photocurrent of 2.71 mA cm^{-2} at 1.23 V vs. RHE by loading a moderate amount of Co_3O_4 on $BiVO_4$, which is 5 times higher than the photocurrent of bare $BiVO_4$.[19]

Although the influence of doping on the photoelectrochemical performance of $BiVO_4$ has been investigated, a concrete and comprehensive understanding on interfacial charge carrier dynamics is still needed.

In this study, Mo doped $BiVO_4$ photoanodes were prepared by a two-step spin coating-calcination approach. The effect of doping on the photoelectrochemical performance of OER are systemically investigated from the aspect of interfacial resistance and interfacial transfer of charge carriers. We believe that insights into the interfacial charge transfer processes is the

key to better understand the roles of dopants on $BiVO_4$ photoanodes in order to further improve the overall PEC performance.

5.2 Experimental section

5.2.1 Sample preparation

Pristine $BiVO_4$ films were synthesized by a modified metal organic decomposition method according to literature.[20] First, ITO substrates (2×2 cm^2) were cleaned by sonication in distilled water, acetone, and ethanol for 15 min each and then calcined at 470 °C for 2 h to remove adventitious organic compounds. The ITO substrates were covered with tape at the edge to leave a blank area for later conductive connection. To prepare the precursor solutions, 1 mmol of $Bi(NO_3)_3{\cdot}5H2O$ (99.99%, Sigma-Aldrich) was dissolved in 4 mL of 2-methoxyethanol (99.5%, Carl Roth), which forms a colorless solution. 1 mmol of vanadyl-acetylacetonate (98%, Sigma-Aldrich) was dissolved in 4 mL of methanol and forms a dark blue solution. Subsequently, the dark blue solution was carefully added into the bismuth-containing colorless solution. 0.5 mL of acetylacetone (99%, Sigma-Aldrich) was added for adjusting the viscosity of the resulting solution. Finally, 50 µL of this solution was spin coated (1800 rpm, 1 min) on the cleaned ITO substrates. After preheated at 150 °C for 10 min, the substrates were calcined in air at 470 °C for 2 h in a muffle furnace. For Mo doped $BiVO_4$ films, bis(acetylacetonato) dioxomolybdenum (VI) (CAS No. 17524-05-9, Sigma-Aldrich) was used as Mo source, a stoichiometric ratio of V to Mo compounds (0.97 mmol: 0.03 mmol) in methanol was prepared as precursor solution. The spin coating and calcination processes are the same to those for pristine $BiVO_4$. The obtained samples were denoted as BVO and Mo-BVO.

5.2.2 Materials characterization

XRD pattern was recorded from 10° to 70° on a Bruker D8 Advance diffractometer with monochromatic Cu Kα radiation (λ = 1.54178 Å) at a scan rate of 0.02° min^{-1}. The morphologies of all samples were assessed by field emission scanning electron microscopy (FESEM, SU8010, Hitachi). UV-Vis-NIR spectra were measured on a Cary 7000 universal measurement spectrometer (Agilent Technologies, Santa Clara, USA). The sample orientation was set as 6° and baseline was corrected against air. The transmission and reflectance spectra were recorded and absorption spectra in percentage were obtained by subtracting transmission

and reflectance spectra from 1. X-ray photoelectron spectra (XPS) were recorded on a Thermo Fisher Escalab 250 with a monochromic Al Kα X-ray source (hv = 1486.6 eV) set at 13 mA and 15 kV. The pressure inside the analytical chamber was monitored below 5×10^{-9} mbar. The high-resolution core-level spectra were acquired with a pass energy of 10 eV, a step size of 0.05 eV, and a dwell time of 50 ms per measurement point. All XP spectra were calibrated by setting Bi $4f_{7/2}$ spectrum to 159.0 eV. An electron gun was used to compensate for surface charging. The reflectance FTIR measurements were performed on a Bruker VERTEX 80v spectrometer, equipped with MCT detector, and the incidence angle was set at 60°. A flat aluminum (Al) mirror was used for background correction. FTIR spectra were acquired at a resolution of 2 cm^{-1} by averaging 100 scans in the range of 400-4000 cm^{-1}. Raman spectra were obtained from 50 - 3000 cm^{-1} with excitation wavelength of 514 nm on a micro-Raman HR800 spectrometer (Horiba Jobin Yvon, Bensheim, Germany).

5.2.3 Photoelectrochemical measurement

Photoelectrochemical characterization was performed in three electrode configuration (PECC-2 cell Zahner Elektrik GmbH, Germany). The working electrodes consisting of $BiVO_4$ film samples were electrically connected by copper tape (**Figure 5.1**). Ag/AgCl and Pt wire were used as reference electrode and counter electrode, respectively. 0.1 M sodium phosphate buffer solution (KPi, pH 6.8) and 0.5 M sodium sulfite solution were used as electrolytes. The photoelectrochemical performance was evaluated by linear sweep voltammetry which was carried out in a bias range of +0.6 V_{RHE} to +1.8 V_{RHE} at a scan rate of 10 mV s^{-1}. EIS measurements were conducted at +1.2 V_{RHE} by applying a sine 10 mV signal AC amplitude in the frequency range of 0.1 Hz to 10 KHz. Modulated illumination was provided by blue emitting diode (435 nm, 100 mW cm^{-2}) and the irradiation active area was 0.283 cm^2. Mott Schottky plots were measured from +0.2 V to +1.0 V at a frequency of 1 kHz in 0.1 M KPi solution. Intensity modulated photocurrent spectroscopy (IMPS) spectra were collected at +1.2 V_{RHE} in 0.1 M KPi solution in the range of 0.1 Hz to 10 kHz. Intensity and small AC perturbation of 435 nm LED light were set to 100 mW cm^{-2} and 10%, respectively.

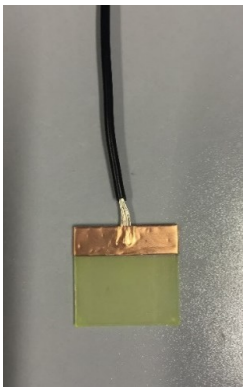

Figure 5.1 Contacting of BVO photoelectrode.[11]

5.3 Results and discussion

5.3.1 Crystal structure, morphology, and light absorption

Pristine BVO and Mo-BVO films were prepared in this work. XRD pattern of all BVO thin film samples are consistent with monoclinic $BiVO_4$ (JCPDS No. 14-0688), indicating that no obvious secondary phases were formed during doping and annealing processes (**Figure 5.2**). The phase purity of $BiVO_4$ films was also confirmed by their Raman spectra (see **Figure 5.7** and discussion below). Typical morphologies of pristine BVO and Mo-BVO films samples are shown in **Figure 5.3**. The thickness of pristine BVO film is about 500 nm and the width of tightly connected wormlike $BiVO_4$ chains is around 50-100 nm, respectively (**Figure 5.3a** and **Figure 5.3c**). This chain-like morphology remains after Mo doping (**Figure 5.3b**).

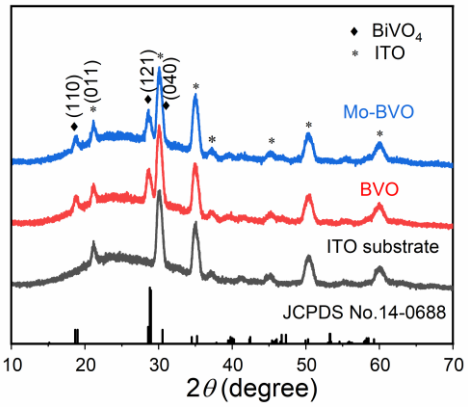

Figure 5.2 XRD pattern of annealed BVO (red) and Mo-BVO (blue) film samples, ITO substrate was measured as reference.[11]

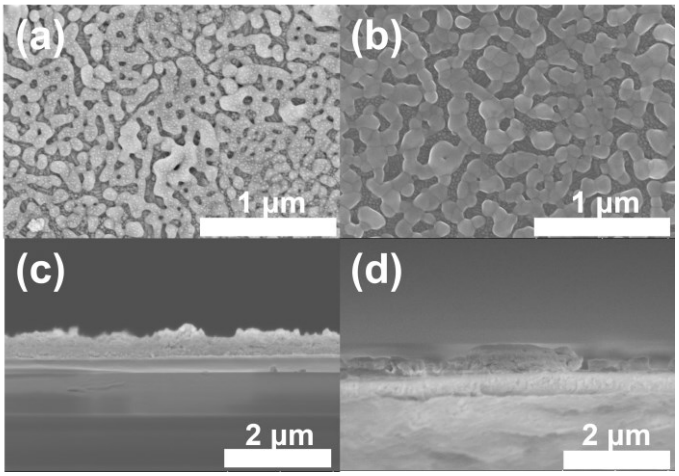

Figure 5.3 SEM images of BVO (a), Mo-BVO (b) and cross-sections of BVO (c) and Mo-BVO (d).[11]

UV-Vis-NIR spectra were recorded to determine the light absorption characteristics of as-prepared BVO samples (**Figure 5.4a**). Bare ITO substrate shows an onset of the optical transition energy at 3.0 eV, which does not affect the bandgap determination of BVO samples. Intrinsic $BiVO_4$ is an indirect semiconductor with a bandgap of 2.4 eV, but its direct optical transition occurs only 200 meV above the conduction band minimum (CBM), explaining the high visible light absorption coefficient.[12-14] The bandgaps of BVO and Mo-BVO were determined to 2.49 eV and 2.54 eV, respectively. This implies that Mo doping barely affect the optical bandgap of BVO.

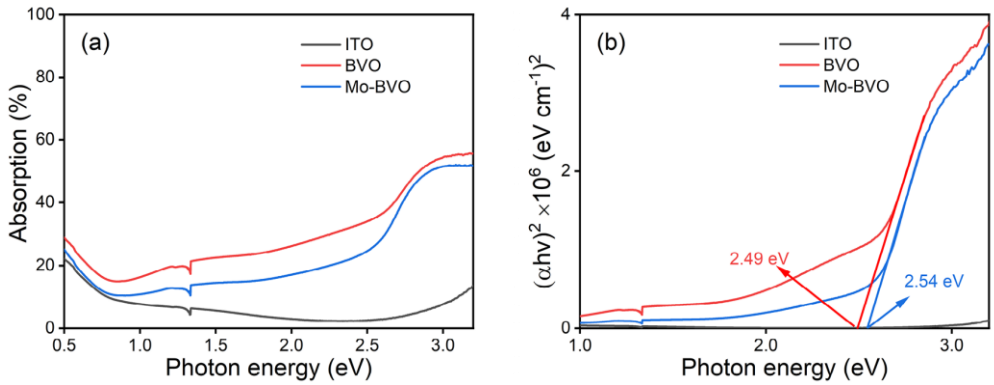

Figure 5.4 UV-Vis-NIR absorption spectra (a) and corresponding Tauc plots (b) of as-prepared $BiVO_4$ film samples, assuming direct optical absorption.[11]

5.3.2 Surface analysis of as-prepared BVO samples by X-ray photoemission spectroscopy, specular reflectance FTIR and Raman spectroscopy

To further analyze doping and surface species, X-ray photoemission spectra (XPS) of $BiVO_4$ films were recorded. The emission at a binding energy of 159.0 eV is ascribed to Bi $4f_{7/2}$ (**Figure 5.5a**).[15] The two peaks at 524.2 eV and 516.6 eV are attributed to V $2p_{1/2}$ and V $2p_{3/2}$, respectively (**Figure 5.5b**).[16] The binding energies of these states show negligible variation when going from BVO to Mo-BVO. The O1*s* emissions located at 529.8 eV, 530.8 eV and 532.5 eV can be ascribed to lattice oxygen, surface –OH groups and adsorbed oxygen species, respectively.[17-19] Mo $3d_{3/2}$ and $3d_{5/2}$ states show up at 235.2 eV and 232.1 eV, respectively, indicating that Mo^{6+} ions are successfully introduced into $BiVO_4$ (**Figure 5.5e**).[20, 21] Additionally, trace N element is observed in BVO and Mo-BVO samples. N 1*s* binding energy shifts from 400.0 eV of BVO to 398.0 eV of Mo-BVO, implies two kinds of N (**Figure 5.5d**). However, peak shifts caused by doping in metal oxides semiconductors are usually small due to limited shifts of the Fermi level. For instance, N 1*s* binding energy shifts from 400.0 eV to 399.6 eV, when the nitrogen content in N-doped TiO_2 increases from 0.5 % to 5 %.[22] Herein, we infer that N originated from $Bi(NO_3)_3$ precursor decomposition and only exists at the surface. The four peaks of C 1*s* at 288.4 eV, 285.5 eV, 284.8 eV and 284.5 eV are assigned to C=O, C-O-C, C-C and C=C entities, respectively. The assignment of C=O in BVO and Mo-BVO at 288.4 eV mainly originates from adsorbed adventitious carbon. On the other hand, the assignments of C-C in BVO at 284.8 eV and C=C in Mo-BVO at 284.5 eV indicate two kinds of carbon species (sp^2 and sp^3 carbon). Combined with Raman results (see below), we infer that short sp^3 carbon chains and short sp^2 carbon chains exist on BVO and Mo-BVO, respectively.

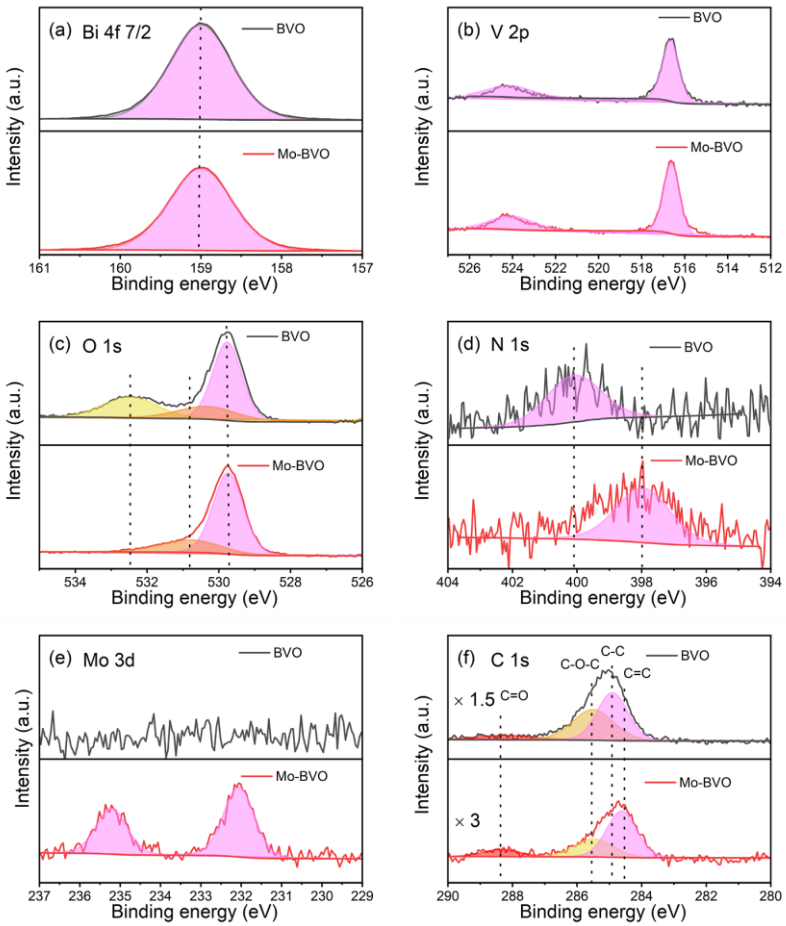

Figure 5.5 High resolution XPS spectra of Bi 4$f_{7/2}$ (a), V 2*p* (b), O 1*s* (c), N 1*s* (d), Mo 3*d* (e) and C 1*s* (f) of as-prepared BVO samples.[11]

To obtain further insight into the speciation of surface functional groups of as-prepared BVO samples, specular reflectance FTIR spectra were recorded. Characteristic peaks of as-prepared films are displayed in **Figure 5.6a**. The peaks located at 1232 cm^{-1} and 1066 cm^{-1} are ascribed to longitudinal optical (LO) and transversal optical (TO) Si-O-Si vibration mode of ITO glass.[23] In the typical C-H stretching vibration ν(C-H) region of 2800- 3000 cm^{-1}, 2960 cm^{-1} is attributed to asymmetric stretching vibration mode of -CH_3 functional groups while 2915 cm^{-1} and 2848 cm^{-1} are attributed to asymmetric and symmetric stretching of -CH_2- groups, respectively.[24] As shown in **Figure 5.6b**, both BVO and Mo-BVO show trace amounts of -CH_2- carbon chain species.

Raman spectra of all samples are presented in **Figure 5.7a**. The bands located at 207, 322, 364, 710, 825 cm^{-1} are attributed to characteristic peaks of monoclinic $BiVO_4$.[25, 26] The band

at 207 cm^{-1} is assigned to the external mode of VO_4^{3-} group. The motion frequencies of external modes in polyatomic ions are usually much lower than that of internal modes due to their heavier masses.[27] The bands at 322 cm^{-1} and 364 cm^{-1} are associated with the asymmetric and symmetric bending vibration modes of the VO_4^{3-} group, while the bands at 710 cm^{-1} and 825 cm^{-1} are attributed to asymmetric and symmetric stretching vibration modes of the V-O bond, respectively. As shown in **Figure 5.7b**, the main peak of $BiVO_4$ originated from symmetric stretching vibration of V-O band shifts from 825.6 cm^{-1} to 823.6 cm^{-1}, which is indicative of Mo ions being doped into $BiVO_4$.[28]

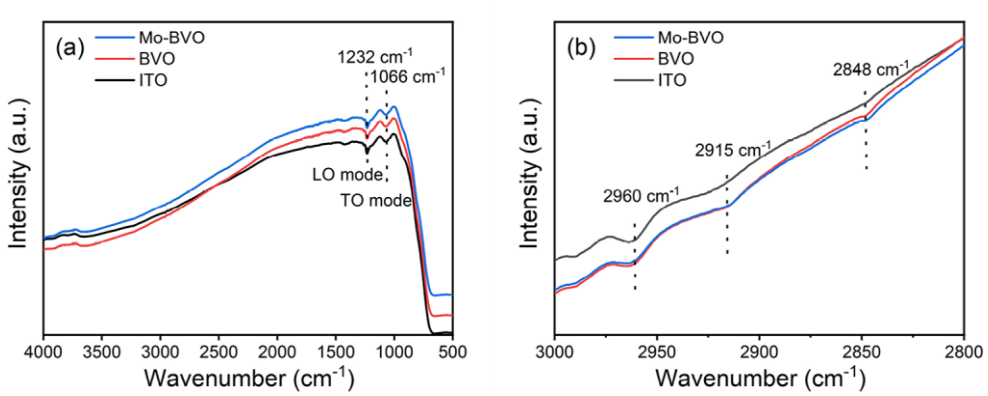

Figure 5.6 Reflectance FTIR spectra of as-prepared BVO films (a) and enlarged region of 2800-3000 cm^{-1} (b).[11]

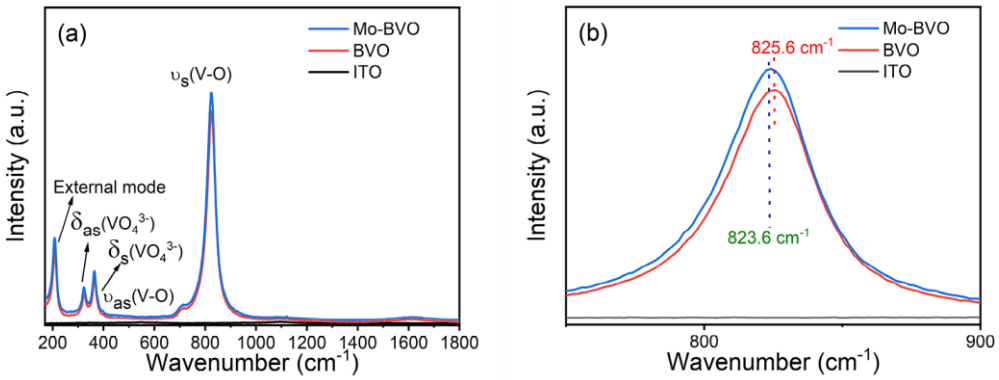

Figure 5.7 Raman spectra of as-prepared BVO films (a) and enlarged regions of 750-900 cm^{-1} (b).[11]

5.3.3 Photoelectrochemical measurements

5.3.3.1 Effect of Mo doping on the photoelectrochemical performance

The photoelectrochemical activity of as-prepared photoanodes is evaluated by linear sweep voltammetry (LSV) curves. **Figure 5.8a** depicts the photoelectrochemical performance of all samples in 0.1 M phosphate buffer solution (pH 6.8). As expected, little current densities of BVO and Mo-BVO are observed in dark due to a high overpotential and a sluggish oxidation process for OER. The photocurrent densities of BVO and Mo-BVO measured at 1.23 V vs. RHE under illumination are 9.5 µA cm^{-2} and 25.2 µA cm^{-2}, respectively. To calculate charge transfer efficiency, LSV curves of BVO and Mo-BVO were measured in a 0.5 M Na_2SO_3 solution, their dark current densities at 1.23 V vs. RHE are 10 µA cm^{-2} and 38 µA cm^{-2} , indicating oxidation potential of Na_2SO_3 solution is below 1.23 eV, consistent with literature.[29] Photocurrent densities of BVO and Mo-BVO at 1.23 V vs. RHE noticeably increase to 319 µA cm^{-2} and 321 µA cm^{-2} (**Figure 5.8b**), using Na_2SO_3 as an effective hole scavenger and the charge transfer resistance (R_{ct}) can be neglected at this potential.[30]

The charge transfer efficiency $\boldsymbol{\eta_{trans}}$ curves of BVO and Mo-BVO can be obtained by using the equation (**Figure 5.8c**):

$$\boldsymbol{\eta_{trans}} = \frac{\boldsymbol{j_{H_2O}}}{\boldsymbol{j_{Na_2SO_3}}} \qquad \text{(eqn. 5.1)}$$

Charge transfer efficiencies of BVO and Mo-BVO are 6.8% and 13.7%, respectively. It indicates that Mo doping can accelerate charge transfer at the interface by a factor of 2-3.

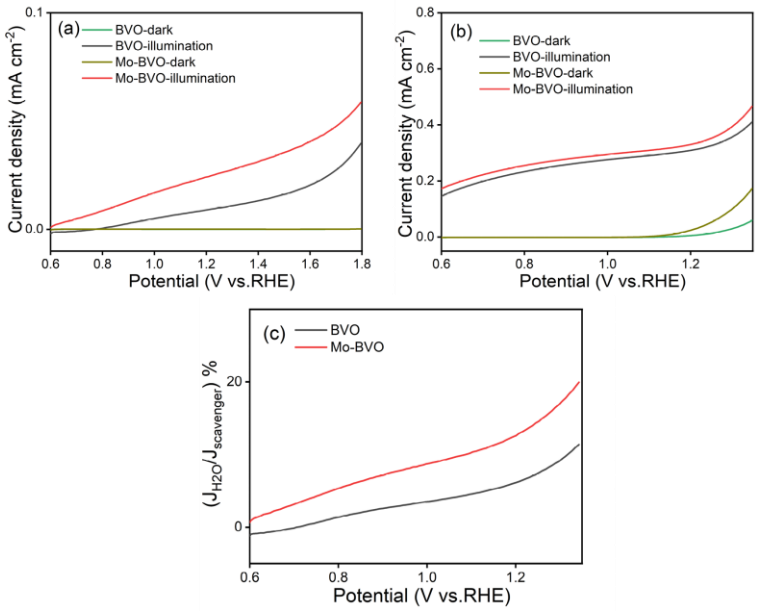

Figure 5.8 Linear sweep voltammetry (LSV) of as-prepared samples in the dark and under illumination (λ_{exc} = 435 nm, 100 mW cm^{-2}), measured in 0.1 M phosphate buffer solution (a) and 0.5 M Na_2SO_3 solution (b); charge transfer efficiency under illumination, calculated from LSV curves (c).[11]

5.3.3.2 Effect of Mo doping on the electrochemical impedance spectra (EIS)

To clarify current change from aspect of an equivalent circuit in the OER reaction, EIS measurements of BVO and Mo-BVO in the dark and under illumination were carried out. Generally, the semiconductor-electrolyte interface can be modeled as **Figure 5.9** and the equivalent circuit consists of the external circuit, space charge region and electric double layer.[31] However, it is difficult to distinguish and measure the resistance, capacitance in the space charge region and the electric double layer separately due to their similar frequency responses. Therefore, we fit EIS data by a classic Randles model, and the total capacitance and resistance are given as follows.

$$\frac{1}{C_{total}} = \frac{1}{C_{SCR}} + \frac{1}{C_{dl}} \qquad \text{(eqn. 5.2)}$$

$$R_{total} = R_{bulk} + R_{ct} \qquad \text{(eqn.5.3)}$$

Additionally, we assume that charge transfer resistance (R_{ct}) measured in Na_2SO_3 solution at 1.20 V_{RHE} approximately is zero and bulk resistance is independent of electrolyte. In this case, R_{total} equals to R_{ct}.

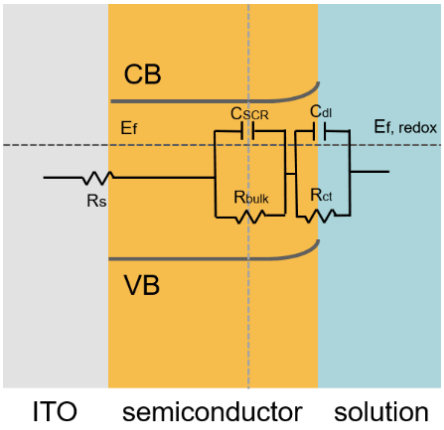

Figure 5.9 Schematic diagram of semiconductor electrolyte interface. R_s is the solution resistance between working electrode and reference electrode, R_{bulk} is bulk resistance, C_{SCR} is capacitance of space charge region, R_{ct} is charge transfer resistance, C_{dl} is capacitance of electric double layer.[11]

The detailed fitting results of the EIS data are summarized in the **Figure 5.10**, **Table 5.1**, and **Table 5.2**.

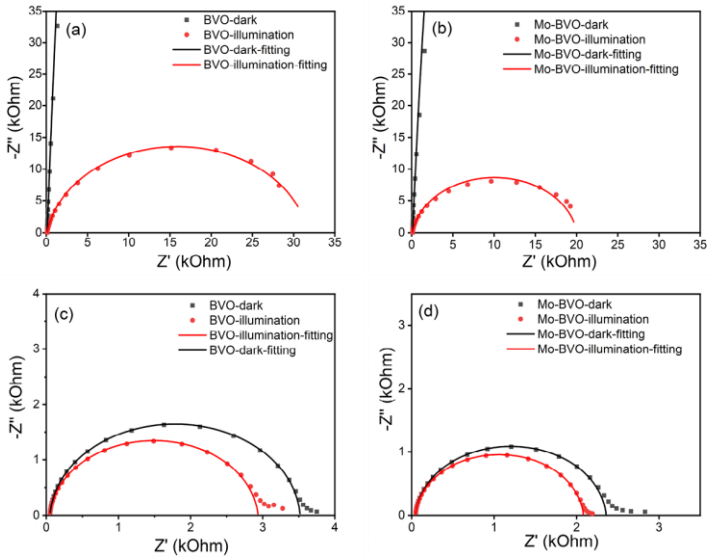

Figure 5.10 EIS fitting results of as-prepared samples, measured at 1.2 V vs. RHE in 0.1 M phosphate buffer solution (a and b) and 0.5 M Na_2SO_3 solution (c and d).[11]

Table 5.1 Element parameters of Randles equivalent circuit, obtained from EIS data fitting, measured in 0.1 M phosphate buffer solution.[11]

Sample	Condition	Rs (Ω)	CPE		$R_{total}=R_{bulk}+R_{ct}$ (MΩ)	Error(%)
			C_{total} (μF)	α		
BVO	Dark	101	3.03	0.982	12.6	1.3
	Illumination	92.9	2.85	0.904	31.6×10^{-3}	6.9
Mo-BVO	Dark	99.7	3.40	0.979	5.51	2.7
	Illumination	91.9	3.06	0.911	19.9×10^{-3}	14.1

Table 5.2 Element parameters of Randles equivalent circuit, obtained from EIS data fitting, measured in 0.5 M Na_2SO_3 solution.[11]

Sample	Condition	Rs (Ω)	CPE		$R_{total}=R_{bulk}+R_{ct}$ (kΩ)	Error (%)
			C_{total} (μF)	α		
BVO	Dark	49.6	3.17	0.967	3.47	1.0
	Illumination	47.2	2.30	0.956	2.89	2.0
Mo-BVO	Dark	45.4	3.14	0.960	2.31	1.2
	Illumination	44.7	3.21	0.958	2.06	2.0

The total resistances of BVO and Mo-BVO, measured at +1.2 V_{RHE} in 0.1 M phosphate buffer solution in the dark, are 12.6 MΩ and 5.51 MΩ, respectively. This indicates the absence of an oxidation current at 1.2 V vs. RHE, which is consistent with LSV data. Resistances of BVO and Mo-BVO sharply drop to 31.6 kΩ and 19.9 kΩ under illumination. In this case, R_{total} obviously decreases 2 - 3 orders of magnitude under illumination (**Figure 5.11a** and **5.11c**). Therefore, the current density of photoanodes, inversely proportional to R_{total}, is remarkably increased.

To further calculate the contributions of R_{bulk} and R_{ct} on the current density, EIS measurements of BVO and Mo-BVO are conducted in 0.5 M Na_2SO_3 solution at 1.2 V vs. RHE as well. R_{bulk} of BVO and Mo-BVO slightly decrease from 3.4 kΩ and 2.31 kΩ in the dark to 2.89 kΩ and 2.06 kΩ under illumination, respectively (see **Figure 5.11b** and **d**). These decreased resistances originate from increased photoconductivity under illumination.

R_{ct} of OER is thousand times higher than R_{bulk} in the dark, while R_{ct} of OER is 2.6 to 10 times higher than R_{bulk} under illumination, which means that both dark current and photocurrent densities of OER are limited by R_{ct}, rather than R_{bulk}. On the other hand, Mo doping slightly decreases R_{bulk} but obviously decreases R_{ct} under illumination, which implies that the increase of interface active sites is more important than that of bulk conductivity for photoelectrochemical OER, i.e., bulk concentration of charge carriers.

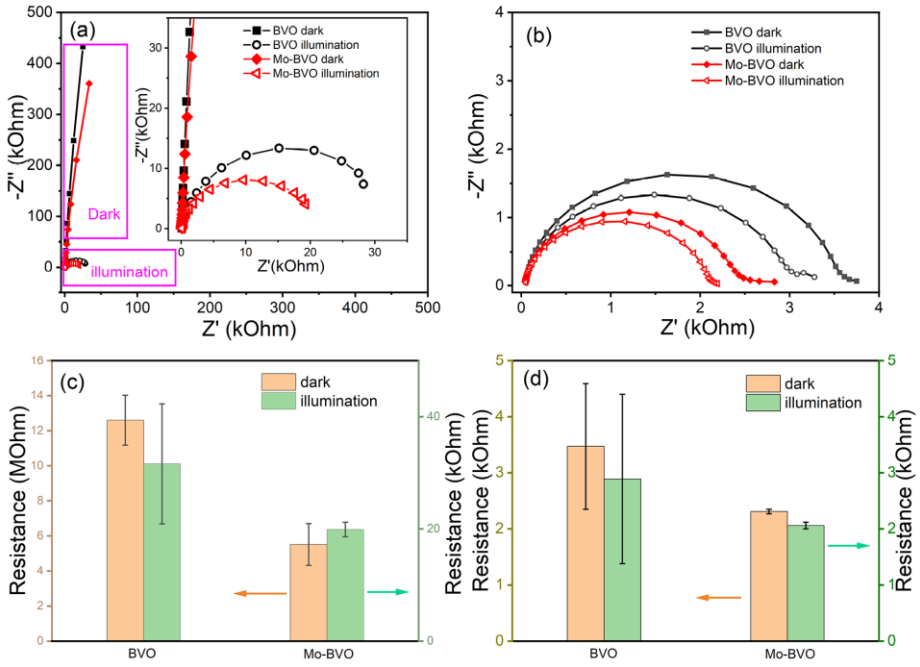

Figure 5.11 Electrochemical impedance spectra and corresponding interfacial resistances of as-prepared samples in the dark and under illumination (435 nm, 100 mW cm^{-2}), measured in 0.1 M phosphate buffer solution ((a) and (c)) and 0.5 M Na_2SO_3 solution ((b) and (d)) at the potential of 1.2 V vs. RHE. Error bars originate from repetitive measurements of second samples.[11]

5.3.3.3 Effect of Mo doping on concentration of charge carriers, photo-voltage and surface charge carrier kinetics

The Mott-Schottky measurements are carried out at the frequency of 1 kHz according to the literature.[32, 33]

In order to further confirm that the frequency of 1 kHz meet the requirement of the Mott Schottky measurements, we also plotted the resistance vs. frequency figures of $BiVO_4$ samples, measured at 1.2 V vs. RHE in the phosphate buffer solution and Na_2SO_3 solution (**Figure 5.12**). The real resistance at 1 kHz is independent of frequency and the slope of imaginary resistance at 1 kHz is close to 1, which indicates 1 kHz of frequency is suitable for Mott-Schottky measurement

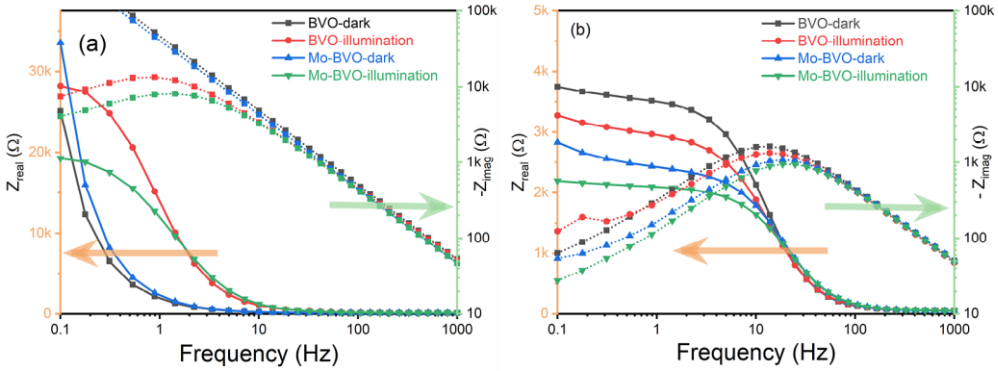

Figure 5.12 Resistance vs. frequency plots of as-prepared BVO samples, measured at 1.2 V vs. RHE in 0.1 M phosphate buffer solution (a) and 0.5 M Na_2SO_3 solution (b).[11]

Mott-Schottky plots of BVO and Mo-BVO show typical n-type semiconductor behavior as evident from the positive linear slope between 0.7 V and 1.0 V vs. RHE (**Figure 5.13**).

The concentrations of charge carriers of BVO and Mo-BVO in the dark were determined to be 1.82 × 10^{19} cm^{-3}, 2.22 × 10^{19} cm^{-3}, while the concentrations of charge carriers under illumination were increased to be 2.16 × 10^{19} cm^{-3} and 2.46 × 10^{19} cm^{-3}, according to the following equation.

$$N_D = \frac{2}{e\varepsilon_0\varepsilon_r \cdot slope \cdot A^2} \quad \text{(eqn. 5.4)}$$

N_D is the donor density, e is elementary charge, ε_0 is the dielectric constant in vacuum, ε_r is relative dielectric constant of the material. A is the actual illuminated surface area. The rise in

the charge carrier density can be interpreted as an increase of the photoconductivity and thus a reduction of the bulk resistances. The measured flat band potentials, E_{fb} of Mo-BVO, which have found to be at 0.48V, respectively, showed no changes after illumination. However, the E_{fb} of BVO shifts from 0.41 eV to 0.36 eV (**Table 5.3**). This effect is due to trapping of photo-excited holes at surface states.[38, 39]

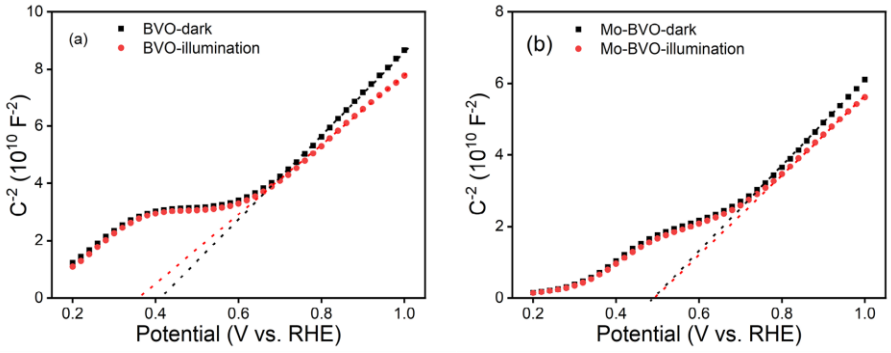

Figure 5.13 Mott Schottky plots of BVO (a) and Mo-BVO (b), measured in 0.1 M phosphate buffer solution (pH 6.8) in the dark and under illumination (435 nm, 100 mW cm^{-2}).[11]

Table 5.3 Calculated flat band potentials (E_{fb}) and concentration of charge carrier derived from Mott-Schottky plots of the as-prepared BVO samples.[11]

Sample	Condition	E_{fb} (V vs. RHE)	Concentration of charge carriers (cm^{-3})
BVO	Dark	0.41	1.82×10^{19}
	Illumination	0.36	2.16×10^{19}
Mo-BVO	Dark	0.48	2.22×10^{19}
	Illumination	0.48	2.46×10^{19}

The presence of surface defect states in the BVO sample is also demonstrated by its low photovoltage as shown in **Figure 5.14**. The photovoltages of BVO and Mo-BVO under illumination (435 nm, 100 mW cm^{-2}) are 0.063 eV, 0.216 eV, respectively. It is reported that

surface states give rise to fermi level pinning effects at the solid-electrolyte interface, which obviously limits the photovoltage.[34] Because of this, the concentration of photo-generated charge carriers in BVO is much higher than that of Mo-BVO, but the photovoltage of BVO is much lower than that of Mo-BVO (see **Figure 5.14**). Commonly, surface states in BVO arise from V vacancies, so the amount of surface states are reduced after Mo doping into V sites.[35]

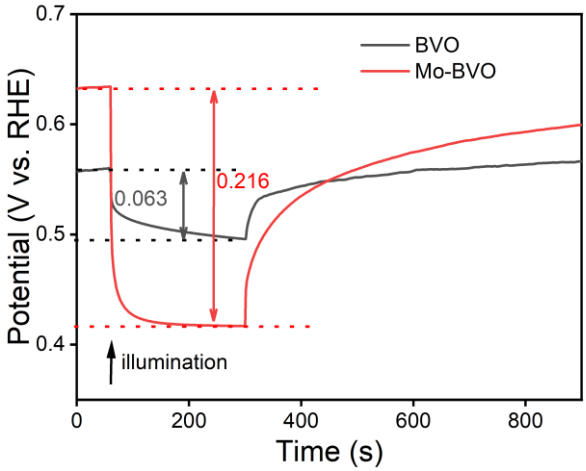

Figure 5.14 Photovoltage of as-prepared samples under illumination (435 nm, 100 mW cm^{-2}), measured at open circuit potentials in 0.1 M phosphate buffer solution.[11]

The transfer and recombination kinetics of surface charge carriers of BVO samples are investigated by intensity modulated photocurrent spectroscopy (IMPS) (**Figure 5.15**). The photocurrent can be depicted by the following equation according to Peter's model.[36]

$$j(\omega) = \frac{I_0[k_{tr}+i\omega(C_{cell}/C_{sc})]}{(k_{tr}+k_{rec}+i\omega)(1+i\omega\tau)} \quad \text{(eqn. 5.5)}$$

ω is the angular frequency of modulated light, I_0 is intensity of photo-generated holes flux towards the surface. C_{cell} is the capacitance of electrochemical cell and equal to $\frac{C_{sc}C_H}{C_{sc}+C_H}$. C_{sc} and C_H are the capacitances of space charge layer and Helmholtz layer. k_{tr} and k_{rec} are transfer rate constant and recombination rate constant of photo-generated minority charge carriers, respectively. τ is the time constant of the electrochemical cell [36, 37]

In the case that τ is at least two decades smaller than $\frac{1}{k_t+k_{rec}}$,[38] the above equation can be simplified as follows.

$$j(\omega) = \frac{I_0[k_{tr}+i\omega(C_{cell}/C_{sc})]}{(k_{tr}+k_{rec}+i\omega)} \qquad \text{(eqn. 5.6)}$$

Resistance capacitance (RC) attenuation and competition between charge carrier transfer and recombination usually occur in the 4th and 1st quadrants, respectively.[39, 40] The angular frequency corresponds to the sum of k_{tr} and k_{rec}, when the imaginary part reaches a maximum value in the 1st quadrant, i.e., $\omega_{max} = 2\pi f_{max} = k_t + k_{rec}$. When the imaginary part is equal to zero, the intercepts of the x axis correspond to $\frac{I_0 k_{tr}}{k_{tr}+k_{rec}}$ and $\frac{I_0 C_H}{C_H+C_{SC}}$, respectively. Normally, the space charge capacitance is much smaller than the Helmholtz capacitance ($C_{sc} \ll C_H$). Therefore, the ratio of the x intercepts is equal to $\frac{k_{tr}}{k_{tr}+k_{rec}}$.

At short circuit conditions, the photo-generated majority charge carriers would migrate to the back layer of the photoanode and recombine with minority charge carriers at the back contact.[41] Accordingly, the transit time of electrons reflects their recombination possibility at the back contact and can be obtained from the equation from RC attenuation region.

$$\tau = \frac{1}{2\pi f_{min}} \qquad \text{(eqn. 5.7)}$$

The calculated k_{tr} and k_{rec} of photo-excited holes and transit time of photo-generated electrons are summarized in **Table 5.4**. The average electron transit times of BVO and Mo-BVO are 0.06 ms and 0.38 ms, respectively, indicating that the photo-generated electrons in BVO transfer much faster, comparing Mo-BVO. This also implies that the PEC water splitting process is limited by the transfer of photo-excited holes, not the photo-excited electrons. The surface recombination rate of Mo-BVO is 5 times lower than that of BVO, verifying that Mo doping can reduce effectively surface recombination of BVO due to an increased amount of surface states.

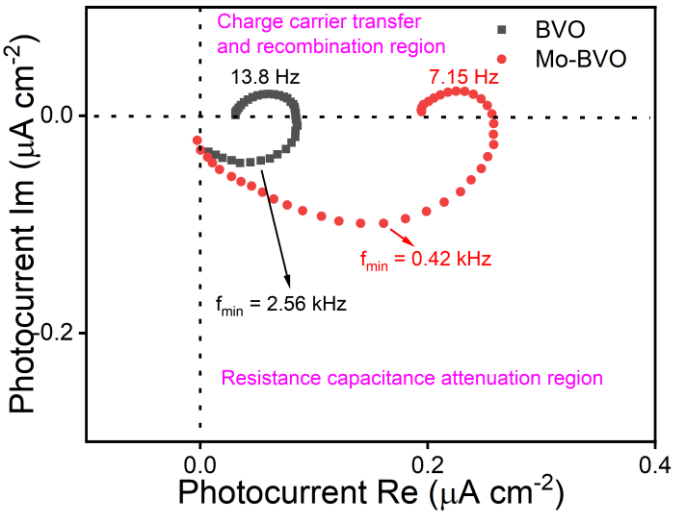

Figure 5.15 Intensity modulated photocurrent spectroscopy (IMPS) of as-prepared samples under illumination (435 nm, 100 mW cm^{-2}), measured at 1.2 V vs. RHE in 0.1 M phosphate buffer solution.[11]

Table 5.4 Calculated transfer rate constant (k_{tr}) and recombination rate constant (k_{rec}) of photo-excited holes and transit time τ of photo-generated electrons, estimated from IMPS.[11]

Sample	Transfer rate constant of charge carriers k_{tr} (s^{-1})	Recombination rate constant of charge carriers k_{rec} (s^{-1})	Transit time of electrons τ (ms)
BVO	31	55	0.06
Mo-BVO	34	11	0.38

5.4 Conclusions

To summarize, the photoelectrochemical activities of semiconductors are closely dependent on their resistance at the semiconductor electrolyte interface. In our study, Mo doping of BVO films was introduced by a spin coating approach. Mo doping are confirmed by XPS and Raman

spectra. The influence of Mo doping on BVO is investigated from the aspect of interfacial resistance and charge carrier transfer. Our results show: (1) interfacial charge transfer resistances (R_{ct}) of $BiVO_4$ in 0.1 M phosphate buffer solution decrease 2 to 3 orders of magnitude under illumination. (2) both dark and photo current densities of BVO in OER are dominantly limited by R_{ct}, rather than R_{bulk}; (3) Mo doping of BVO can not only effectively decrease charge transfer resistance (R_{ct}) under illumination, but also increase photovoltage; (4) in comparison with bare BVO, Mo doped BVO exhibits an enhanced photocurrent density at 1.23 V vs. RHE by a factor of 2.7.

References

[1] M.A. Marwat, M. Humayun, M.W. Afridi, H. Zhang, M.R. Abdul Karim, M. Ashtar, M. Usman, S. Waqar, H. Ullah, C. Wang, W. Luo, Advanced Catalysts for Photoelectrochemical Water Splitting, *ACS Appl. Energy Mater.*, **2021**, *4*, 12007-12031.

[2] F. Le Formal, E. Pastor, S.D. Tilley, C.A. Mesa, S.R. Pendlebury, M. Gratzel, J.R. Durrant, Rate law analysis of water oxidation on a hematite surface, *J. Am. Chem. Soc.*, **2015**, *137*, 6629-6637.

[3] J. Tang, J.R. Durrant, D.R. Klug, Mechanism of Photocatalytic Water Splitting in TiO_2. Reaction of Water with Photoholes, Importance of Charge Carrier Dynamics, and Evidence for Four-Hole Chemistry, *J. Am. Chem. Soc.*, **2008**, *130*, 13885-13891.

[4] K.T. Butler, B.J. Dringoli, L. Zhou, P.M. Rao, A. Walsh, L.V. Titova, Ultrafast carrier dynamics in $BiVO_4$ thin film photoanode material: interplay between free carriers, trapped carriers and low-frequency lattice vibrations, *J. Mater. Chem. A*, **2016**, *4*, 18516-18523.

[5] F.F. Abdi, T.J. Savenije, M.M. May, B. Dam, R. van de Krol, The Origin of Slow Carrier Transport in $BiVO_4$ Thin Film Photoanodes: A Time-Resolved Microwave Conductivity Study, *J. Phys. Chem. Lett.*, **2013**, *4*, 2752-2757.

[6] A.J. Rettie, H.C. Lee, L.G. Marshall, J.F. Lin, C. Capan, J. Lindemuth, J.S. McCloy, J. Zhou, A.J. Bard, C.B. Mullins, Combined charge carrier transport and photoelectrochemical characterization of $BiVO_4$ single crystals: intrinsic behavior of a complex metal oxide, *J. Am. Chem. Soc.*, **2013**, *135*, 11389-11396.

[7] J.H. Kim, J.S. Lee, Elaborately Modified $BiVO_4$ Photoanodes for Solar Water Splitting, *Adv. Mater.*, **2019**, *31*, 1806938.

[8] F.F. Abdi, L. Han, A.H. Smets, M. Zeman, B. Dam, R. van de Krol, Efficient solar water splitting by enhanced charge separation in a bismuth vanadate-silicon tandem photoelectrode, *Nat. Commun.*, **2013**, *4*, 2195.

[9] M. Schleuning, M. Kölbach, F.F. Abdi, K. Schwarzburg, M. Stolterfoht, R. Eichberger, R. van de Krol, D. Friedrich, H. Hempel, Generalized Method to Extract Carrier Diffusion

Length from Photoconductivity Transients: Cases of $BiVO_4$, Halide Perovskites, and Amorphous and Crystalline Silicon, *PRX Energy*, **2022**, *1*, 023008.

[10] F.F. Abdi, R. van de Krol, Nature and Light Dependence of Bulk Recombination in Co-Pi-Catalyzed $BiVO_4$ Photoanodes, *J. Phys. Chem. C*, **2012**, *116*, 9398-9404.

[11] X. Wu, F.E. Oropeza, Z. Qi, M. Einert, C. Tian, C. Maheu, K. Lv, J.P. Hofmann, Influence of Mo doping on interfacial charge carrier dynamics in photoelectrochemical water oxidation on $BiVO_4$, *Sustain. Energy Fuels*, **2023**, *7*, 2923-2933.

[12] M.V. Malashchonak, E.A. Streltsov, D.A. Kuliomin, A.I. Kulak, A.V. Mazanik, Monoclinic bismuth vanadate band gap determination by photoelectrochemical spectroscopy, *Mater. Chem. Phys.*, **2017**, *201*, 189-193.

[13] J.K. Cooper, S. Gul, F.M. Toma, L. Chen, P.-A. Glans, J. Guo, J.W. Ager, J. Yano, I.D. Sharp, Electronic Structure of Monoclinic $BiVO_4$, *Chem. Mater.*, **2014**, *26*, 5365-5373.

[14] J.K. Cooper, S. Gul, F.M. Toma, L. Chen, Y.-S. Liu, J. Guo, J.W. Ager, J. Yano, I.D. Sharp, Indirect Bandgap and Optical Properties of Monoclinic Bismuth Vanadate, *J. Phys. Chem. C*, **2015**, *119*, 2969-2974.

[15] Y. Wei, J. Su, X. Wan, L. Guo, L. Vayssieres, Spontaneous photoelectric field-enhancement effect prompts the low cost hierarchical growth of highly ordered heteronanostructures for solar water splitting, *Nano Res.*, **2016**, *9*, 1561-1569.

[16] T. Jiang, F. Nan, J. Zhou, Enhanced photocatalytic and photoelectrochemical performance of g-C_3N_4/$BiVO_4$ heterojunction: A combined experimental and theoretical study, *AIP Adv.*, **2019**, *9*, 055225.

[17] Z. Jiang, Y. Liu, T. Jing, B. Huang, X. Zhang, X. Qin, Y. Dai, M.-H. Whangbo, Enhancing the Photocatalytic Activity of $BiVO_4$ for Oxygen Evolution by Ce Doping: Ce^{3+} Ions as Hole Traps, *J. Phys. Chem. C*, **2016**, *120*, 2058-2063.

[18] Y. Zhou, L. Zhang, L. Lin, B.R. Wygant, Y. Liu, Y. Zhu, Y. Zheng, C.B. Mullins, Y. Zhao, X. Zhang, G. Yu, Highly Efficient Photoelectrochemical Water Splitting from Hierarchical WO_3/$BiVO_4$ Nanoporous Sphere Arrays, *Nano Lett.*, **2017**, *17*, 8012-8017.

[19] S. Wang, P. Chen, Y. Bai, J.H. Yun, G. Liu, L. Wang, New $BiVO_4$ Dual Photoanodes with Enriched Oxygen Vacancies for Efficient Solar-Driven Water Splitting, *Adv. Mater.*, **2018**, *30*, 1800486.

[20] W. Ji, R. Shen, R. Yang, G. Yu, X. Guo, L. Peng, W. Ding, Partially nitrided molybdenum trioxide with promoted performance as an anode material for lithium-ion batteries, *J. Mater. Chem. A*, **2014**, *2*, 699-704.

[21] S. Durairaj, P. Krishnamoorthy, N. Raveendran, B.D. Ryu, C.-H. Hong, T.H. Seo, S. Chandramohan, Barrier-assisted vapor phase CVD of large-area MoS_2 monolayers with high spatial homogeneity, *Nanoscale Adv.*, **2020**, *2*, 4106-4116.

[22] J. Feng, W. Bao, L. Li, H. Cheng, W. Huang, H. Kong, Y. Li, The synergistic effect of nitrogen-doped titanium dioxide/mercaptobenzoic acid/silver nanocomplexes for surface-enhanced Raman scattering, *J. Nanopart. Res.*, **2018**, *20*, 82.

[23] S.H. Brewer, S. Franzen, Optical properties of indium tin oxide and fluorine-doped tin oxide surfaces: correlation of reflectivity, skin depth, and plasmon frequency with conductivity, *J. Alloys Compd.*, **2002**, *338*, 73–79.

[24] Rong Lu, Wei Gan, Bao-hua Wu, Zhen Zhang, Yuan Guo, H.-f. Wang, C-H Stretching Vibrations of Methyl, Methylene and Methine Groups at the Vapor/Alcohol (n=1-8) Interfaces, *J. Phys. Chem. B*, **2005**, *109*, 14118-14129.

[25] V.-I. Merupo, S. Velumani, K. Ordon, N. Errien, J. Szade, A.-H. Kassiba, Structural and optical characterization of ball-milled copper-doped bismuth vanadium oxide ($BiVO_4$), *CrystEngComm*, **2015**, *17*, 3366-3375.

[26] M.R.d.S. Pelissari, N.F. Azevedo Neto, L.P. Camargo, L.H. Dall'Antonia, Characterization and Photo-Induced Electrocatalytic Evaluation for $BiVO_4$ Films Obtained by the SILAR Process, *Electrocatalysis*, **2021**, *12*, 211-224.

[27] W. Luo, J. Wang, X. Zhao, Z. Zhao, Z. Li, Z. Zou, Formation energy and photoelectrochemical properties of $BiVO_4$ after doping at Bi^{3+} or V^{5+} sites with higher valence metal ions, *Phys. Chem. Chem. Phys.*, **2013**, *15*, 1006-1013.

[28] X. Zhao, W. Luo, J. Feng, M. Li, Z. Li, T. Yu, Z. Zou, Quantitative Analysis and Visualized Evidence for High Charge Separation Efficiency in a Solid-Liquid Bulk Heterojunction, *Adv. Energy Mater.*, **2014**, *4*, 1301785.

[29] K.J. McDonald, K.-S. Choi, A new electrochemical synthesis route for a BiOI electrode and its conversion to a highly efficient porous $BiVO_4$ photoanode for solar water oxidation, *Energy Environ. Sci*, **2012**, *5*, 8553-8557.

[30] J. Gu, Q. Huang, Y. Yuan, K.-H. Ye, Z. Wang, W. Mai, In situ growth of a TiO_2 layer on a flexible Ti substrate targeting the interface recombination issue of $BiVO_4$ photoanodes for efficient solar water splitting, *J. Mater. Chem. A*, **2017**, *5*, 20195-20201.

[31] X. Wan, F. Niu, J. Su, L. Guo, Enhanced photoelectrochemical water oxidation of bismuth vanadate via a combined strategy of W doping and surface RGO modification, *Phys. Chem. Chem. Phys.*, **2016**, *18*, 31803-31810.

[32] Q. Meng, B. Zhang, L. Fan, H. Liu, M. Valvo, K. Edstrçm, M. Cuartero, R.d. Marco, G.A. Crespo, L. Sun, Efficient $BiVO_4$ Photoanodes by Postsynthetic Treatment: Remarkable Improvements in Photoelectrochemical Performance from Facile Borate Modification, *Angew. Chem. Int. Ed.*, **2021**, *131*, 19203-19209.

[33] T. Tran-Phu, Z. Fusco, I. Di Bernardo, J. Lipton-Duffin, C.Y. Toe, R. Daiyan, T. Gengenbach, C.-H. Lin, R. Bo, H.T. Nguyen, G.M.J. Barca, T. Wu, H. Chen, R. Amal, A. Tricoli, Understanding the Role of Vanadium Vacancies in $BiVO_4$ for Efficient Photoelectrochemical Water Oxidation, *Chem. Mater.*, **2021**, *33*, 3553-3565.

[34] B.J. Trześniewski, W.A. Smith, Photocharged $BiVO_4$ photoanodes for improved solar water splitting, *J. Mater. Chem. A*, **2016**, *4*, 2919-2926.

[35] M. Lamers, S. Fiechter, D. Friedrich, F.F. Abdi, R. van de Krol, Formation and suppression of defects during heat treatment of $BiVO_4$ photoanodes for solar water splitting, *J. Mater. Chem. A*, **2018**, *6*, 18694-18700.

[36] E.A. Ponomarev, L.M. Peter, A generalized theory of intensity modulated photocurrent spectroscopy (IMPS), *J. Electroanal. Chem.*, **1995**, *396*, 219-226.

[37] M. Antuch, P. Millet, A. Iwase, A. Kudo, The role of surface states during photocurrent switching: Intensity modulated photocurrent spectroscopy analysis of $BiVO_4$ photoelectrodes, *Appl. Catal. B: Environ.*, **2018**, *237*, 401-408.

[38] H. Cachet, E.M.M. Sutter, Kinetics of water oxidation at TiO_2 nanotube arrays at different pH domains investigated by electrochemical and light-modulated impedance spectroscopy, *J. Phys. Chem. C*, **2015**, *119*, 25548-25558.

[39] F. Li, H. Yang, Q. Zhuo, D. Zhou, X. Wu, P. Zhang, Z. Yao, L. Sun, A cobalt@cucurbit[5]uril complex as a highly efficient supra-molecular catalyst for electrochemical and photoelectrochemical water splitting, *Angew. Chem. Int. Ed.*, **2021**, *60*, 1976-1985.

[40] B. Gao, T. Wang, X. Fan, H. Gong, P. Li, Y. Feng, X. Huang, J. He, J. Ye, Enhanced water oxidation reaction kinetics on a $BiVO_4$ photoanode by surface modification with Ni_4O_4 cubane, *J. Mater. Chem. A*, **2019**, *7*, 278-288.

[41] L. Xia, J. Li, J. Bai, L. Li, Q. Zeng, Q. Xu, B. Zhou, Preparation of a $BiVO_4$ nanoporous photoanode based on peroxovanadate reduction and conversion for efficient photoelectrochemical performance, *Nanoscale*, **2018**, *10*, 2848-2855.

6. Promoting effect of interfacial hole accumulation on photoelectrochemical water oxidation in $BiVO_4$ and Mo doped $BiVO_4$ [3]

Hole transfer at the semiconductor-electrolyte interface is a key elementary process in (photo)electrochemical (PEC) water oxidation. However, up to now, a detailed understanding of the hole transfer and the influence of surface hole density on PEC water oxidation kinetics is lacking. In this work, we propose a model for the first time in which the surface accumulated hole density in $BiVO_4$ and Mo-doped $BiVO_4$ samples during water oxidation can be acquired via employing illumination-dependent Mott-Schottky measurements. Based on this model, some results are demonstrated as below: (1) Although the surface hole density increases when increasing light intensity and applied potential, the hole transfer rate remains linearly proportional to surface hole density on a log-log scale. (2) Both water oxidation on $BiVO_4$ and Mo-doped $BiVO_4$ follow first-order reaction kinetics at low surface hole densities, which is in good agreement with literature. (3) We find that water oxidation active sites in both $BiVO_4$ and Mo-doped $BiVO_4$ are very likely to be Bi^{5+}, which are produced by photoexcited or/and electro-induced surface holes, rather than VO_x species or Mo^{6+} due to their insufficient redox potential for water oxidation. (4) Introduction of Mo doping brings about higher OER activity of $BiVO_4$, as it suppresses the recombination rate of surface holes and increases formation of Bi^{5+}. This surface hole model offers a general approach for the quantification of surface hole density in the field of semiconductor photoelectrocatalysis.

6.1 Introduction

Photoelectrochemical water splitting offers a promising approach to convert solar energy to chemical energy.[1, 2] In comparison with the cathodic hydrogen evolution reaction, photoanodic oxygen evolution is much more sluggish due to slow hole kinetics in the rate limiting step during water oxidation (oxygen evolution reaction, OER).

[3] This chapter has been published in: **Xiaofeng Wu,** Freddy E. Oropeza, Shixin Chang, Marcus Einert, Qingyang Wu, Clément Maheu, Julia Gallenberger, Chuanmu Tian, Kangle Lv, Jan P. Hofmann, Promoting effect of interfacial hole accumulation on photoelectrochemical water oxidation in $BiVO_4$ and Mo doped $BiVO_4$, *Advanced Powder Materials*, doi.org/10.1016/j.apmate.2024.100234.

Loading of OER cocatalysts (e.g., RuO_2, MnO_2, CoO_x, NiO_x) on a photoabsorber is a general approach to speed up interfacial hole transfer, as electrocatalysts can lower the required overpotential for water oxidation significantly. For instance, Sun et al. reported that a Cu@cucurbit[5]uril cocatalyst on a $BiVO_4$ photoanode can lower the onset potential from 0.50 to 0.15 V vs. RHE and remarkably increase the photocurrent from 2.0 to 4.8 mA cm^{-2} at 1.23 V vs. RHE under illumination (AM 1.5G, 100 mW cm^{-2}).[3]

Nowadays, significant efforts are dedicated to promoting the efficiency of photoelectrodes in water oxidation by tuning light absorption, separation of charge carriers and interfacial chemical reaction. Studies of charge carrier dynamics are relatively rare, especially the determination of interfacial charge carrier concentration. At present, transient absorption spectroscopy (TAS) is the major technique to probe and determine photo-induced surface hole density in semiconductors.[4-7] Based on this technique, new insight into the carrier dynamics and reaction kinetics at the semiconductor solid-liquid interface has been obtained. For example, Formal et al. demonstrated that the reaction order of water oxidation on Fe_2O_3 hematite and $BiVO_4$ is closely linked to the surface hole density. First order reaction and third order reaction of water oxidation are revealed at low and high surface accumulated hole density, respectively.[8, 9]

Apart from TAS, it is worth mentioning that Li et al. recently developed an operando surface potential approach to investigate the relationship between interfacial hole transfer rate and surface potential in the photoelectrochemical water oxidation process. They demonstrated that the surface potential is linearly correlated to the interfacial charge transfer rate of water oxidation and this linear relation is independent of applied bias and light intensity.[10]

Despite these efforts, the complex relationship between surface hole density, applied bias, (photo)electrochemically active sites and (photo)current density is not clearly established yet. In this work, we setup a surface hole accumulation model for semiconductor-electrolyte interfaces with which the surface accumulated hole density can be determined. $BiVO_4$ and Mo doped $BiVO_4$ are employed as model systems for studying the interplay between surface hole density and photocurrent. Water oxidation on these model systems follows a first order reaction mechanism, which is in good agreement with results from TAS literature. Besides, we identify the active sites of Mo doped $BiVO_4$ being Bi^{5+}, rather than VO_x or Mo^{6+} species via the analysis of redox potentials. The observed

promoting effect of Mo doping for water oxidation mainly originates from a reduced recombination rate.

6.2 Experimental section

6.2.1 Preparation of $BiVO_4$ and Mo doped $BiVO_4$ photoanodes

The synthesis procedure of $BiVO_4$ and Mo doped $BiVO_4$ films follows our previous work.[11] Briefly, ITO substrates (2×2 cm^2, 10 Ω per square, Xop glass) were cleaned by ultrasound in distilled water, acetone, and ethanol and UV/ozone treatment for further use. The recipes of $BiVO_4$ precursor solution was displayed as follows: 1 mmol of $Bi(NO_3)_3{\cdot}5H_2O$ (99.99%, Sigma-Aldrich) in 4 mL of 2-methoxyethanol (99.5%, Carl Roth) and 1 mmol of vanadyl-acetylacetonate (98%, Sigma-Aldrich) in 4 mL of methanol form a colorless bismuth source solution and a dark blue V source solution, respectively. Subsequently, the dark blue V source solution was dropped into the Bi-containing solution, followed by addition of 0.5 mL of acetylacetone (99%, Sigma-Aldrich) for tuning the viscosity. Finally, 50 µL of the clear combined precursor solution was spread homogeneously on the ITO substrates by spin coating at the speed of 1800 rpm for 1 min. After that, the samples were transferred to a muffle furnace and calcined at 470 °C for 4 h in air with a ramp rate of 2 °C min^{-1}. For the preparation of Mo doped $BiVO_4$ samples, a certain amount of bis(acetylacetonato) dioxomolybdenum (VI) (99 %, Sigma-Aldrich) was added to the V precursor solution. The stoichiometric molar ratio of V to Mo compounds is 0.97: 0.03. The other procedures are the same as for the bare $BiVO_4$. The finally collected samples were named BVO and Mo-BVO.

6.2.2 Materials characterization

XRD patterns were measured from 2θ = 5° to 80° on a D8 Advance diffractometer (Bruker, Germany) with monochromatic Cu Kα radiation at a scan rate of 0.02° min^{-1}. The morphologies of as-prepared BVO samples were investigated by field emission scanning electron microscopy (FE-SEM, SU8010, Hitachi). UV-Vis-NIR spectra were carried out on a Cary 7000 universal measurement spectrometer (Agilent Technologies, Santa Clara, USA). Baseline correction of air was conducted before the measurements. X-ray photoelectron spectra (XPS) of samples were acquired on a Thermo Fisher Escalab 250 with a monochromic Al Kα X-ray source (hν= 1486.6 eV, 13 mA, 15 kV), measured in an analytical chamber with

a base pressure below 5×10^{-9} mbar. The pass energy, energy step length and dwell time were set to 10 eV, 0.05 eV, 50 ms, respectively. Subsequently, the high-resolution XPS spectra of as-prepared samples were recorded. An electron gun was used to compensate for surface charging and all XPS spectra were binding energy calibrated by setting the main peak of the C 1*s* spectrum to 284.8 eV (assigned to sp^3 C). The XPS spectra were analyzed with CasaXPS (version 2.3.19PR1.0) [2], using Shirley-type background, the weighted least-squares method and model curves (70% Gaussian and 30% Lorentzian). Work function and valence band edge positions were determined by He-I (21.22 eV) ultraviolet photoelectron spectroscopy (UPS) on the same spectrometer. 2.5×10^{-8} mbar of He was introduced and pass energy, step length and dwell time were set to 2.5 eV, 0.05 eV, 100 ms, respectively. To estimate the secondary electron cutoff energy, a −6 V bias was applied to impart additional kinetic energy and have a more resolved portion of this spectrum. Raman spectroscopy was performed on a Bruker SENTERRA microscope with a green excitation laser (532 nm). The spectra were collected by averaging 5 scans with a step length of 2 cm^{-1}.

6.2.3 Photoelectrochemical measurements

All photoelectrochemical characterization was carried out in 0.1 M sodium phosphate buffer solution (KPi, pH 6.8) in a standard three electrode configuration (PECC-2 cell Zahner Elektrik GmbH, Germany). The BVO film samples were used as working electrode with an active irradiation area of 0.283 cm^2. Pt wire was used as counter electrode (CE) and Ag/AgCl electrode was used as reference electrode (RE). Linear sweep voltammetry curves of as-prepared BVO samples were acquired from +0.2 VRHE to +1.5 VRHE at a scan rate of 2 mV and 10 mV. Mott Schottky plots were performed from +0.2 V to +1.4 V at a frequency of 1 kHz in the dark or under illumination. The intensity of the LED light source (λ_{center} = 435 nm; $h\nu_{center}$ = 2.85 eV) was varied from 10 to 200 mW cm^{-2}.

6.3 Results and discussion

6.3.1 Crystalline phase, microstructure and optical properties

XRD patterns of as-synthesized BVO and Mo-BVO samples are shown in **Figure 6.1**. The characteristic diffraction peaks showed up at 2θ = 18.7°, 18.9°, 28.9°, and 30.4° which are

assigned to (110), (011), (121), and (040) crystal facets of monoclinic $BiVO_4$, respectively (JCPDS No. 14-0688). No impurity phases in BVO and Mo-BVO samples were observed. The phase purity of $BiVO_4$ can be further evidenced by their Raman spectra (see **Figure 6.5** and discussion below) since this technique is much more sensitive to detection of secondary phases. The peak of the (121) crystalline facet in BVO shifts from 2θ = 29.01° to 28.94° after doping, which indicates a change in the lattice parameter, and thus a successful substitution of Mo ions. These data are supported by the Raman as well as XPS analysis (see **Figure 6.4e** and discussion below). Typical wormlike morphologies of bare BVO and Mo-BVO samples are shown in **Figure 6.2a** and **Figure 6.2c**. The widths of these wormlike chains in BVO and Mo-BVO are roughly 150-200 nm and 50-100 nm, respectively. The small porous channel of Mo-BVO implied that Mo doping probably influences the crystal growth of $BiVO_4$. The thicknesses of both BVO and Mo-BVO was found to be about 400 nm (**Figure 6.2b** and **Figure 6.2d**), investigated by cross-sectional SEM analysis and consistent with our previous work.[11]

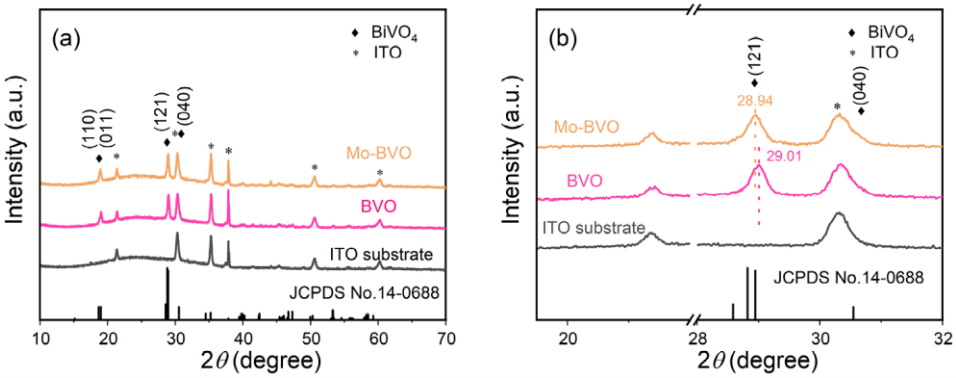

Figure 6.1 XRD pattern (a) of as-synthesized BVO and Mo-BVO samples and corresponding local enlarged region (b) of (121) crystal facet in BVO and Mo-BVO samples.

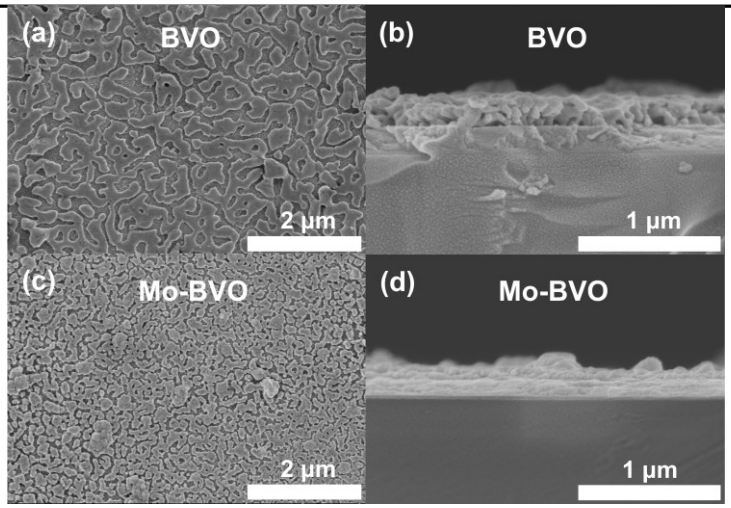

Figure 6.2 SEM images of BVO (a), Mo-BVO (c) and their cross-section views of BVO (b) and Mo-BVO (d) samples.

UV-Vis-NIR absorption spectra were collected to investigate the light-harvesting abilities of as-synthesized BVO samples (**Figure 6.3a**). A bare ITO substrate shows an optical absorption onset at the transition energy of 2.5 eV and therefore does not influence the bandgap determinations of BVO and Mo-BVO samples. Intrinsic $BiVO_4$ is considered as an indirect semiconductor with an optical bandgap of 2.4 eV. However, the direct optical bandgap of $BiVO_4$ is only 200 meV higher than its indirect optical bandgap, which leads to a high visible light absorption coefficient (~ 10^7 m^{-1}).[11, 12] The direct bandgaps of BVO and Mo-BVO samples were determined by Tauc plot analysis to 2.45 eV and 2.56 eV, respectively. The result indicates that the optical bandgap of BVO barely changed after Mo doping.

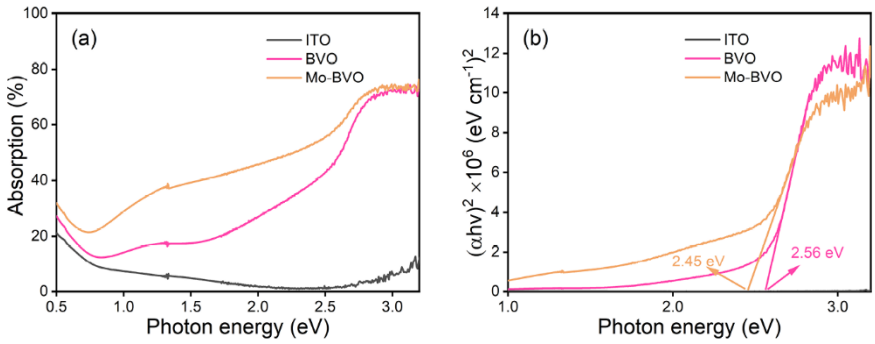

Figure 6.3 UV-Vis-NIR absorption spectra (a) and corresponding Tauc plots (b) of ITO substrates, BVO, and Mo-BVO samples, assuming direct optical absorption.

6.3.2 Analysis of valence states and surface species

X-ray photoemission spectroscopy (XPS) was performed to analyze Mo doping, valence states and surface species of the BVO samples. The emission lines at binding energies 159.0 eV and 164.4 eV are attributed to Bi $4f_{7/2}$ and Bi $4f_{5/2}$ (**Figure 6.4a**).[13] The two emission lines of 524.2 eV and 516.6 eV can be ascribed to V $2p_{1/2}$ and V $2p_{3/2}$, respectively (**Figure 6.4b**).[14] The spin-orbit splitting energy of the Bi 4*f* orbitals is 5.4 eV, while that of V 3*d* orbitals is 7.6 eV.[15] The O1*s* peaks at 529.7 eV, 530.3 eV, and 532.4 eV are usually assigned to lattice oxygen, surface hydroxyl groups and adsorbed oxygen species, respectively.[16, 17] The Mo $3d_{3/2}$ and $3d_{5/2}$ states at 235.3 eV and 232.2 eV indicate the successful introduction of Mo^{6+} ions into $BiVO_4$ in Mo-BVO (**Figure 6.4e**).[18, 19] Additionally, N species cannot be observed for both BVO and Mo-BVO samples, which implies that the $Bi(NO_3)_3{\cdot}5H_2O$ precursor has been completely thermally decomposed (**Figure 4d**). The C 1*s* region can be fitted by three peaks at 288.3 eV, 286.2 eV, and 284.8 eV, corresponding to C=O, C-O-C and C-C (sp^3) species, respectively. The carbon signals originate from surface adsorbed hydrocarbons, typically observed at sol-gel derived metal oxide thin films.[20]

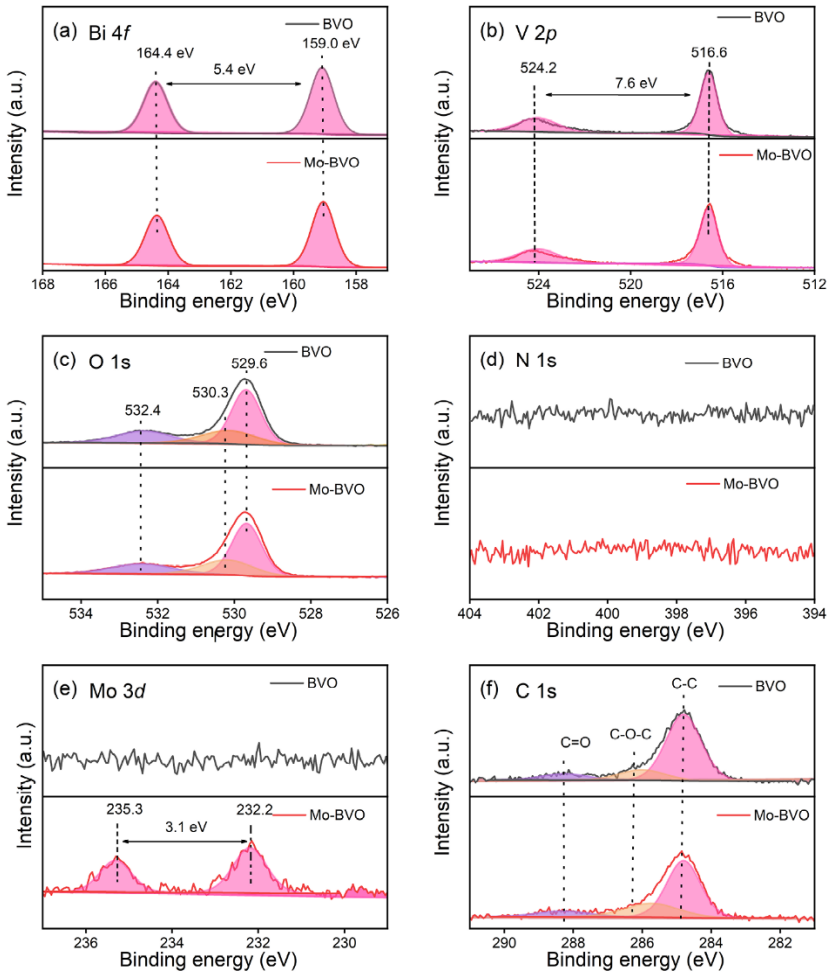

Figure 6.4 High resolution XPS spectra of BVO and Mo-BVO samples: Bi 4*f* (a), V 2*p* (b), O 1*s* (c), N 1*s* (d), Mo 3*d* (e), and C 1*s* (f) spectral regions.

The phase composition at the surface of BVO and Mo-BVO samples has been additionally confirmed by Raman spectroscopy. As shown in **Figure 6.5**, the bands located at around 210, 328, 367, 712, and 820 cm^{-1} are assigned to typical characteristic phonon peaks of monoclinic $BiVO_4$.[21, 22] The band at around 210 cm^{-1} originates from the external vibration mode of VO_4^{3-} group. In comparison with internal modes, the frequencies of the external mode in VO_4^{3-} group are usually much lower owning to heavier mass.[23] The Raman bands at 367 cm^{-1} and 328 cm^{-1} are the symmetric and asymmetric bending vibration of the VO_4^{3-} group, respectively. The peaks at around 820 cm^{-1} and 712 cm^{-1} can be assigned to symmetric and asymmetric stretching vibration of the V-O bonds.[11] Symmetric stretching vibration of V-O stemming from the VO_4^{3-} group shifts from 824.8 cm^{-1} to 820.0 cm^{-1}, which implies the substitution of Mo ions on V sites in $BiVO_4$.[24]

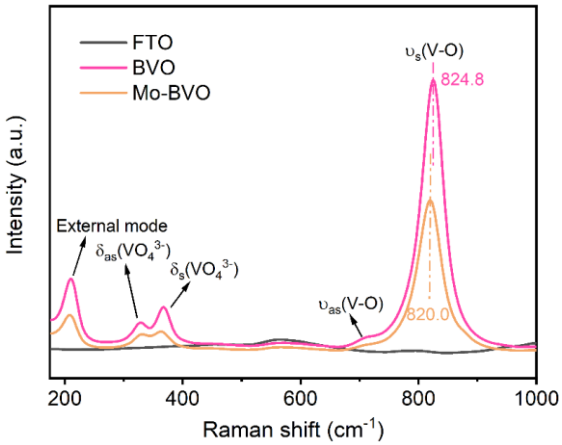

Figure 6.5 Raman spectra (532 nm excitation) of BVO (pink) and Mo-BVO (light brown) films, FTO substrates (black) were measured as reference.

6.3.3 Photoelectrochemical measurements

6.3.3.1 Surface hole states on BVO and Mo-BVO

In an ideal semiconductor without surface states, holes can only be thermally excited from the valence band in the dark, as no electronic states are available in the band gap.[25] However, in a real semiconductor, various surface states including surface defects, dangling bonds and absorbed species exist. These surface states forming mid-gap states in the semiconductor can store and release charge carriers and are generally regarded as recombination centers or active sites for surface chemical reactions.

At the surface of photoelectrodes, photo-induced or/and electro-induced holes are mainly localized at specific sites like surface states or states close to the valence band maximum.[25] The chemical speciation of these holes can be expressed as follows, where M denotes a transition metal:[26]

$$\mathrm{M(III)-OH+h^+ \rightarrow M(IV)-OH \rightleftharpoons M(III)-O^{\cdot}+H^+} \quad \text{(eqn. 6.1)}$$

Lower valence states of transition metals can be oxidized to higher valence states by photo and/or electro induced holes. Generally, hydroxyl groups exist at the surface of oxide semiconductors when exposed to air or aqueous electrolyte. These adsorbed hydroxyl groups and water can be oxidized when the redox potential of the high valence-state metal ions is high enough to overcome the required energy barriers of the charge transfer steps.

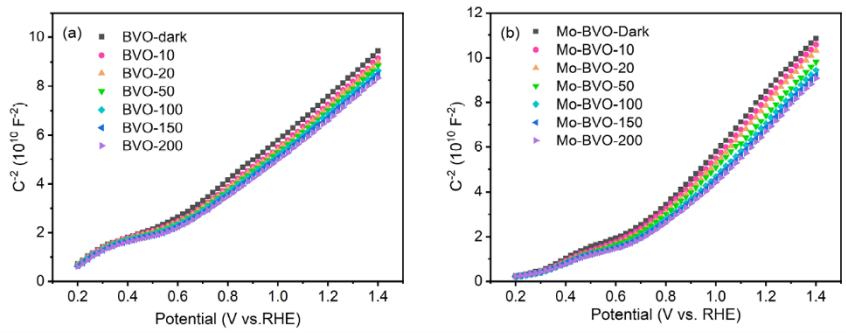

Figure 6.6 Mott-Schottky characterization of BVO (a) and Mo-BVO (b) samples, measured in 0.1 M phosphate buffer solution (pH 6.8) in the dark and under illumination. The wavelength of the light source is 435 nm and its intensity varies from 10 to 200 mW cm^{-2} (value given as (Mo-)BVO-XX in legend).

To investigate the impact of light illumination on the charge carrier concentration of BVO and Mo-BVO samples, Mott-Schottky measurements of as-prepared samples are carried out under dark and different intensities of light irradiation (**Figure 6.6**). Consistently, the slopes of the Mott-Schottky plots in both BVO and Mo-BVO samples decrease with increasing light intensity, which indicates an increased concentration of photo-generated charge carriers within the space charge region. Compared to the bulk charge carrier concentrations in BVO and Mo-BVO samples in the dark, the estimated photogenerated charge carrier concentration in BVO and Mo-BVO samples are 6.5× 10^{18} cm^{-3} and 8.5× 10^{18} cm^{-3}, which correspond to 8.8% and 16.6% of the bulk charge carrier concentration measured by Mott-Schottky in the dark, respectively. The concentration of charge carriers and the flat band positions are summarized in **Table 6.1**.

Table 6.1 Positions of flat band potentials (E_{fb}) and concentrations of charge carriers in the dark and under illumination, estimated from the Mott–Schottky plots of the as-prepared BVO and Mo-BVO samples.

Sample	Illumination intensity (mW cm^{-2})	E_{fb} (V vs. RHE)	Concentration of charge carriers (10^{19} cm^{-3})

BVO	0 (dark)	0.36	7.38
	10	0.36	7.42
	20	0.36	7.51
	50	0.36	7.64
	100	0.36	7.80
	150	0.36	7.91
	200	0.36	8.03
Mo-BVO	0 (dark)	0.53	5.12
	10	0.53	5.20
	20	0.53	5.27
	50	0.53	5.66
	100	0.53	5.72
	150	0.53	5.87
	200	0.53	5.97

To obtain the surface accumulated photoexcited hole density p_s (cm^{-2}), a surface hole model is proposed (see 6.3.3.2). Based on this model, the surface hole density p_S can be expressed by the following equation.

$$p_s = \frac{1}{e\,A_c}\left(\sqrt{\frac{U-U'_{fb}}{slope'}} - \sqrt{\frac{U-U_{fb}}{slope}}\right) \quad \text{(eqn. 6.2)}$$

Slope' and slope are the slopes of Mott Schottky plot under illumination and in the dark, respectively. U'_{fb} and U_{fb} is the flat band position under illumination and in the dark, respectively.

The surface hole density vs. potential curves of as-prepared BVO samples is shown in **Figure 6.7**. The surface accumulated photoexcited charge carrier density in BVO and Mo-BVO samples increase when increasing applied potentials and light intensities. The highest surface accumulated hole densities of BVO and Mo-BVO film samples at the potential of 1.23 V (vs. RHE) under illumination (435 nm, 200 mW cm^{-2}) can achieve 1.7 × 10^{12} cm^{-2} and 4.0 × 10^{12} cm^{-2}, respectively.

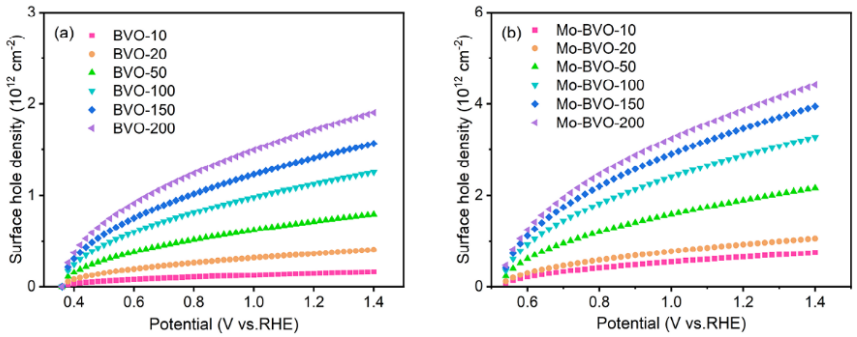

Figure 6.7 Surface hole density vs. applied potential of BVO (a) and Mo-BVO (b).

Linear sweep voltammetry of BVO and Mo-BVO samples was performed for studying the relation between current and surface hole density. The total current density generally consists of faradaic current and capacitive current. Faradaic current is caused by charge transfer in (photo)electrochemical reactions while capacitive current originates from charging or discharging of the electrochemical double layer. Herein, linear sweep voltammetry of BVO and Mo-BVO samples is obtained at sweep rates of 2 mV s^{-1} and 10 mV s^{-1} (**Figure 6.8**) in the dark and under illumination. Both BVO and Mo-BVO show negligible dark currents at potentials below 1.5 V vs. RHE as higher overpotentials for water oxidation are required. The photocurrents of BVO and Mo-BVO can reach up to 0.009 mA cm^{-2} and 0.095 mA cm^{-2}, respectively, at 1.23 V vs. RHE under illumination (435 nm, 200 mW cm^{-2}) at a sweep rate of 2 mV s^{-1}. However, the photocurrents of BVO and Mo-BVO increase to 0.013 mA cm^{-2} and 0.21 mA cm^{-2}, respectively, at a high sweep rate of 10 mV s^{-1} (**Figure 6.8**). These enhanced photocurrents likely originate from capacitive currents at the interface. So, consequently, the photocurrent densities measured at a low sweep rate of 2 mV s^{-1} were employed to calculate the real interfacial charge transfer rate r_h, derived by the following equation:

$$r_h = e\, N_A\, J_{faradaic} \quad \text{(eqn. 6.3)}$$

where N_A is Avogadro constant 6.02×10^{23} mol^{-1} and e is the elementary charge 1.6×10^{-19} Coulomb.

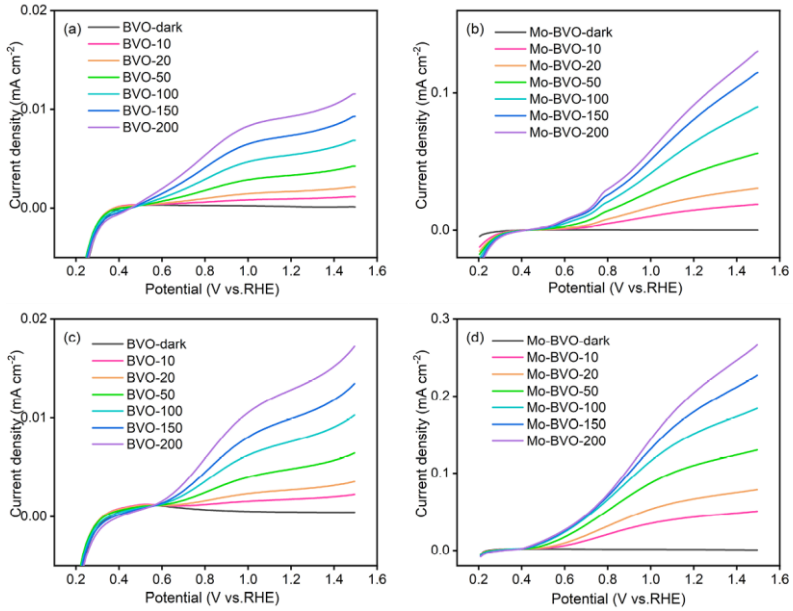

Figure 6.8 Current-voltage curves of BVO (a) and Mo-BVO (b) films, measured at a sweep rate of 2 mV s^{-1} in the dark and under illumination. Current-voltage curves of BVO (c) and Mo-BVO (d) films measured at a sweep rate of 10 mV s^{-1} in the dark and under illumination as reference. The light intensity varies from 10 to 200 mW cm^{-2} as indicated in the sample names (Mo-)BVO-XX.

6.3.3.2 Description of the surface hole model

The semiconductor-electrolyte interface is similar to a semiconductor metal junction as illustrated in **Figure 6.9**. Free electrons in the semiconductor will flow to the electrolyte after contacting due to the difference of their work function. Charge transfer reaches a balance until the Fermi energy of the semiconductor (E_f) equals to that of the solution (E_{sol}). Band bending and space change region in the semiconductor are subsequently formed for compensating the loss of electrons during the process.

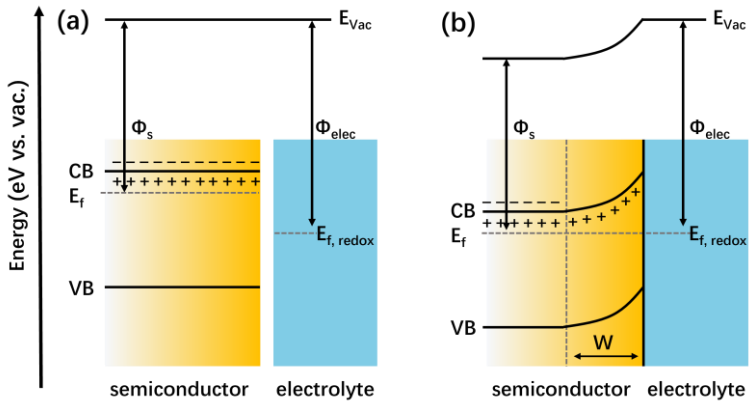

Figure 6.9 Illustration of n-type semiconductor electrolyte interface before (a) and after contact (b). The shallow ionized donor species and free electrons are denoted as "+" and "-" markers, respectively. Φ_s and Φ_{sol} are the work function of the semiconductor and the redox electrolyte. W is the width of space charge region.

The total positive charge number N_{total} in the depletion region of a semiconductor can be expressed as follows:

$$N_{total} = (N_{D^+} + p)\, A_c\, W \quad \text{(eqn. 6.4)}$$

where N_{D^+} , p and A_c represent the ionized donor density, free hole density and actual contacted area with electrolyte, respectively.

Assuming donors are completely ionized,

$$N_{D^+} = N_D = n_b \quad \text{(eqn. 6.5)}$$

where N_D and n_b represent donor density and bulk electron density of semiconductor, respectively, which are far larger than hole density *p* in depletion layer of an n-type semiconductor ($N_{D^+} \gg p$). Therefore, equation 6.4 can be simplified to:

$$N_{total} = N_D\, A_c\, W \quad \text{(eqn. 6.6)}$$

N_D is donor density, which is commonly used in the Mott Schottky equation:

$$\frac{1}{C^2} = \frac{2}{eN_D\varepsilon_0\varepsilon_s A_c{}^2}\left(U - U_{fb} - \frac{kT}{e}\right) \quad \text{(eqn. 6.7)}$$

C is the space charge layer capacitance of the semiconductor, *e* is elementary charge 1.602 × 10^{-19} C, ε_0 is the dielectric constant in vacuum (8.85 × 10^{-14} F cm^{-1}), ε_r is relative dielectric

constant of the semiconductor. A_c is the actual illuminated surface area, U_{fb} is the flat band potential, *k* Boltzmann constant, *T* temperature in Kelvin.

In the case of illumination, an equal number of holes and electrons are generated within the space charge region of the semiconductor. However, photogenerated electrons will flow into the bulk due to band bending and photogenerated holes accumulate in the space charge region. This leads to quasi-Fermi level splitting for holes (E_h) and electrons (E_e). The process is illustrated in **Figure 6.10**. Therefore, the total positive charge number will change to N'_{total}, which may be written as follows:

$$N'_{total} = (N_D + \Delta p)A_c\, W' = N'_D\, A_c\, W' \text{ (eqn. 6.8)}$$

Δp represents the photogenerated hole density (unit: cm^{-3}), N'_D represents the donor density under illumination, which can be calculated from the slope of the Mott-Schottky plot under illumination. *W'* is the width of space charge region under illumination.

The total number of photogenerated holes (ΔN_{total}) can be written as,

$$\Delta N_{total} = N'_{total} - N_{total} = \Delta p\, A_c\, W = N'_D\, A_c\, W' - N_D\, A_c\, W \text{ (eqn. 6.9)}$$

Where, N'_D and *W'* can be represented as,

$$N'_D = \frac{2}{slope'\, e\, \varepsilon_0 \varepsilon_s {A_c}^2} \; and \; N_D = \frac{2}{slope\, e\, \varepsilon_0 \varepsilon_s {A_c}^2} \text{ (eqn. 6.10)}$$

$$W' = \sqrt{\frac{2\varepsilon_0 \varepsilon_s (U - U'_{fb})}{e\, N'_D}} \; and \; W = \sqrt{\frac{2\varepsilon_0 \varepsilon_s (U - U_{fb})}{e\, N_D}} \text{ (eqn. 6.11)}$$

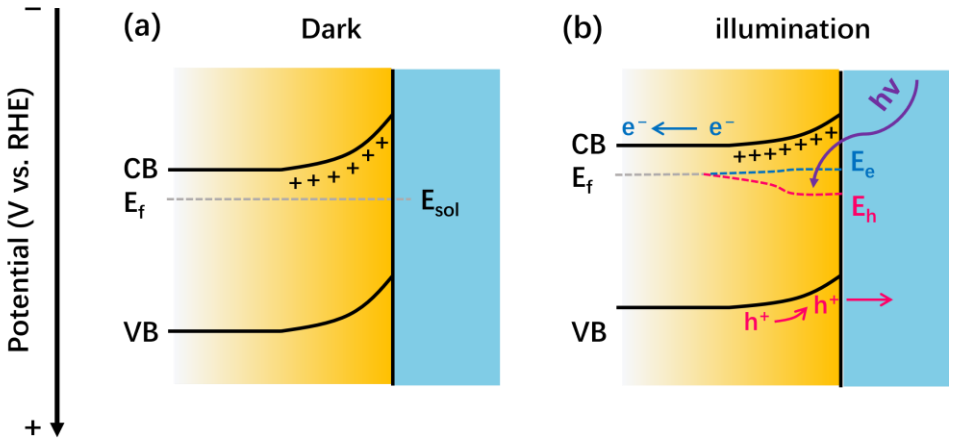

Figure 6.10 Schematic illustration of band diagram variation of semiconductor in the dark (a) and under illumination (b). The band bending of semiconductor depends applied potential and light illumination intensity. Besides, quasi-Fermi levels of electrons (E_e) and holes (E_h) in semiconductor will be produced after illumination. "+" markers represent the shallow ionized donor species.

Distribution of photogenerated holes within space charge region

The photoexcited holes will transfer and accumulate at the surface. This process is illustrated in **Figure 6.11**. The accumulated charge carriers in the space charge region follow the Fermi Dirac distribution, which is given as follows:

$$f_h(E) = \frac{1}{e^{-\frac{(\varepsilon_i-\mu)}{kT}}+1} = \frac{1}{e^{(-\frac{E}{kT})}+1} \quad \text{(eqn. 6.12)}$$

k is the Boltzmann constant, T is absolute temperature (K), μ is the total chemical potential of photogenerated holes, herein, μ indicates the energy of valence band maximum (VBM) at the surface. ε_i is the energy state of a single hole. E is the energy difference between ε_i and μ.

Since total probability of hole occupation (P_{total}) is 1, the integrated probability of finding a hole in the range from -3 *kT* to 0 equals to 1.

$$P_{total} = N_c \int_{-3kT}^{0} f_h(E)dE = 1 \text{ (eqn. 6.13)}$$

Nc is normalizing constant.

The surface hole density is p_s (unit: cm^{-2}). The hole density p_E at the energy state of E can be calculated by equation S7.

$$\frac{p_E}{p_s} = \frac{f_h(E)}{f_h(0)} = \frac{f_h(E)}{\frac{1}{e^0+1}} = 2f_h(E) \text{ (eqn. 6.14)}$$

$$p_E = 2p_s f_h(E) \text{ (eqn. 6.15)}$$

Therefore, the total number of photogenerated holes (ΔN_{total}) is integration of hole density over the energy from -3 *kT* to 0.

$$\Delta N_{total} = A_i \int_{-3kT}^{0} p_E \, N_c dE = 2p_s \, N_c A_c \int_{-3kT}^{0} f_h(E) dE = 2p_s A_c P_{total} = 2p_s A_c \text{ (eqn. 6.16)}$$

By combining eqn. 6.16 with eqn. 6.9, 6.10 and 6.11. we can finally derive the expression for the surface hole density p_s

$$p_s = 0.5 \, (N_D' \, W' - N_D \, W) = \frac{1}{e \, A_c} \left(\sqrt{\frac{U - U_{fb}'}{slope'}} - \sqrt{\frac{U - U_{fb}}{slope}} \right) \text{ (eqn. 6.17)}$$

Slope' and slope is the slope of Mott Schottky plot under illumination and in the dark, respectively. U_{fb}' and U_{fb} is the flat band position under illumination and in the dark.

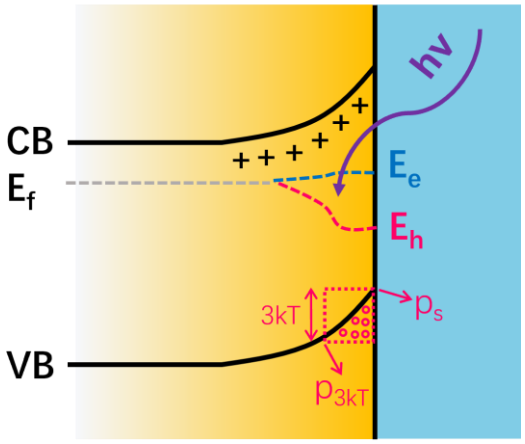

Figure 6.11 Proposed model for calculation of accumulated photogenerated hole concentration at semiconductor electrolyte interface under illumination at a specific potential. p_s is the surface hole density and p_{3kT} is bulk hole density at the position where the energy of holes is 3 *kT* lower than that of p_s.

The band bending of the space charge region is commonly larger than 3 *kT*, even at open circuit potential (OCP). This means almost all photogenerated holes accumulate within SCR, not extend into the bulk. For example, the flat band positions of BVO and Mo-BVO are 0.36 and 0.53 V vs. RHE, respectively. (**Table 6.1**) The OCP values of BVO and Mo-BVO are around 0.65 V vs. RHE. (Not presented) In this work, the applied potential of 0.7 to 1.4 V vs. RHE are employed to investigate relationship between charge transfer rate and surface accumulated hole density.

6.3.3.3 Water oxidation reaction rate law analysis of BVO and Mo-BVO

According to the model proposed by Durrant et al.,[9] the surface accumulated hole density can also be expressed as follows:

$$\frac{dp_s}{dt} = J_{hole} - k \times {p_s}^{\beta} \text{ (eqn. 6.18)}$$

where J_{hole} is the hole flux to the surface, *k* and β are rate constant and reaction order of the photoelectrochemical reaction, respectively. In steady state, the variation of $\frac{dp_s}{dt}$ is equal to zero, which simplifies 6.18 as follows:

$$J_{hole} = J_{faradaic} = k \times {p_s}^{\beta} \text{ (eqn. 6.19)}$$

By combining eqns. 6.3 and 6.19, the charge transfer rate r_h can be derived to

$$\log(r_h) = \beta \log(p_s) + \log(e\ N_A\ k) \text{ (eqn. 6.20)}$$

The relationship between charge transfer rate r_h and surface charge density p_s in BVO and Mo-BVO is plotted in **Figure 6.12**. The charge transfer rate is linearly proportional to surface charge density on a log-log scale. It is reported that the reaction order of water oxidation on $BiVO_4$ depends on surface hole density.[9] In our study, water oxidation follows first-order reaction at the potential of 0.7 V to 1.4 V vs. RHE under low surface hole density ($p_s < 0.1\ hole\ nm^{-2}$), which is in good agreement with literature.[9] This slightly counterintuitive conclusion implies that the rate-determining step of water oxidation on BVO and Mo-BVO only involves one surface hole.[9] Hydroxyl radicals are considered as the main intermediate during this single hole transfer step.[27]

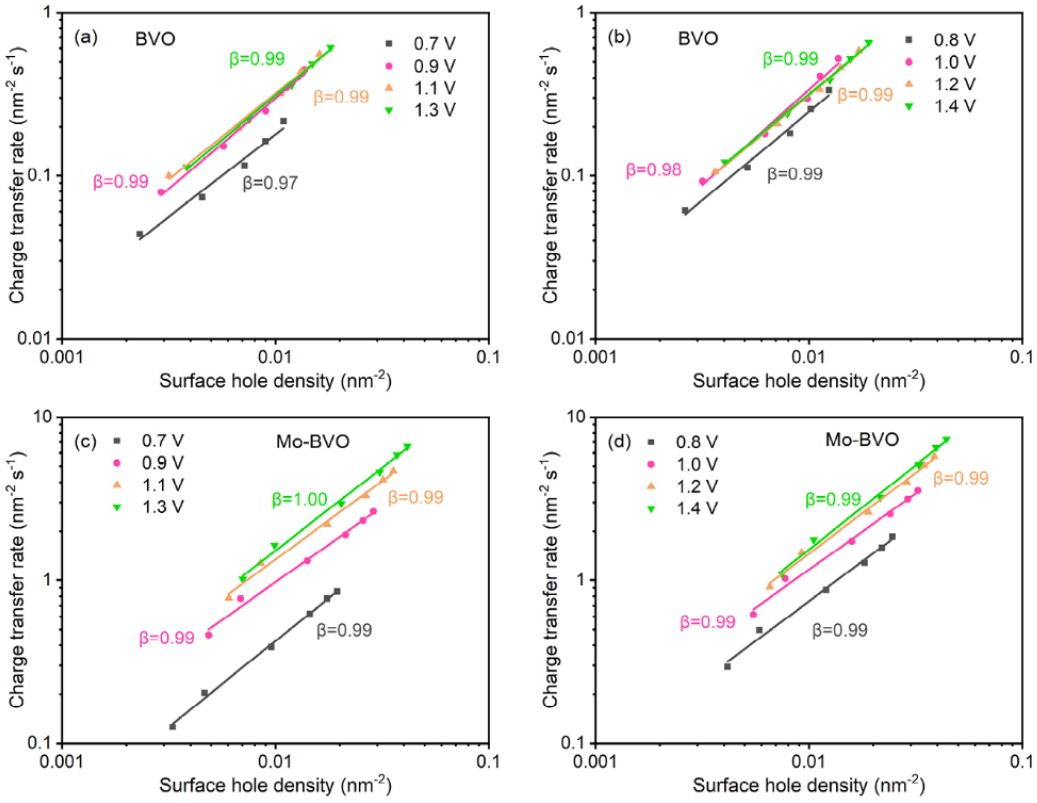

Figure 6.12 Relationship between charge transfer rate and surface accumulated hole density under illumination at different potentials.

Reaction rate constants of water oxidation on BVO and Mo-BVO and the corresponding rate constants vs. potential variation were determined and plotted in **Figure 13a-d**. For BVO (**Figure 13c**), there are two linear regimes, separated by the potential of 1.0 V vs. RHE. The reaction rate constant increases linearly when the potential is below 1.0 V. However, it plateaus off when the potential exceeds 1.0 V vs. RHE. This is possibly caused by oxidation of low valence state vanadium species. The highest apparent rate constant of water oxidation in BVO reaches up to 40 s^{-1}. For Mo-BVO samples, the apparent rate constant increases slowly when increasing the potential from 0.6 to 0.8 V vs. RHE, while it increases pronouncedly when increasing the potential from 0.8 to 1.4 V vs. RHE. In Mo-BVO, this phenomenon can also be explained by oxidation of the low valence state Mo species. To clarify this point further, we need to correlate the emergence of active sites with the redox potentials of the involved species.

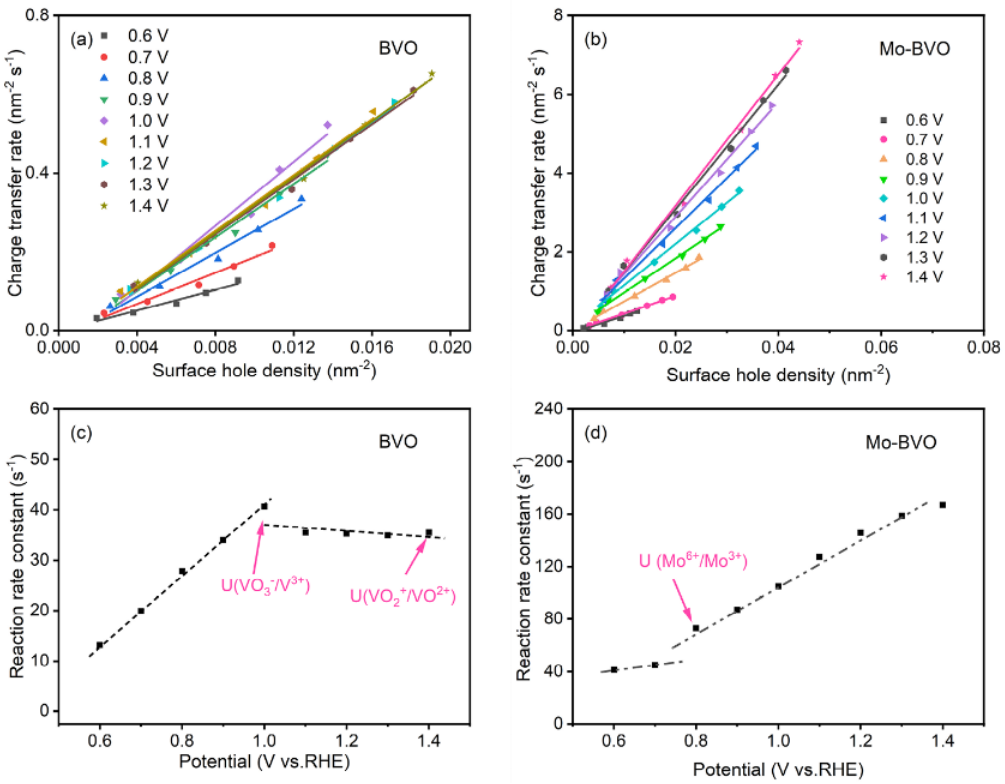

Figure 6.13 Reaction rate constants (a) and (b) at different applied potentials and relationship between reaction rate constant vs. applied potential plots of BVO (c) and Mo-BVO (d) samples during photoelectrochemical water oxidation.

6.3.3.4 Photo(electro)chemically active sites of BVO and Mo-BVO

Charge transfer occurs via surface active sites at the solid-liquid interface. The highest valence states of metal cations in metal oxides are likely active sites. For example, Chai et al. demonstrated that the Fe component in FeCoCrNi alloy can promote the formation of Ni^{4+} species which enhance the intrinsic catalytic activity of OER.[28] Zhang et al. reported that partial substitution of Sr at La sites in $LaFeO_3$ is favorable to form Fe^{4+} species which led to an increase in OER activity.[29]

In the case of BVO and Mo-BVO samples, the active sites that are induced by trapping of photogenerated and/or electrochemical holes should be Mo^{6+}, V^{5+} and Bi^{5+}. However, the redox potentials of $HV_2O_5^-/V^{3+}$ and VO_2^+/VO^{2+} are only 0.94 V and 1.39 V vs. RHE, respectively, while for Mo^{6+}/Mo^{3+} and Mo^{6+}/Mo^{4+} couples they are 0.83 V and 0.90 V vs. RHE, respectively, which also implies that these species are thermodynamically unable to oxidize water

molecules.[30, 31] The redox potential of VO_2^+/VO^{2+} thermodynamically meets the requirement of water oxidation, but the lowest overpotential of the four elementary steps in water oxidation is 0.37 V according to the OER adsorbate evolution mechanism (AEM).[32, 33] Consequently, there should be another redox active surface species, where Bi^{5+} is the most likely active site in both BVO and Mo-BVO, because the potential of Bi^{5+}/Bi^{3+} redox couples is 1.99 V vs. RHE. This hypothesis is supported by linear sweep voltammetry characterization (**Figure 6.14**). In dark condition, both BVO and Mo-BVO exhibit negligible current densities below the onset potential of 1.94 V vs. RHE due to insufficient oxidation ability. Nevertheless, numerous Bi^{5+} active sites are electrically induced in BVO and Mo-BVO which sharply enhance the current density, when the applied bias exceeds the onset potential of OER. This Bi^{5+} active sites are expected to be verified by the state-of the art in-situ or operando PEC instruments in the future.

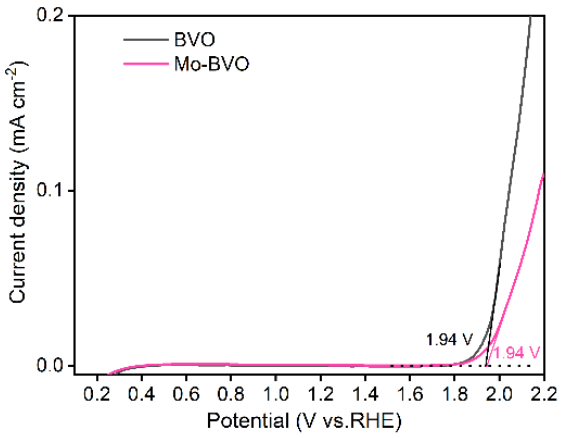

Figure 6.14 Linear sweep voltammetry curves of BVO and Mo-BVO films samples, measured at a sweep rate of 10 mV s^{-1} in the dark. The applied potential varies from 0.2 V to 2.2 V vs. RHE.

To further investigate the water oxidation mechanism on BVO and Mo-BVO samples from the aspect of the interfacial band energetics, the work functions and valence band positions were measured by UPS. The secondary electron cutoff energies of BVO and Mo-BVO samples were determined to be 16.5 eV and 16.7 eV, resulting in work functions of 4.7 eV and 4.5 eV, respectively, while their valence band maxima were measured to be 2.36 and 2.39 eV below the Fermi level, respectively (**Figure 6.15**).

Combined with the optical bandgap values of BVO samples (2.45 eV and 2.56 eV with and without Mo, respectively – see **Figure 6.3**) and the redox potentials of metal ions, we propose a schematic diagram to explain the reaction mechanism of water oxidation at the surface of BVO and Mo-BVO samples involving Bi^{5+} sites in **Figure 6.16**. The oxidation state of Mo^{6+} ions is larger than that of V^{5+} ions while the electronegativity of Mo atoms (2.16) is greater than that of V atoms (1.63). Therefore, Mo^{6+} ions polarize the Mo-O bond in MoO_4^{2-} tetrahedrons more strongly than V^{5+} does in VO_4^{3-} tetrahedrons. This implies Mo doping in BVO can effectively suppress the formation of oxygen vacancies and the emergence of low valence V species during sample preparation at high temperature. According to our previous work, the surface recombination rate of charge carriers in Mo-BVO is about five times lower than that in BVO.[11] Based on the above analysis, we reckon that low valence V species existing at the surface of BVO are the main factors that lead to a high surface recombination rate and slow water oxidation kinetics. The photocurrent and apparent rate constant of Mo-BVO are 10 times and 4 times higher than that of BVO. This is mainly attributed to the reduced number of low valence state V species at the surface of Mo-BVO induced by Mo doping.[11]

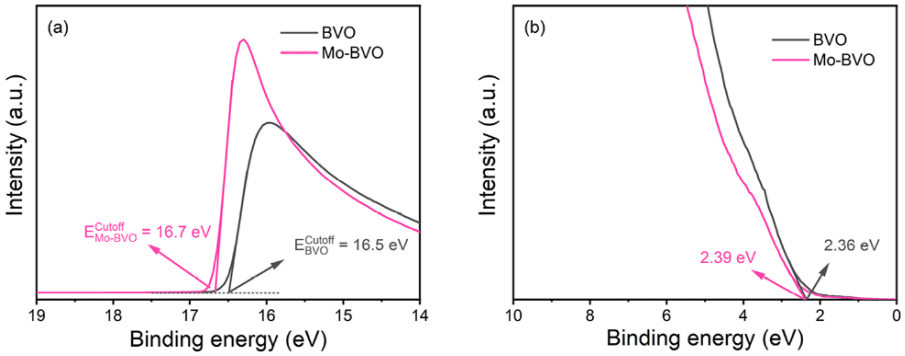

Figure 6.15 Secondary electron cutoff energies and valence band maximum positions determination of BVO and Mo-BVO samples, measured by UPS. For the secondary electron cutoff determination, a bias of – 6 V was applied to the sample and the spectra were subsequently corrected.

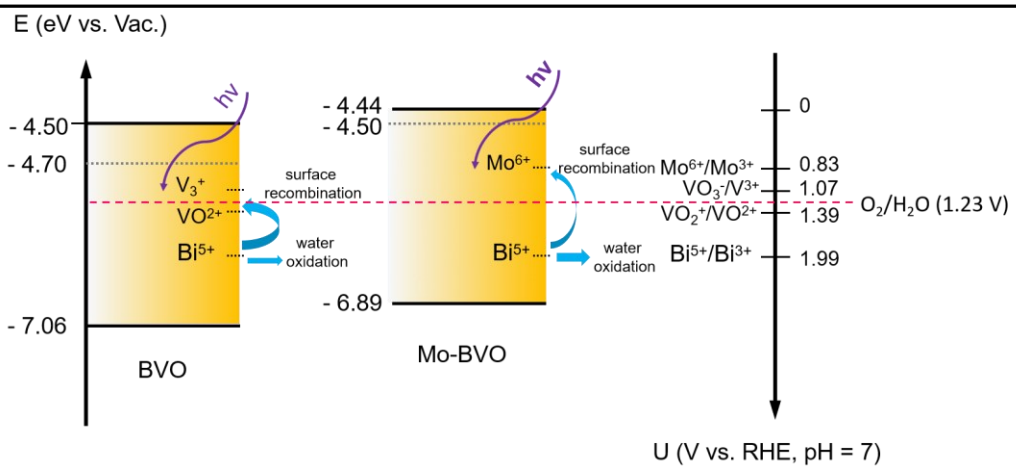

Figure 6.16 Proposed schematic diagram of water oxidation at the interfaces of BVO and Mo-BVO samples.

6.4 Conclusions

In summary, $BiVO_4$ (BVO) and Mo-doped $BiVO_4$ (Mo-BVO) thin film photoelectrodes were employed as model systems to investigate the impact of surface hole accumulation on the photocurrent density. A semiconductor electrolyte junction model was developed for determining the surface accumulated hole density and investigating the kinetics of water oxidation on BVO and Mo-BVO photoelectrodes. Based on this model, we demonstrated that (1) surface hole density at the interface of the BVO and Mo-BVO model systems depends on the light irradiation intensity and applied potential. (2) Water oxidation on both BVO and Mo-BVO samples follows a first order reaction mechanism under low surface accumulated density. (3) According to the redox potential of the involved metal ions, we assume that the active sites in both BVO and Mo-BVO are very likely to be Bi^{5+} which can be generated by photoexcitation and/or electric potential, rather than VO_x species and Mo^{6+}. (4) The observed promotional effect of Mo doping in water oxidation mainly originates from a reduced interfacial recombination rate. This work offers a relatively complete physical image for generation and transfer of the photo(electro)-induced holes, as well as their accumulation and distribution within the space charge region (SCR) of a semiconductor photoanode and surface hole-related water oxidation kinetics with possibility to transfer to other materials systems.

References

[1] J.H. Kim, D. Hansora, P. Sharma, J.W. Jang, J.S. Lee, Toward practical solar hydrogen production - an artificial photosynthetic leaf-to-farm challenge, *Chem. Soc. Rev.*, **2019**, *48*, 1908-1971.

[2] M.G. Walter, E.L. Warren, J.R. McKone, S.W. Boettcher, Q. Mi, E.A. Santori, a.N.S. Lewis, Solar Water Splitting Cells, *Chem. Rev.*, **2010**, *110*, 6446-6473.

[3] F. Li, H. Yang, Q. Zhuo, D. Zhou, X. Wu, P. Zhang, Z. Yao, L. Sun, ACobalt@Cucurbit[5]uril Complexasa Highly Efficient Supra-molecular Catalyst for Electrochemical and Photoelectrochemical Water Splitting, *Angew. Chem. Int. Ed.*, **2021**, *60*, 1976-1985.

[4] S. Corby, L. Francas, S. Selim, M. Sachs, C. Blackman, A. Kafizas, J.R. Durrant, Water Oxidation and Electron Extraction Kinetics in Nanostructured Tungsten Trioxide Photoanodes, *J. Am. Chem. Soc.*, **2018**, *140*, 16168-16177.

[5] C.A. Mesa, A. Kafizas, L. Francas, S.R. Pendlebury, E. Pastor, Y. Ma, F. Le Formal, M.T. Mayer, M. Gratzel, J.R. Durrant, Kinetics of Photoelectrochemical Oxidation of Methanol on Hematite Photoanodes, *J. Am. Chem. Soc.*, **2017**, *139*, 11537-11543.

[6] A. Kafizas, X. Wang, S.R. Pendlebury, P. Barnes, M. Ling, C. Sotelo-Vazquez, R. Quesada-Cabrera, C. Li, I.P. Parkin, J.R. Durrant, Where Do Photogenerated Holes Go in Anatase:Rutile TiO_2? A Transient Absorption Spectroscopy Study of Charge Transfer and Lifetime, *J. Phys. Chem. A*, **2016**, *120*, 715-723.

[7] Y. Ma, S.R. Pendlebury, A. Reynal, F. Le Formal, J.R. Durrant, Dynamics of photogenerated holes in undoped $BiVO_4$ photoanodes for solar water oxidation, *Chem. Sci.*, **2014**, *5*, 2964-2973.

[8] F. Le Formal, E. Pastor, S.D. Tilley, C.A. Mesa, S.R. Pendlebury, M. Gratzel, J.R. Durrant, Rate law analysis of water oxidation on a hematite surface, *J. Am. Chem. Soc.*, **2015**, *137*, 6629-6637.

[9] Y. Ma, C.A. Mesa, E. Pastor, A. Kafizas, L. Francàs, F. Le Formal, S.R. Pendlebury, J.R. Durrant, Rate Law Analysis of Water Oxidation and Hole Scavenging on a $BiVO_4$ Photoanode, *ACS Energy Lett.*, **2016**, *1*, 618-623.

[10] R. Chen, D. Zhang, Z. Wang, D. Li, L. Zhang, X. Wang, F. Fan, C. Li, Linking the Photoinduced Surface Potential Difference to Interfacial Charge Transfer in Photoelectrocatalytic Water Oxidation, *J. Am. Chem. Soc.*, **2023**, *145*, 4667-4674.

[11] X. Wu, F.E. Oropeza, Z. Qi, M. Einert, C. Tian, C. Maheu, K. Lv, J.P. Hofmann, Influence of Mo doping on interfacial charge carrier dynamics in photoelectrochemical water oxidation on $BiVO_4$, *Sustain. Energy Fuels*, **2023**, *7*, 2923-2933.

[12] N. Khan, F. Stelo, G.H.C. Santos, L.M. Rossi, R.V. Gonçalves, H. Wender, Recent advances on Z-scheme engineered $BiVO_4$-based semiconductor photocatalysts for CO_2 reduction: A review, *Appl. Surf. Sci. Adv.*, **2022**, *11*, 100289.

[13] Y. Wei, J. Su, X. Wan, L. Guo, L. Vayssieres, Spontaneous photoelectric field-enhancement effect prompts the low cost hierarchical growth of highly ordered heteronanostructures for solar water splitting, *Nano Res.*, **2016**, *9*, 1561-1569.

[14] T. Jiang, F. Nan, J. Zhou, Enhanced photocatalytic and photoelectrochemical performance of g-C_3N_4/$BiVO_4$ heterojunction: A combined experimental and theoretical study, *AIP Adv.*, **2019**, *9*, 055225.

[15] S.S. Mali, G.R. Park, H. Kim, H.H. Kim, J.V. Patil, C.K. Hong, Synthesis of nanoporous Mo:$BiVO_4$ thin film photoanodes using the ultrasonic spray technique for visible-light water splitting, *Nanoscale Adv.*, **2019**, *1*, 799-806.

[16] Z. Jiang, Y. Liu, T. Jing, B. Huang, X. Zhang, X. Qin, Y. Dai, M.-H. Whangbo, Enhancing the Photocatalytic Activity of $BiVO_4$ for Oxygen Evolution by Ce Doping: Ce^{3+} Ions as Hole Traps, *J. Phys. Chem. C*, **2016**, *120*, 2058-2063.

[17] Y. Zhou, L. Zhang, L. Lin, B.R. Wygant, Y. Liu, Y. Zhu, Y. Zheng, C.B. Mullins, Y. Zhao, X. Zhang, G. Yu, Highly Efficient Photoelectrochemical Water Splitting from Hierarchical WO_3/$BiVO_4$ Nanoporous Sphere Arrays, *Nano Lett.*, **2017**, *17*, 8012-8017.

[18] M. Huang, J. Bian, W. Xiong, C. Huang, R. Zhang, Low-dimensional Mo:$BiVO_4$ photoanodes for enhanced photoelectrochemical activity, *J. Mater. Chem. A*, **2018**, *6*, 3602-3609.

[19] W. Luo, Z. Li, T. Yu, Z. Zou, Effects of Surface Electrochemical Pretreatment on the Photoelectrochemical Performance of Mo-Doped $BiVO_4$, *J. Phys. Chem. C*, **2012**, *116*, 5076-5081.

[20] M. Einert, A. Waheed, S. Lauterbach, M. Mellin, M. Rohnke, L.Q. Wagner, J. Gallenberger, C. Tian, B.M. Smarsly, W. Jaegermann, F. Hess, H. Schlaad, J.P. Hofmann, Sol‐Gel‐Derived Ordered Mesoporous High Entropy Spinel Ferrites and Assessment of Their Photoelectrochemical and Electrocatalytic Water Splitting Performance, *Small*, **2023**, *19*, 2205412.

[21] V.-I. Merupo, S. Velumani, K. Ordon, N. Errien, J. Szade, A.-H. Kassiba, Structural and optical characterization of ball-milled copper-doped bismuth vanadium oxide ($BiVO_4$), *CrystEngComm*, **2015**, *17*, 3366-3375.

[22] M.R.d.S. Pelissari, N.F. Azevedo Neto, L.P. Camargo, L.H. Dall'Antonia, Characterization and Photo-Induced Electrocatalytic Evaluation for $BiVO_4$ Films Obtained by the SILAR Process, *Electrocatalysis*, **2021**, *12*, 211-224.

[23] W. Luo, J. Wang, X. Zhao, Z. Zhao, Z. Li, Z. Zou, Formation energy and photoelectrochemical properties of $BiVO_4$ after doping at Bi^{3+} or V^{5+} sites with higher valence metal ions, *Phys. Chem. Chem. Phys.*, **2013**, *15*, 1006-1013.

[24] X. Zhao, W. Luo, J. Feng, M. Li, Z. Li, T. Yu, Z. Zou, Quantitative Analysis and Visualized Evidence for High Charge Separation Efficiency in a Solid-Liquid Bulk Heterojunction, *Adv. Energy Mater.*, **2014**, *4*, 1301785.

[25] A.M. Fajardo, N.S. Lewis, Free-Energy Dependence of Electron-Transfer Rate Constants at Si/Liquid Interfaces, *J. Phys. Chem. B*, **1997**, *101*, 11136-11151.

[26] J. Li, M.M. Waegele, Advances in understanding the role of surface hole formation in heterogeneous water oxidation, *Curr. Opin. Electrochem.*, **2022**, *33*, 100932.

[27] A.J. Bard, Inner-Sphere Heterogeneous Electrode Reactions. Electrocatalysis and Photocatalysis: The Challenge, *J. Am. Chem. Soc.*, **2010**, *132*, 7559-7567.

[28] N. Zhang, X. Feng, D. Rao, X. Deng, L. Cai, B. Qiu, R. Long, Y. Xiong, Y. Lu, Y. Chai, Lattice oxygen activation enabled by high-valence metal sites for enhanced water oxidation, *Nat. Commun.*, **2020**, *11*, 4066.

[29] Z. Shen, Y. Zhuang, W. Li, X. Huang, F.E. Oropeza, E.J.M. Hensen, J.P. Hofmann, M. Cui, A. Tadich, D. Qi, J. Cheng, J. Li, K.H.L. Zhang, Increased activity in the oxygen evolution

reaction by Fe^{4+}-induced hole states in perovskite $La_{1-x}Sr_xFeO_3$, *J. Mater. Chem. A*, **2020**, *8*, 4407-4415.

[30] Y. Hermans, S. Murcia-López, A. Klein, R.v.d. Krol, T. Andreu, J.R. Morante, T. Toupance, W. Jaegermann, Analysis of the interfacial characteristics of $BiVO_4$/metal oxide heterostructures and its implication on their junction properties, *Phys. Chem. Chem. Phys.*, **2019**, *21*, 5086--5096.

[31] A.J. Bard, R. Parsons, J. Jordan, Standard Potentials in Aqueous Solution, CRC Press, 1985.

[32] J. Song, C. Wei, Z.F. Huang, C. Liu, L. Zeng, X. Wang, Z.J. Xu, A review on fundamentals for designing oxygen evolution electrocatalysts, *Chem. Soc. Rev.*, **2020**, *49*, 2196-2214.

[33] Z. Shi, X. Wang, J. Ge, C. Liu, W. Xing, Fundamental understanding of the acidic oxygen evolution reaction: mechanism study and state-of-the-art catalysts, *Nanoscale*, **2020**, *12*, 13249-13275.

7. Conclusions and perspectives

The intention of this dissertation is to investigate the structure-activity relationships of the bismuth-based photocatalytic/photoabsorber materials BiOCl and $BiVO_4$ for photoelectrochemical applications. This chapter will summarize main conclusions and novelties of these studies. Subsequently, comments and perspectives on these works are presented in the end for guiding further research.

7.1 Conclusions

Part I: Effect of thermally Induced OVs in BiOCl Nanosheets on their photoelectrochemical performance

(1) BiOCl is extremely surface-sensitive to temperature and OVs can be thermally induced at 200 °C in He atmosphere.

(2) Specific adsorption of CO_2 on the surface of BiOCl nanosheets bearing OVs is confirmed by in-situ DRIFTS. The formation process of OVs could be traced by using CO_2 as IR probe molecule.

(3) Introduction of OVs not only increases concentration of charge carriers but also gives rise to two kinds of shallow and deep defect states. Shallow defect states as electrons sinks accelerate separation of charge carriers and remarkably enhance the photocurrent, while deep defect states as recombination centers negatively impact on photocurrent.

(4) Photoelectrochemical performance of BiOCl nanosheets is dominantly determined by the balance of OV induced generation (doping) and defect mediated recombination of charge carriers.

Part II: Influence of Mo doping in $BiVO_4$ on interfacial charge carrier dynamics of photoelectrochemical water oxidation

The photoelectrochemical activities of semiconductors are closely dependent on their resistance at the semiconductor electrolyte interface. In this work, Mo doping of BVO films was introduced by a spin coating approach. Mo doping are confirmed by XPS and Raman

spectra. The influence of Mo doping on BVO is investigated from the aspect of interfacial resistance and charge carrier transfer. Our results show:

(1) Interfacial charge transfer resistances (R_{ct}) of $BiVO_4$ in 0.1 M phosphate buffer solution decrease 2 to 3 orders of magnitude under illumination.

(2) Both dark and photo current densities of BVO in OER are dominantly limited by R_{ct}, rather than R_{bulk}.

(3) Mo doping of BVO can not only effectively decrease charge transfer resistance (R_{ct}) under illumination, but also increase photovoltage.

(4) In comparison with bare BVO, Mo doped BVO exhibits an enhanced photocurrent density at 1.23 V vs. RHE by a factor of 2.7.

Part III: Promoting effect of interfacial hole accumulation on photoelectrochemical water oxidation in $BiVO_4$ and Mo doped $BiVO_4$

BVO and Mo-BVO film samples were employed as model systems to investigate the impact of surface hole accumulation on photocurrent density. A semiconductor solution junction model was developed for determining the surface accumulated hole density and investigating rate laws of water oxidation on BVO and Mo-BVO photoelectrodes. Based on this model, we demonstrated that:

(1) Surface hole density at the interface of the BVO and Mo-BVO model systems is associated with light irradiation intensity and applied potential.

(2) Water oxidation on both BVO and Mo-BVO samples follow a first order reaction mechanism under low surface accumulated density, which is in good agreement with the literature.

(3) According to the redox potential of the involved metal ions, we speculate that the active sites in both BVO and Mo-BVO are Bi^{5+} which can be generated by photoexcitation and/or electric potential, rather than VO_x species and Mo^{6+}.

(4) The observed promotional effect of Mo doping in water oxidation mainly originates from a reduced interfacial recombination rate.

The novelties in the dissertation are emphasized as follows:

In the first work, we found that BiOCl readily forms oxygen vacancies upon thermal treatment in He atmosphere. These thermally induce oxygen vacancies in BiOCl lead to shallow and deep defect states. Shallow defect states as electrons sinks accelerate separation of charge carriers and positively enhance the photocurrent, while deep defect states as recombination centers negatively impact on photocurrent.

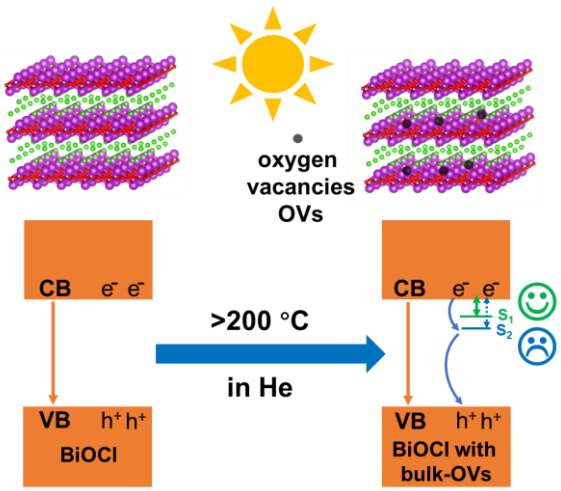

Figure 7.1 Illustration of the effect of OVs in BiOCl nanosheets on defect states.

In the second work, we investigated the effect of Mo doping in $BiVO_4$ on interfacial resistance and charge carrier transfer of photoelectrochemical water oxidation. Our results show that the photocurrent during water oxidation in $BiVO_4$ is predominantly limited by charge transfer resistance (R_{ct}), rather than the semiconductor bulk resistance (R_{bulk}). Mo doping of $BiVO_4$ can slightly reduce R_{bulk} but obviously decrease R_{ct}.

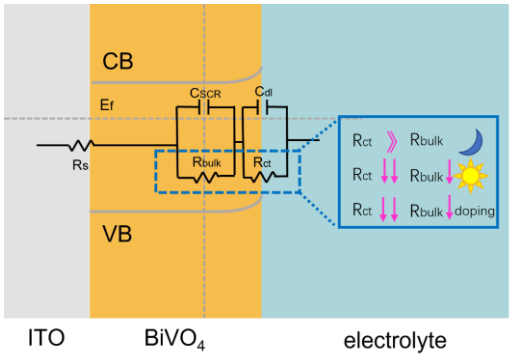

Figure 7.2 Influence of Mo doping in $BiVO_4$ photoanode on bulk resistance (R_{bulk}) and interfacial charge transfer resistance (R_{ct}).

In the third work, we proposed a general surface hole model of the semiconductor electrolyte junction to determine the surface hole density of BVO and Mo-BVO samples via employing illumination intensity-dependent Mott-Schottky measurements. The relationship between surface hole density and photocurrent is linked based on this model. Besides, water oxidation active sites in both $BiVO_4$ and Mo doped $BiVO_4$ are considered as Bi^{5+}, rather than VO_x or Mo^{6+} species. In a word, this study gives a relatively complete physical image for generation and transfer of the photo(electro)-induced holes, as well as their accumulation and distribution within the space charge region (SCR) of semiconductor and surface hole-related water oxidation dynamics.

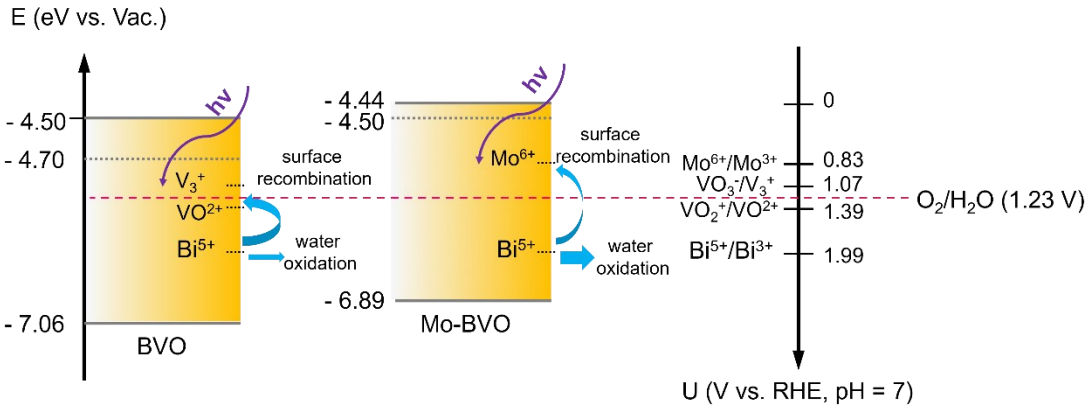

Figure 7.3 Effect of Mo doping in $BiVO_4$ photoanode on band diagram, interfacial charge carrier dynamics and water oxidation active sites.

7.2 Perspectives

The relationship between thermally induced OVs and two kinds of defect states (shallow and deep) in BiOCl is investigated in detail. The photocatalytic performances of BVO and Mo-BVO samples in water oxidation are well elaborated from the aspects of surface charge carrier dynamic, charge transfer resistance, as well as the surface hole density and active site in this dissertation. Nevertheless, some subsequent studies are worthy to be conducted in the future.

(1) The formation of shallow states near the CBM in BiOCl is beneficial to its photoelectrochemical performance due to the increased electron concentration (doping) and effective thermal excitation of electrons. However, deep states in BiOCl can act as recombination center for the electrons. Therefore, the precise control of the energy band

positions of defect states in semiconductors is expected to be a feasible approach for further improvement of the photoelectrochemical performance under heating conditions.

(2) Surface charge density is a good descriptor for investigating photoelectrochemical reactions. Moreover, it sheds light on the reaction dynamics via linking surface charge density and performance. The surface hole density model is universal for the semiconductor-electrolyte junction and is also applicable to electrons in p-type semiconductors, but the photogenerated holes/electrons in some photoanodic/photocathodic materials are limited and likely insufficient to bring about an obvious change of the slopes in Mott Schottky plots. Consequently, the development of some other techniques and strategies on surface charge density is also urgently required.

(3) Surface hole model in principle is not applicable to interface modification of the $BiVO_4$, such as the deposition of the noble metals. This is due to the presence of two kinds of solid-solution interfaces, i.e., semiconductor-electrolyte interface and metal-electrolyte interface. The photoexcited holes accumulate at both metal and semiconductor interfaces, leading to forming a complicate system. Accordingly, a modified surface hole model for complicate systems is expected to be established.

(4) Surface micro-structure of catalysts is often directly linked to photocatalytic performance. Therefore, the micro-morphology design and adjustment of $BiVO_4$ (BVO) is also an interesting and meaningful research topic.

(5) The long-term stability and corresponding deactivation mechanism of $BiVO_4$ (BVO) and Mo-BVO samples should be investigated via in-situ or operando techniques. The improved approaches are expected to be proposed after the investigation of change of the surface components and possible surface reconstruction.

Acknowledgements

First of all, I would like to express my most sincere gratitude to my supervisor prof. Jan Philipp Hofmann for giving me the wonderful opportunity to conduct my doctoral research project in the Surface Science Laboratory at TU Darmstadt. Thank you very much for your valuable guidance and assistance, as well as your persistent support and encouragement throughout my whole doctoral studies. Your scientific meticulousness and curiosity inspire me a lot. Besides, I have also benefited greatly from your optimism about life and work.

I am very grateful to Prof Emiel Hensen for accepting me as a Ph.D. student to study in the Inorganic Materials and Catalysis (IMC) group at TU Eindhoven. Your profound knowledge and scientific perspective are great of benefit to me. It is an unforgettable experience to study in your group. I will miss the wonderful time I spent there forever.

I would also like to thank my master supervisor prof. Kangle Lv for helping me with the XRD and SEM measurements and providing me with a nice workplace to complete my dissertation. All your support and help are very much appreciated.

I would also like to deeply thank all my colleagues and friends in both the Surface Science Laboratory (SSL) and the Inorganic Materials and Catalysis (IMC) group for their help in both scientific research and life during my Ph.D. project. I am fortunate to have all of you as friends in my life. Special thanks to Dr. Longfei Wu, Dr. Lu Gao, Dr. Freddy E. Oropeza, Dr. Yaqiong Su, Yue Zhang, Dr. Valerii Muravev, Nitin Puthuval Prasad, Dr. Yannick Hermans, Dr. Clément Maheu, Dr. Marcus Einert, Dr. Tim Hellmann, Chuanmu Tian, Dr. Jingwen Qian, Dr. Binxiang Huang, Dr. Wei Li, Christopher Gort, Dominik Moritz, Qingyang Wu, Dr. Yongchao Chen, Pengcheng Hu, and Julia Gallenberger for guiding and advising me in the process of my experiments and paper writing.

I would also like to acknowledge the Chinese Scholarship Council (CSC) for the financial support during my Ph.D. study (scholarship No. 201708420159).

Finally, I would like to express my deep gratitude to my parents, Mr. Qihong Wu and Mrs. Wenjuan Lv, my brother-in-law, Mr. Hui Dai, my sister, Mrs. Yaling Wu, and my nephew, Mr. Yuxiang Dai. Thank you for your unconditional love and support, which keeps me going.

Curriculum Vitae

Xiaofeng Wu

Education and Work Experience

- 2020.10-Present: Ph.D. Candidate Materials Science, Technical University of Darmstadt, Germany (**Supervisor: Prof. Jan Philipp Hofmann**)
- 2017.10-2020.10: Ph.D. Candidate Materials Science, Eindhoven University of Technology, the Netherlands (**Supervisor: Prof. Emiel Hensen and Prof. Jan Philipp Hofmann**)
- 2014.09-2017.06: Master candidate of Inorganic Chemistry, South-Central Minzu University, China (**Supervisor: Prof. Kangle Lv**)
- 2011.09-2014.08: Technician of Suzhou Taihu Electric Advanced Materials Co. Ltd., China
- 2007.09-2011.06: Bachelor of Applied Chemistry, Wuhan Institute of Technology, China

Conferences

- Physics @Veldhoven 2020: the Art of Physics, January 21-22, 2020, Veldhoven, the Netherlands, **Poster**.
- The XXI Netherlands' Catalysis and Chemistry Conference (NCCC), March 2-4, 2020, *Noordwijkerhout*, *the Netherlands*, **Poster**.
- Electrochemistry 2022-At the Interface between Chemistry and Physics, September 27-30, 2022, *Berlin*, *Germany*, **Poster**.

Honors and Awards

- The XXI Netherlands' Catalysis and Chemistry Conference (NCCC), Best Poster Award (2020)
- Ph.D. Scholarship of Chinese Scholarship Council (2017-2021)
- Chinese National Scholarship for Master Students (2016)
- First Class Professional Scholarship for Master Students (2015 and 2016)

Publications

(1) **Xiaofeng Wu,** Freddy E. Oropeza, Shixin Chang, Marcus Einert, Qingyang Wu, Clément Maheu, Julia Gallenberger, Chuanmu Tian, Kangle Lv, Jan P. Hofmann, Promoting effect of interfacial hole accumulation on photoelectrochemical water oxidation in $BiVO_4$ and Mo doped $BiVO_4$, *Advanced Powder Materials*, doi.org/10.1016/j.apmate.2024.100234.

(2) **Xiaofeng Wu,** Freddy E. Oropeza, Zheng Qi, Marcus Einert, Chuanmu Tian, Clement Maheu, Kangle Lv and Jan P. Hofmann, Influence of Mo doping on interfacial charge carrier dynamics in photoelectrochemical water oxidation on $BiVO_4$, *Sustainable Energy & Fuels*, **2023,** 7, 2923-2933.

(3) **Xiaofeng Wu**, Freddy E. Oropeza, Daan den Boer, Peter Kleinschmidt, Thomas Hannappel, Dennis G. H. Hetterscheid, Emiel J. M. Hensen, Jan P. Hofmann, Thermally induced oxygen vacancies in BiOCl nanosheets and their impact on photoelectrochemical performance, *ChemphotoChem*, **2022**, e202200192.

(4) **Xiaofeng Wu**, Jinshui Cheng, Xiaofang Li, Yuhan Li, Kangle Lv, Enhanced visible photocatalytic oxidation of NO by repeated calcination of g-C_3N_4, *Appl. Surf. Sci.* **2019**, *465*, 1037-1046.

(5) **Xiaofeng Wu**, Lili Wen, Kangle Lv, Kejian Deng, Dingguo Tang, Hengpeng Ye, Dongyun Du, Sining Liu, Mei Li, Fabrication of ZnO/graphene flake-like photocatalyst with enhanced photoreactivity. *Appl. Surf. Sci.* **2015**, *358*, 130-136.

(6) **Xiaofeng Wu**, Shun Fang, Yang Zheng, Jie Sun, Kangle Lv, Thiourea-modified TiO_2 nanorods with enhanced photocatalytic activity. *Molecules*, **2016**, *21*, 181.

(7) Xiaoying Xi, Feng Zeng, Heng Zhang, **Xiaofeng Wu**, Jie Ren, Timo Bisswanger, Christoph Stampfer, Jan P. Hofmann, Regina Palkovits, and Hero J. Heeres, CO_2 Hydrogenation to Higher Alcohols over K-Promoted Bimetallic Fe−In Catalysts on a Ce−ZrO_2 Support, *ACS Sustainable Chem. Eng.* **2021**, *9,* 6235−6249.

(8) Yumei Lin, Yan Wang, Hongxia Wang, Jingjing Wang, **Xiaofeng Wu**, Jan P. Hofmann, Giulio Gorni, Victor A. de la Peña O'Shea, Freddy E. Oropeza & Kelvin H. L. Zhang, Inductive effect of Ti-doping in Fe_2O_3 enhances the photoelectrochemical water oxidation, *Science China Chemistry* **2023**, *66*, 2091–2097.